Fractal-Based Point Processes

2005

Steven Bradley Lowen
Harvard Medical School
McLean Hospital

Malvin Carl Teich
Boston University
Columbia University

WILEY

Appendix B
Problem Solutions

B.1 INTRODUCTION

Prob. 1.1.1 Figure B.1 displays the measured coastline length d as a function of the measurement scale s used.

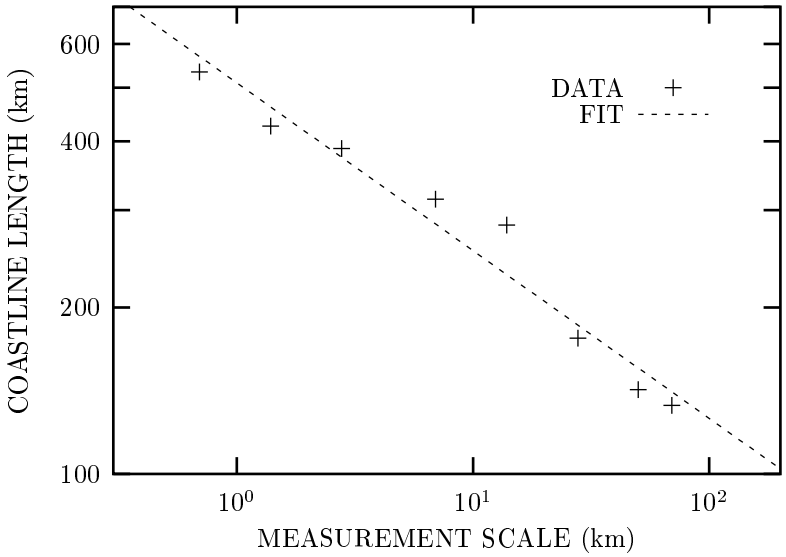

Fig. B.1 Coastline length d vs. measurement scale s (+ symbols). The data are well described by a straight line on this doubly logarithmic plot, revealing that $d \propto \mathsf{s}^c$. A least-squares fit based on the logarithms, shown as the dashed line, exhibits a slope $c \approx -0.30$.

Prob. 1.1.2 Taking the logarithm of both sides of Eq. (1.1) yields $\ln(d) = c\ln(\mathsf{s}) + \ln(b)$, for some constant b. This suggests fitting a straight line to a plot of $\ln(d)$ vs. $\ln(\mathsf{s})$ to obtain the slope, c. This also explains the use of logarithmic coordinates for both axes of Fig. B.1. Such a least-squares fit yields $c \approx -0.30$.

Prob. 1.1.3 Consulting an atlas reveals that the South African coastline is exceptionally smooth, the coastline of Britain is much rougher, and that of Australia lies somewhere between the two. Iceland's coastline appears the roughest of all. Evidently, the power-law exponent c provides an index of roughness, with larger negative magnitudes signifying more irregular coastlines.

Prob. 1.2.1 Place n points evenly spaced about the perimeter of a circle of unit circumference, and connect adjacent points to form a regular polygon of n sides, each of length s, as shown in Fig. B.2. Now draw line segments from each point on the perimeter to the center of the circle; all have a length equal to the radius $\mathsf{r} = 1/2\pi$. Considering one of the isosceles triangles thus generated, let θ_1 denote the value of

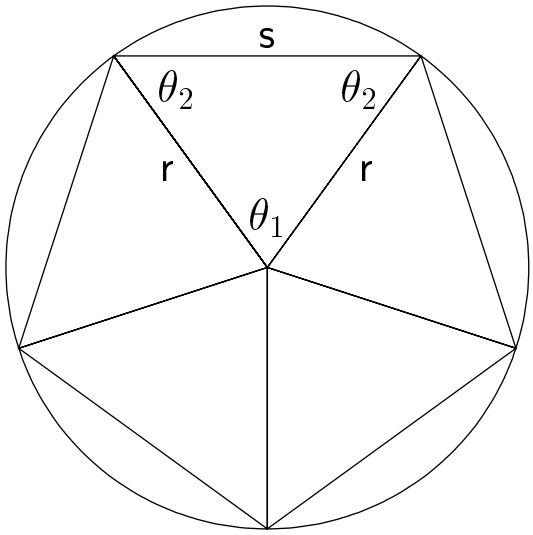

Fig. B.2 A regular polygon inscribed within a circle provides a means for approximating the circle's perimeter with a given resolution. Standard trigonometry yields a relation between the number of edges of the polygon and their size, and therefore yields the perimeter of the polygon.

the angle formed at the center of the circle. Since all n of these angles together subtend an angle of 2π, we have $\theta_1 = 2\pi/n$. For isosceles triangles, the other two angles θ_2 must each equal $\pi/2 - \pi/n$, since all three angles must sum to π. The sine theorem for triangles states that the ratio of two sides equals the ratio of the sines of the opposite angles, yielding

$$\begin{aligned} \frac{\mathsf{s}}{\mathsf{r}} &= \frac{\sin(\theta_1)}{\sin(\theta_2)} \\ \frac{\mathsf{s}}{(2\pi)^{-1}} &= \frac{\sin(2\pi/n)}{\sin(\pi/2 - \pi/n)} \\ \mathsf{s} &= \frac{\sin(2\pi/n)}{2\pi \sin(\pi/2 - \pi/n)} \\ &= \frac{2\sin(\pi/n)\,\cos(\pi/n)}{2\pi\cos(\pi/n)} \\ n\mathsf{s} &= (n/\pi)\,\sin(\pi/n). \end{aligned} \tag{B.1}$$

Graphs of this function indeed increase as n increases.

Prob. 1.2.2 A circle is *not* a fractal, however, since the perimeter does not increase significantly as the resolution increases. In the limit of a large number of sides n,

Eq. (B.1) becomes

$$\begin{aligned} \lim_{n\to\infty} n\mathsf{s} &= \lim_{n\to\infty} (n/\pi)\,\sin(\pi/n) \\ &= \lim_{x\to 0} \sin(x)/x \\ &= 1. \end{aligned} \tag{B.2}$$

As the number of sides n increases, s decreases in concert. Concurrently, the perimeter approaches unity, the value of the circle itself, as it must. Therefore, the estimated perimeter varies between $2/\pi$ for two segments (each of length $1/\pi$) and unity for infinitesimal segments: an increase of only 57%. For a fractal, in contrast, the perimeter changes dramatically over a broad range of measurement resolutions.

B.2 SCALING, FRACTALS, AND CHAOS

Prob. 2.1

1. Yes: circulatory systems comprise branches and sub-branches, with parts resembling the whole over a range of branchings.
2. Yes: again, each branching yields smaller random copies of the original.
3. No: with all hair strands essentially the same diameter and length, these two scales dominate and no scaling behavior emerges.
4. No: except for possible surface roughness or percolating pores, a brick essentially forms a simple rectangular prism.
5. No: steady winds of constant velocity sort sand grains by size and impart regular ripples to the sand; with only these two scales present, fractal characteristics do not occur.
6. Yes: clouds generally have borders with fractal characteristics and resemble coastlines in many respects.
7. Yes: mountain ranges have mountains and foothills, each with smaller features of similar shape, and so forth; horizontal slices (contours) of mountain ranges themselves take fractal form — similar slices at sea level determine coastlines, which take fractal forms as we have seen.
8. No: with or without air resistance included, the path of the ball forms a simple curve without fractal features; air turbulence results in slight variations in the path, but only negligible ones.
9. No: the added noise effectively destroys the self-similar structure of the set of line segments; examining the final result *a posteriori*, one cannot know of the exact self-similarity employed in the construction of the set $\mathcal{C}_3$ *a priori*, before adding the noise.

Prob. 2.2.1 Proceeding directly from Eq. (2.31) yields

$$\begin{aligned} y &\equiv \pi^{-1} \arccos(1-2x) \\ \cos(\pi y) &= 1-2x \\ x &= \tfrac{1}{2}[1-\cos(\pi y)]. \end{aligned} \tag{B.3}$$

Substituting Eq. (B.3) into Eq. (2.20) with $c = 4$ leads to

$$\begin{aligned} x_{n+1} &= 4x_n(1-x_n) \\ \tfrac{1}{2}\big[1-\cos(\pi y_{n+1})\big] &= 4 \times \tfrac{1}{2}\big[1-\cos(\pi y_n)\big] \times \Big(1-\tfrac{1}{2}\big[1-\cos(\pi y_n)\big]\Big) \end{aligned}$$

$$\begin{aligned}
\tfrac{1}{2}\left[1-\cos(\pi y_{n+1})\right] &= 1-\cos^2(\pi y_n) \\
\cos(\pi y_{n+1}) &= 2\cos^2(\pi y_n)-1 \\
&= \cos^2(\pi y_n)-\sin^2(\pi y_n) \\
&= \cos(2\pi y_n), \qquad \text{(B.4)}
\end{aligned}$$

which yields results identical to Eq. (2.32).

Prob. 2.2.2 Equation (2.32) states that the values of y effectively experience a doubling at each iteration. This ignores the sign of the transformation in Eq. (2.32), which becomes irrelevant for estimates of absolute values in any case. This simply yields $|\epsilon_{n+1}/\epsilon_n| = 2$, which is exactly the same as for the original expression in x, Eq. (2.20). The two must assume the same values, since a monotonic transformation cannot change the ratio of perturbations (Ott, 2002).

Prob. 2.3.1 Essentially the same argument applies to $\mathcal{C}'$ as to $\mathcal{C}$. Since we remove the middle half from each interval, the total width or Lebesgue measure of $\mathcal{C}'_n$ assumes the value 2^{-n}, which also approaches zero as n increases. In the limit $n \to \infty$, we have a width of zero for $\mathcal{C}'$ just as for $\mathcal{C}$.

Prob. 2.3.2 Again, similar arguments apply. This time a *quaternary* expansion proves useful, with points having only 0 and 3 in their expansions (except for endpoints) belonging to $\mathcal{C}'$, and others not. The same one-to-one mapping to the original unit interval exists, showing that the number of points in the unit interval, in $\mathcal{C}'$, and in $\mathcal{C}$ for that matter, all coincide.

Prob. 2.3.3 Since each stage in the construction of $\mathcal{C}'$ yields twice as many intervals, each one quarter the size of the original, we find that decreasing ϵ by a factor of 4 yields a corresponding increase in $N(\epsilon)$ of a factor of 2. Employing the scaling equation $N(\epsilon) \sim \epsilon^{-D_0}$, we obtain $D_0 = \log(2)/\log(4) = \frac{1}{2}$, exactly.

Prob. 2.4.1 Solving for x we obtain

$$\begin{aligned}
x &\equiv 0.002002\ldots_3 \\
27x &= 2.002002\ldots_3 \\
26x &= 2 \qquad \text{(B.5)} \\
x &= 2/26 \\
&= 1/13, \qquad \text{(B.6)}
\end{aligned}$$

where Eq. (B.5) results from the difference between the two lines above it.

Prob. 2.4.2 All endpoints of $\mathcal{C}$ have terminating ternary expansions. Since the ternary expansion for x does not terminate, but rather persists indefinitely, x does not belong to the endpoints of $\mathcal{C}$.

Prob. 2.4.3 Since the ternary expansion of x has no 1's in it, x must belong to $\mathcal{C}$. Since we have established that x does not belong to the endpoints of $\mathcal{C}$, x must belong to the interior of $\mathcal{C}$.

Prob. 2.4.4 An uncountably infinite number of irrational values belong to $\mathcal{C}$, since $\mathcal{C}$ comprises an uncountably infinite number of values and only a countable number of them belong to the rational numbers. The value $x = 0.022020200020\ldots_3$, where $a_k = 2$ if k is prime and zero if not, forms one such example.

Prob. 2.5 Setting $x = 1$ in Eq. (2.4) yields

$$f(a) = g(a)\, f(1) \tag{B.7}$$

Substituting Eq. (B.7) back into Eq. (2.4), we obtain

$$\begin{aligned} g(ax)\, f(1) &= g(a)\, g(x)\, f(1) \\ g(ax) &= g(a)\, g(x). \end{aligned} \tag{B.8}$$

Defining

$$\begin{aligned} g_2(x) &\equiv \ln\bigl\{g\bigl[\exp(x)\bigr]\bigr\} \\ a' &\equiv \ln(a) \\ x' &\equiv \ln(x) \end{aligned} \tag{B.9}$$

and substituting Eq. (B.9) into Eq. (B.8) yields

$$\begin{aligned} \exp\bigl\{g_2\bigl[\ln(ax)\bigr]\bigr\} &= \exp\bigl\{g_2\bigl[\ln(a)\bigr]\bigr\}\, \exp\bigl\{g_2\bigl[\ln(x)\bigr]\bigr\} \\ g_2\bigl[\ln(ax)\bigr] &= g_2\bigl[\ln(a)\bigr] + g_2\bigl[\ln(x)\bigr] \\ g_2(a' + x') &= g_2(a') + g_2(x'). \end{aligned} \tag{B.10}$$

Equation (B.10) demonstrates that $g_2(\cdot)$ belongs to the class of linear functions, so that

$$\begin{aligned} g_2(x') &= \ln(c)\, x' \\ g(x) &= x^c \\ f(x) &= b\, x^c, \end{aligned} \tag{B.11}$$

in accord with Eqs. (2.5) and (2.6).

B.3 POINT PROCESSES: DEFINITION AND MEASURES

Prob. 3.1 An orderly, one-dimensional point process provides a useful model for examples 2, 3, 7, 8, and 9, despite the extremes of example 8, which has an average rate of well over 1 billion events/sec, and example 9, in which there is only one interval. The orderly, one-dimensional point-process model fails for the other examples for a variety of reasons. A *two*-dimensional point process describes example 1, and considering either the latitude or longitude (but not both) would yield an example amenable to the model of an orderly, one-dimensional point-process. For example 4, the failure lies in the lack of precise time localization, since thunderstorms arise and dissipate gradually. For the model to apply, one could instead consider the times of lightning strikes. A similar argument applies to example 5; considering the times at which cars pass a specified point, such as the toll booth, would render the model applicable. Example 6 contains an infinite number of events in a finite interval, and therefore has an infinite rate; in particular, any rate estimate diverges near the origin. No orderly point process can model this set. Restricting the integers n to lie below a certain maximum value would obviate this limitation. Finally, example 10 has no events at all, either well- or ill-defined. For the model to apply, one could consider the times at which the sign of the difference changes.

Prob. 3.2 In the limit as $T \to 0$, Eq. (3.33) indicates that the probability of two or more events occurring within a counting time becomes very small. This makes sense, since smaller durations tend to contain fewer events. Given the approximation $\Pr\{Z(T) > 1\} \approx 0$, the count random variable $Z(T)$ almost always takes one of two values: zero or unity. In both cases, $Z^2(T) = Z(T)$. Including the rare cases when $Z(T) > 1$ gives $Z^2(T) \approx Z(T)$. Taking expectations of both sides then yields $\mathrm{E}\left[Z^2(T)\right] \approx \mathrm{E}[Z(T)]$, as we set out to prove.

Prob. 3.3 Combine Eqs. (3.11) and (3.29), and proceed to take two derivatives:

$$\begin{aligned}
\Pr\{Z(t)=0\} &= 1 - P_\vartheta(t) \\
&= 1 - \frac{1}{\mathrm{E}[\tau]} \int_0^t [1 - P_\tau(x)]\, dx \\
\frac{d}{dt}\, \Pr\{Z(t)=0\} &= -\frac{1}{\mathrm{E}[\tau]}\, [1 - P_\tau(t)] \\
\frac{d^2}{dt^2}\, \Pr\{Z(t)=0\} &= -\frac{1}{\mathrm{E}[\tau]}\, [-p_\tau(t)] \\
\mathrm{E}[\tau]\, \frac{d^2}{dt^2}\, \Pr\{Z(t)=0\} &= p_\tau(t). \qquad \text{(B.12)}
\end{aligned}$$

Prob. 3.4 For $Z(t) = 0$, we require that no events occur in an interval of duration t. Alternately, we can say that the time to the next event, starting at the beginning of the interval of duration t, exceeds t. In terms of the forward recurrence time ϑ,

we have $\vartheta > t$. Taking probabilities, we have that $\Pr\{Z(t) = 0\} = \Pr\{\vartheta > t\}$. But by the definition of the probability distribution function, $P_\vartheta(t) \equiv \Pr\{\vartheta \leq t\} = 1 - \Pr\{\vartheta > t\}$. Combining these two expressions yields Eq. (3.29).

Prob. 3.5 For arbitrary intervals, there is no restriction on the skewness, which can take any value from negative to positive infinity, inclusive. The kurtosis can also attain arbitrarily large positive values, but a lower limit exists. Since the kurtosis does not depend on the absolute scale of a distribution, we can choose zero mean and unit variance without loss of generality. We define a reduced variable x with these statistics,

$$x \equiv \frac{\tau - \mathrm{E}[\tau]}{\sigma_\tau}, \tag{B.13}$$

so that the kurtosis of τ simplifies to

$$\mathrm{E}[(\tau - \mathrm{E}[\tau])^4]/\sigma_\tau^4 - 3 \to \mathrm{E}[x^4] - 3. \tag{B.14}$$

Now define $y \equiv x^2$, and consider

$$\begin{aligned} \mathrm{E}[x^4] &= \mathrm{E}[y^2] \\ &= \mathrm{E}^2[y] + \mathrm{Var}[y] \\ &\leq \mathrm{E}^2[y] \\ &= \mathrm{E}^2[x^2] \\ &= 1. \end{aligned} \tag{B.15}$$

Combining Eqs. (B.14) and (B.15) therefore provides

$$\mathrm{E}[(\tau - \mathrm{E}[\tau])^4]/\sigma_\tau^4 - 3 \leq 1 - 3 = -2. \tag{B.16}$$

To achieve this lower limit, we require a random variable with zero mean, unit variance, and (constant) unit square. We then have $x = +1, -1$, with equal probability, as the only solution. In terms of the original variable τ, we may choose any two values as long as they each occur with probability $1/2$. In this case, the general probability density function takes the form

$$p_\tau(t) = \frac{\delta(t-a) + \delta(t-b)}{2} \tag{B.17}$$

for arbitrary (but distinct) values a and b.

Restricting τ to assume nonnegative values actually changes these ranges very little. The kurtosis retains its negative limit of -2 as well as its upper limit of positive infinity. Positive values of skewness derive from tails in positive values of τ, which does not change. To achieve negative skewness values, we can truncate a distribution of τ at some large negative number, and then increase the mean by that same number, resulting in a distribution with nearly the same negative skewness but limited to positive interevent intervals. In this manner one can generate any desired negative skewness except for negative infinity.

Prob. 3.6 Proceeding directly from the definition in Eq. (3.13), and using a change of variable $x = t_0/t$, we have

$$\begin{aligned} \mathrm{E}[\tau^c] &= \int_0^\infty t^c \sqrt{t_0/\pi}\ t^{-3/2}\ \exp(-t_0/t)\, dt \\ &= \int_0^\infty t_0^c\, x^{-c} \sqrt{t_0/\pi}\ t_0^{-3/2}\, x^{3/2}\, e^{-x}\, t_0\, x^{-2}\, dx \\ &= \frac{t_0^c}{\sqrt{\pi}} \int_0^\infty x^{-1/2-c}\, e^{-x}\, dx \qquad \text{(B.18)} \\ &= \pi^{-1/2}\, \Gamma(\tfrac{1}{2} - c)\, t_0^c, \qquad \text{(B.19)} \end{aligned}$$

for c sufficiently small, where $\Gamma(\cdot)$ again denotes the Eulerian gamma function [see Eq. (4.44)]. Moments of τ do not exist for positive integers c since the integral in Eq. (B.18) diverges near the origin for those exponents. For exponents less than or equal to -1, the integral in Eq. (B.18) has infinite area near the origin and therefore diverges. For convergence, we thus require $-\frac{1}{2} - c > -1$, or $c < \frac{1}{2}$. Hence, all moments of order c less than one half exist, including fractional moments between zero and one half as well as negative-integer moments.

Prob. 3.7 Employing the properties of regular Brownian motion, as discussed in Sec. 2.4.2, proves especially helpful. The rescaled range statistic and detrended fluctuation analysis both employ a summed version of the input series. For large k, and intervals with finite variance, the resulting sums will converge to a Gaussian distribution as a result of the central limit theorem. Thus, the sums approach regular Brownian motion. We know from Sec. 2.4.2 that scaling the time by a factor c is equivalent to scaling the amplitude by a factor $\sqrt{c}$. In terms of a sum of intervals, the case of interest here, the independent variable changes from time to the number of intervals. Both the rescaled range statistic and detrended fluctuation analysis yield results that derive from the amplitude of the process: a normalized difference for the former statistic, and an average root-mean-square deviation for the latter. So increasing the independent variable by a factor c will similarly increase the resulting statistics by a factor $\sqrt{c}$. Setting $c = k$, we conclude that both statistics scale as $\sqrt{k}$.

Prob. 3.8 The forward recurrence time is defined as the time remaining to the next event, starting at a time t_0 independent of the process. This time t_0 lies within some interevent interval τ, with the probability density of that interval proportional to $sp_\tau(s)$; the form $p_\tau(s)$ itself denotes the probability density of the times between events. The additional factor of s arises because this form of sampling (time-based rather than interval-based) preferentially selects longer intervals, in proportion to their duration. (To see this, consider a simple example where interevent intervals of durations 1 and 2 exist in equal numbers. A time selected at random will lie within an interval of duration 2 twice as often as one of duration 1.) Normalizing this interevent interval yields a probability density of $sp_\tau(s)/\mathrm{E}[\tau]$.

Since we selected the time t_0 independently of the point process, given the interval τ, we have no other information about where within this interval t_0 occurs. Thus,

the time remaining between t_0 and the next event of the point process (the forward recurrence time) has a uniform distribution $1/s$, given that $s = \tau$. To evaluate the forward recurrence-time probability density at t, we integrate over all times that remain possible (greater than t). Taken together, we have

$$\begin{aligned} p_\vartheta(t) &= \int_t^\infty (1/s) \left\{ s p_\tau(s) / \mathrm{E}[\tau] \right\} ds \\ &= \frac{1}{\mathrm{E}[\tau]} \int_t^\infty p_\tau(s)\, ds \\ &= \frac{1}{\mathrm{E}[\tau]} \left[1 - P_\tau(t)\right] \\ P_\vartheta(t) &= \frac{1}{\mathrm{E}[\tau]} \int_0^t \left[1 - P_\tau(s)\right]\, ds, \end{aligned} \tag{B.20}$$

which is precisely Eq. (3.11). See Cox & Isham (1980, pp. 7–8) for a related approach.

Prob. 3.9 Imagine an almost periodic series of events. We represent the interevent intervals τ_k as a perturbation about the mean value

$$\tau_k = \mathrm{E}[\tau]\,(1 + \epsilon_k), \tag{B.21}$$

where the sequence of dimensionless random variables $\{\epsilon_k\}$ represents the relative deviations of each interevent interval from the mean. Since we assume that the sequence $\{\epsilon_k\}$ remains small, we can adequately describe the point process in terms of a local rate, λ_k:

$$\begin{aligned} \lambda_k(\mathrm{E}[\tau]) &= 1/\tau_k \\ &= \left\{ \mathrm{E}[\tau]\,(1 + \epsilon_k) \right\}^{-1} \\ &= \mathrm{E}[\mu]/(1 + \epsilon_k) \\ &\approx \mathrm{E}[\mu] - \mathrm{E}[\mu]\,\epsilon_k. \end{aligned} \tag{B.22}$$

Ignoring the constant term $\mathrm{E}[\mu]$ (which only affects the spectrum at zero frequency), and recalling that multiplying a sequence by a constant changes its spectrum by the square of that constant, we arrive at

$$S_\lambda\left(f/\mathrm{E}[\mu]\right) \approx \mathrm{E}^2[\mu]\, S_\epsilon(\mathsf{f}). \tag{B.23}$$

For the interval-based spectrum, Eq. (B.21) leads to a similar result:

$$S_\tau(\mathsf{f}) = \mathrm{E}^2[\tau]\, S_\epsilon(\mathsf{f}). \tag{B.24}$$

Combining Eqs. (3.67), (B.23), and (B.24) leads to

$$S_\tau(\mathsf{f}) \approx \pi^{-2}\, \mathrm{E}^2[\tau]\; f^{-2}\, (\pi f\, \mathrm{E}[\tau])^2\; S_N(f/\,\mathrm{E}[\mu])\,, \tag{B.25}$$

where we have made use of the relation $\sin(\pi f\,\mathrm{E}[\tau]) \approx \pi f\,\mathrm{E}[\tau]$ for low frequencies f (see Prob. 3.13). Finally, Eq. (B.25) simplifies to

$$S_\tau(\mathsf{f}) \approx \mathrm{E}^4[\tau]\, S_N(f/\,\mathrm{E}[\mu])\,. \tag{B.26}$$

Prob. 3.10 Beginning with the definition of $F(T)$ provided in Eq. (3.32), we have

$$\begin{aligned} F(T) &\equiv \frac{\mathrm{E}\big[Z^2(T)\big] - \mathrm{E}^2[Z(T)]}{\mathrm{E}[Z(T)]} \\ \mathrm{E}[Z(T)]\,F(T) &= \mathrm{E}\big[Z^2(T)\big] - \mathrm{E}^2[Z(T)] \\ \mathrm{E}[\mu]\,T\,F(T) &= \mathrm{E}\left[\int_{s=0}^{T}\int_{t=0}^{T} dN(s)\,dN(t)\right] - \mathrm{E}^2[\mu]\,T^2 \\ &= \int_{s=0}^{T}\int_{t=0}^{T} G(t-s)\,ds\,dt - \mathrm{E}^2[\mu]\,T^2. \end{aligned} \tag{B.27}$$

Defining

$$u \equiv t - s \quad \text{and} \quad v \equiv t + s, \tag{B.28}$$

we obtain

$$ds\,dt = du\,dv/\,2. \tag{B.29}$$

Substituting Eqs. (B.28) and (B.29) into Eq. (B.27) we obtain

$$\begin{aligned} \mathrm{E}[\mu]\,T\,F(T) &= \int_{u=-T}^{T}\int_{v=|u|-T}^{T-|u|} G(u)\,du\,dv/\,2 - \mathrm{E}^2[\mu]\,T^2 \\ &= \int_{u=-T}^{T} (T-|u|)\,G(u)\,du - \mathrm{E}^2[\mu]\,T^2 \\ &= \int_{u=-T}^{T} (T-|u|)\,\big\{G(u) - \mathrm{E}^2[\mu]\big\}\,du. \end{aligned} \tag{B.30}$$

Prob. 3.11 We begin with the inverse Fourier transform relationship between $G(t)$ and $S_N(f)$ provided in Eq. (3.58), and keep in mind that the constant term $\mathrm{E}^2[\mu]$ in the coincidence rate corresponds to a delta function $\mathrm{E}^2[\mu]\,\delta(f)$ at zero frequency in the spectrum

$$\begin{aligned} G(u) &= \int_{f=-\infty}^{\infty} S_N(f)\,\exp(i2\pi f u)\,df \\ &= \int_{f=-\infty}^{\infty} S_N(f)\,\cos(2\pi f u)\,df \\ G(u) - \mathrm{E}^2[\mu] &= \int_{f=-\infty}^{\infty} \big\{S_N(f) - \mathrm{E}^2[\mu]\,\delta(f)\big\}\cos(2\pi f u)\,df \\ &= 2\int_{f=0+}^{\infty} S_N(f)\,\cos(2\pi f u)\,df. \end{aligned} \tag{B.31}$$

Reiterating Eq. (B.30) and making use of Eq. (B.31) yields

$$\begin{aligned}
\mathrm{E}[\mu]\,T\,F(T) &= \int_{u=-T}^{T} (T-|u|)\left\{G(u)-\mathrm{E}^2[\mu]\right\}\,du \\
&= 2\int_{u=-T}^{T} (T-|u|)\int_{f=0+}^{\infty} S_N(f)\,\cos(2\pi f u)\,df\,du \\
&= 2\int_{f=0+}^{\infty} S_N(f)\int_{u=-T}^{T} (T-|u|)\,\cos(2\pi f u)\,du\,df \\
&= \int_{f=0+}^{\infty} 4\,T^2\,S_N(f)\int_{x=0}^{1} (1-x)\,\cos(2\pi f T x)\,dx\,df \\
&= \int_{f=0+}^{\infty} 4\,T^2\,S_N(f)\Big[(2\pi f T)^{-1}\,(1-x)\,\sin(2\pi f T x) \\
&\qquad -(2\pi f T)^{-2}\,\cos(2\pi f T x)\Big]_{x=0}^{1}\,df \\
&= \int_{f=0+}^{\infty} \frac{4T^2}{(2\pi f T)^2}\,S_N(f)\big[1-\cos(2\pi f T)\big]\,df \\
&= \int_{f=0+}^{\infty} \frac{1}{\pi^2 f^2}\,S_N(f)\,2\sin^2(\pi f T)\,df \\
&= \frac{2}{\pi^2}\int_{0+}^{\infty} S_N(f)\,\sin^2(\pi f T)\,f^{-2}\,df. \qquad \text{(B.32)}
\end{aligned}$$

Prob. 3.12 Here we employ Eq. (3.41), and make use of Eq. (3.61), which we proved immediately above [see Eq. (B.32)]:

$$\begin{aligned}
A(T) &= 2F(T)-F(2T) \\
&= \frac{4}{\pi^2\,\mathrm{E}[\mu]\,T}\int_{0+}^{\infty} S_N(f)\,\sin^2(\pi f T)\,f^{-2}\,df \\
&\qquad -\frac{2}{\pi^2\,\mathrm{E}[\mu]\,2T}\int_{0+}^{\infty} S_N(f)\,\sin^2(2\pi f T)\,f^{-2}\,df \\
&= \frac{1}{\pi^2\,\mathrm{E}[\mu]\,T}\int_{0+}^{\infty} S_N(f)\,\Big[4\sin^2(\pi f T)-\sin^2(2\pi f T)\Big]\,f^{-2}\,df \\
&= \frac{1}{\pi^2\,\mathrm{E}[\mu]\,T}\int_{0+}^{\infty} S_N(f)\,\Big[4\sin^2(\pi f T) \\
&\qquad -4\sin^2(\pi f T)\,\cos^2(\pi f T)\Big]\,f^{-2}\,df \\
&= \frac{4}{\pi^2\,\mathrm{E}[\mu]\,T}\int_{0+}^{\infty} S_N(f)\sin^2(\pi f T)\,\big[1-\cos^2(\pi f T)\big]\,f^{-2}\,df \\
&= \frac{4}{\pi^2\,\mathrm{E}[\mu]\,T}\int_{0+}^{\infty} S_N(f)\,\sin^4(\pi f T)\,f^{-2}\,df. \qquad \text{(B.33)}
\end{aligned}$$

Prob. 3.13 Conversion of the point process $dN(t)$ into a rate $\lambda_k(T)$ involves two operations taken in sequence: averaging and sampling. We consider each in turn, and examine how they affect the spectrum.

The first step involves averaging $dN(t)$ over a time T. We can cast this operation as filtering by a simple rectangular form of duration T and height $1/T$, which has an impulse response function

$$h(t) = \begin{cases} 1/T & 0 \le t < T \\ 0 & \text{otherwise.} \end{cases} \tag{B.34}$$

Linear systems theory (Papoulis, 1991) tells us that filtering a point process changes the power spectral density by a factor equal to the square magnitude of the Fourier transform of the impulse response function [see Eq. (9.35)]. In this case we have

$$\begin{aligned} \mathcal{F}\{h(t)\} &\equiv \int_{t=-\infty}^{\infty} h(t)\, \exp(-i2\pi ft)\, df \\ &= \int_0^T (1/T)\, \exp(-i2\pi ft)\, df \\ &= [1 - \exp(-i2\pi fT)]\,/(i2\pi fT) \\ &= \exp(-i\pi fT)\, [\exp(i\pi fT) - \exp(-i\pi fT)]\,/(i2\pi fT) \\ &= \exp(-i\pi fT)\, \sin(\pi fT)/(\pi fT) \\ \left|\mathcal{F}\{h(t)\}\right|^2 &= \sin^2(\pi fT)/(\pi fT)^2. \end{aligned} \tag{B.35}$$

(The same result can be obtained, but with additional effort, by using the methods employed in Probs. 3.10 and 3.11.)

If we let $X(t)$ denote the averaged process thus defined, its spectrum becomes

$$S_X(f) = S_N(f) \sin^2(\pi fT)/(\pi fT)^2. \tag{B.36}$$

But $X(t)$ exists for all times t, while we have defined $\lambda_k(T)$ as a discrete-time process, defined only for integer values of k. Converting $X(t)$ into $\lambda_k(T)$ involves sampling at a time interval of T. Discrete-time processes have periodic spectra, spaced a frequency $1/T$ apart; this leads to aliasing when the component spectra overlap. In terms of the spectrum of the averaged process, we have

$$S_\lambda(f, T) = \sum_{k=-\infty}^{\infty} S_X(f + k/T). \tag{B.37}$$

Combining Eqs. (B.36) and (B.37) yields Eq. (3.67), where we have made use of the simplification

$$\sin(\theta + n\pi) = (-1)^n \sin(\theta). \tag{B.38}$$

To evaluate Eq. (3.67) for small values of fT, we employ the relation $\sin(\theta) \approx \theta$ for small θ, verified by l'Hôpital's rule. Reiterating Eq. (3.67) and employing this

approximation yields

$$\begin{aligned} S_\lambda(f,T) &= \sum_{k=-\infty}^{\infty} S_N(f+k/T)\frac{\sin^2(\pi fT)}{(\pi fT+\pi k)^2} \\ &\approx \sum_{k=-\infty}^{\infty} S_N(f+k/T)\frac{(\pi fT)^2}{(\pi fT+\pi k)^2} \\ &= \sum_{k=-\infty}^{\infty} \frac{S_N(f+k/T)}{[1+k/(fT)]^2}. \end{aligned} \tag{B.39}$$

For small values of the product fT, the denominator in Eq. (B.39) assumes quite large values for $k \neq 0$, making these terms quite small. The term corresponding to $k = 0$ then dominates, and we have $S_\lambda(f,T) \approx S_N(f)$.

B.4 POINT PROCESSES: EXAMPLES

Prob. 4.1.1 A counting window of duration $T = n\tau$ contains exactly n events regardless of the starting time of the window. The randomness inherent in the point process makes interpolation between integer multiples of τ possible, so that for arbitrary T we have

$$Z(T) = \begin{cases} \text{int}(T/\tau) & \text{with probability} \quad 1-p \\ \text{int}(T/\tau)+1 & \text{with probability} \quad p, \end{cases} \tag{B.40}$$

where $\text{int}(x)$ denotes the largest integer not exceeding x and

$$p \equiv T/\tau - \text{int}(T/\tau) \tag{B.41}$$

represents the probability of the larger count. For the mean number of counts, we have the simple result

$$\text{E}[Z(T)] = T/\tau \tag{B.42}$$

common to all point processes (with $\text{E}[\tau] = \tau$ in this case). We employ Eqs. (B.40)–(B.42) to find the variance

$$\begin{aligned} \text{Var}[Z(T)] &= (1-p)\big[\text{int}(T/\tau) - T/\tau\big]^2 + p\,\big[\text{int}(T/\tau)+1-T/\tau\big]^2 \\ &= (1-p)p^{\,2} + p\,(1-p)^2 \\ &= p\,(1-p), \end{aligned} \tag{B.43}$$

where p is defined in Eq. (B.41). The function $p\,(1-p)$ indeed achieves a maximum value of $\frac{1}{4}$ for $p = \frac{1}{2}$.

Prob. 4.1.2 Dividing Eq. (B.43) by Eq. (B.42) yields the normalized variance $F(T)$:

$$\begin{aligned} F(T) &= \text{Var}[Z(T)]/\,\text{E}[Z(T)] \\ &= p\,(1-p)\,\tau/\,T \\ &= \big[T/\,\tau - \text{int}(T/\,\tau)\big]\,\big[\text{int}(T/\,\tau)+1-T/\,\tau\big]\big[\tau/\,T\big]. \end{aligned} \tag{B.44}$$

Prob. 4.2.1 To find the forward recurrence-time probability density, we make use of Eq. (3.12). Substituting Eq. (4.3) for $p_\tau(t)$ yields the result for the homogeneous Poisson process:

$$\begin{aligned} p_\vartheta(t) &= [1 - P_\tau(t)]\,/\,\text{E}[\tau] \\ &= \left[1 - \int_0^t \mu\,\exp(-\mu s)\,ds\right]\mu \\ &= \mu\Big\{1 - \big[1 - \exp(-\mu t)\big]\Big\} \\ &= \mu\,\exp(-\mu t) \\ &= p_\tau(t), \end{aligned} \tag{B.45}$$

so that the forward recurrence-time probability density is identical to the interevent-interval density for this process.

Prob. 4.2.2 Since v can lie anywhere within an interevent interval, the time to the events at either end must have the same statistics. Hence, the backward recurrence-time probability density is the same as the forward recurrence-time probability density, which was derived in Eq. (B.45) above.

Prob. 4.2.3 The forward recurrence time and the backward recurrence time together comprise the interevent interval surrounding v; their sum becomes that interval. As a result of the memoryless nature of the homogeneous Poisson process, these two times are independent. The convolution of the probability densities of two independent random variables provides the probability density of their sum. Recalling that τ_* denotes the interval within which v lies, we obtain

$$\begin{aligned} p_{\tau *}(t) &= p_\tau(t) \star p_\tau(t) \\ &= \int_0^t p_\tau(s)\, p_\tau(t-s)\, ds \\ &= \int_0^t \mu\, \exp(-\mu s)\, \mu\, \exp[-\mu(t-s)]\, ds \\ &= \mu^2 \int_0^t \exp(-\mu t)\, ds \\ &= \mu^2 t\, \exp(-\mu t). \end{aligned} \tag{B.46}$$

Prob. 4.2.4 The two probability densities, Eqs. (B.46) and (4.3), do indeed differ. For example, the mean interevent interval associated with Eq. (B.46) calculates to

$$\begin{aligned} \mathrm{E}[\tau_*] &= \int_0^\infty t\, p_{\tau *}(t)\, dt \\ &= \int_0^\infty t\, \mu^2\, t\, \exp(-\mu t)\, dt \\ &= \mathrm{E}[\tau] \int_0^\infty x^2\, \exp(-x)\, dx \\ &= 2\mathrm{E}[\tau], \end{aligned} \tag{B.47}$$

twice the value for the homogeneous Poisson process. The difference lies in how the intervals are selected. For the conventional interevent-interval probability density, $p_\tau(t)$, each interval is weighted equally. But to obtain the statistics of the interval spanning the time v, larger intervals are selected preferentially. In fact, the larger the interval, the more likely we select it, leading to the extra factor of t in Eq. (B.46); normalization to unity area yields the exact form of Eq. (B.46). Additional information pertinent to this issue can be found in the solution to Prob. 3.8.

Prob. 4.3 We begin with $q = 0$. For a particular value of T, the sum will have L/T terms. Each $Z_k(T)$ assumes a value of zero with probability $\exp(-\mu T)$, as provided by Eq. (4.7); this corresponds to an empty box. A full box then occurs with probability $1 - \exp(-\mu T)$. Multiplying this latter probability by the number of terms yields

$$\mathrm{E}\left[\sum_k Z_k^0(T)\right] = (L/T)\,[1 - \exp(-\mu T)]. \tag{B.48}$$

In the limit of small T, using Eq. (B.48) together with l'Hôpital's rule gives rise to

$$\begin{aligned}
\lim_{T\to 0} \mathrm{E}\left[\sum_k Z_k^0(T)\right] &= \lim_{T\to 0} \frac{1 - \exp(-\mu T)}{T/L} \\
&= \lim_{T\to 0} \frac{\mu \exp(-\mu T)}{1/L} \\
&= \mu L \\
&= \mathrm{E}[N(L)],
\end{aligned} \tag{B.49}$$

a constant value. In connection with Eq. (3.70) we obtain $D_0 = 0$, as we must for a finite collection of points. For large T the exponential function in Eq. (B.48) vanishes so that we have L/T. Using this latter form in conjunction with Eq. (3.72) yields $D_0 = 1$ for this scaling region, as expected for a nonfractal process.

For $q = 2$ we obtain

$$\begin{aligned}
\mathrm{E}\left[\sum_k Z_k^2(T)\right] &= (L/T)\,\mathrm{E}[Z_k^2(T)] \\
&= (L/T)\left\{\mathrm{E}^2[Z_k(T)] + \mathrm{Var}[Z_k(T)]\right\} \\
&= (L/T)\left\{(\mu T)^2 + \mu T\right\} \\
&= \mu L\,(1 + \mu T) \\
&= \mathrm{E}[N(L)]\,(1 + \mu T),
\end{aligned} \tag{B.50}$$

where we have used the particular cases listed immediately after Eq. (4.4). Here the limiting forms emerge more readily; for small T we again obtain $\mathrm{E}[N(L)]$, and for large T the unity term in Eq. (B.50) disappears. Equations (3.70) and (3.72) yield $D_2 = 0$ and $D_2 = 1$, respectively, in agreement with the values obtained for D_0 above.

Prob. 4.4.1 We begin with Eq. (3.6), the characteristic function of the interevent intervals:

$$\phi_\tau(\omega) \equiv \int_0^\infty p_\tau(t)\,\exp(-i\omega t)\,dt$$

$$\begin{aligned} &= \mu(\mu + i\omega)^{-1} \int_0^\infty \exp(-x)\, dx \\ &= \frac{\mu}{\mu + i\omega}\,. \end{aligned} \tag{B.51}$$

For the spectrum, we substitute Eq. (B.51) into Eq. (4.16), to obtain

$$\begin{aligned} S_N(f) &= \mathrm{E}^2[\mu]\,\delta(f) + \mathrm{E}[\mu]\,\mathrm{Re}\left\{\frac{1+\phi_\tau(2\pi f)}{1-\phi_\tau(2\pi f)}\right\} \\ &= \mu^2\,\delta(f) + \mu\,\mathrm{Re}\left\{\frac{1+\mu(\mu+2\pi i f)^{-1}}{1-\mu(\mu+2\pi i f)^{-1}}\right\} \\ &= \mu^2\,\delta(f) + \mu\,\mathrm{Re}\left\{\frac{(\mu+2\pi i f)+\mu}{(\mu+2\pi i f)-\mu}\right\} \\ &= \mu^2\,\delta(f) + \mu\,\mathrm{Re}\left\{\frac{2\mu+2\pi i f}{2\pi i f}\right\} \\ &= \mu^2\,\delta(f) + \mu\,\mathrm{Re}\Big\{-i\mu/(\pi f) + 1\Big\} \\ &= \mu^2\,\delta(f) + \mu, \end{aligned} \tag{B.52}$$

in agreement with Eq. (4.9c). In accordance with Eq. (3.59), the mean rate of the process $\mathrm{E}[\mu] = \lim_{f\to\infty} S_N(f) = \mu$, using the results in Eq. (B.52).

Prob. 4.4.2 Since constants and delta functions interchange under Fourier transforms, Eqs. (4.9c) and (4.9d) form a Fourier-transform pair. Therefore, since Eq. (4.9c) is valid for this process, so must Eq. (4.9d) be valid. Now consider the expectation of two nonoverlapping intervals. For any t_1, t_2, t_3, t_4 satisfying $t_1 < t_2 \le t_3 < t_4$, we have

$$\begin{aligned} &\mathrm{E}\big\{[N(t_4) - N(t_3)]\,[N(t_2) - N(t_1)]\big\} \\ &\quad= \mathrm{E}\left[\int_{s=t3}^{t4} dN(s) \int_{t=t1}^{t2} dN(t)\right] \\ &\quad= \int_{s=t3}^{t4}\int_{t=t1}^{t2} \mathrm{E}[dN(s)\,dN(t)] \\ &\quad= \int_{s=t3}^{t4}\int_{t=t1}^{t2} G(s-t)\,ds\,dt \\ &\quad= \int_{s=t3}^{t4}\int_{t=t1}^{t2} \mu^2\,ds\,dt \qquad \text{(B.53)} \\ &\quad= \left[\int_{s=t3}^{t4} \mu\,ds\right]\left[\int_{t=t1}^{t2} \mu\,dt\right] \\ &\quad= \mathrm{E}\big\{[N(t_4) - N(t_3)]\big\}\,\mathrm{E}\big\{[N(t_2) - N(t_1)]\big\}, \qquad \text{(B.54)} \end{aligned}$$

where Eq. (B.53) follows from the lack of overlap in the two intervals, which prevents the delta function from appearing. Equation (B.54) thus establishes that the

expectation of the product equals the product of the expectations, and therefore that the counts in these disjoint intervals are uncorrelated.

Prob. 4.4.3 Equation (4.2) asserts independence, which implies lack of correlation, but not vice versa. However, a similar argument to that used in the solution of Prob. 4.4.2 yields results for expectations of arbitrary orders:

$$\mathrm{E}\big\{[N(t_4) - N(t_3)]^m\,[N(t_2) - N(t_1)]^n\big\}. \tag{B.55}$$

Taken together, these results establish independence.

Prob. 4.5 Examining Eq. (4.16), we see that low frequencies correspond to small arguments of the characteristic function $\phi_\tau(\omega)$, enabling us to employ a power-series expansion. We next examine the derivatives

$$\begin{aligned}
\frac{d^n}{d\omega^n}\,\phi_\tau(\omega) &= \int_0^\infty p_\tau(t)\,(-it)^n\,e^{-i\omega t}\,dt \\
\frac{d^n}{d\omega^n}\,\phi_\tau(\omega)_{\omega=0} &= \int_0^\infty p_\tau(t)\,(-it)^n\,dt \\
&= (-i)^n\,\mathrm{E}[\tau^n],
\end{aligned} \tag{B.56}$$

which leads to a general property of characteristic functions with finite moments. Turning now to the power-series expansion, we arrive at

$$\begin{aligned}
\phi_\tau(\omega) &= \sum_{n=0}^{\infty}(-i\omega)^n\,\mathrm{E}[\tau^n]/n! \\
&\approx \sum_{n=0}^{2}(-i\omega)^n\,\mathrm{E}[\tau^n]/n! \\
&= 1 - i\omega\,\mathrm{E}[\tau] - \omega^2\,\mathrm{E}[\tau^2]/2.
\end{aligned} \tag{B.57}$$

Finally, substituting Eq. (B.57) into Eq. (4.16) yields

$$\begin{aligned}
&\lim_{f\to 0} S_N(f) \\
&\quad= \mathrm{E}[\mu]\,\lim_{f\to 0}\mathrm{Re}\left\{\frac{1+\phi_\tau(2\pi f)}{1-\phi_\tau(2\pi f)}\right\} \\
&\quad= \mathrm{E}[\mu]\,\lim_{\omega\to 0}\mathrm{Re}\left\{\frac{2 - i\omega\,\mathrm{E}[\tau] - \omega^2\,\mathrm{E}[\tau^2]/2}{i\omega\,\mathrm{E}[\tau] + \omega^2\,\mathrm{E}[\tau^2]/2}\right\} \\
&\quad= \mathrm{E}[\mu]\,\lim_{\omega\to 0}\mathrm{Re}\left\{\frac{2 - i\omega\,\mathrm{E}[\tau] - \omega^2\,\mathrm{E}[\tau^2]/2}{i\omega\,\mathrm{E}[\tau] + \omega^2\,\mathrm{E}[\tau^2]/2}\times\frac{\mathrm{E}[\tau^2]/2 - i\,\mathrm{E}[\tau]/\omega}{\mathrm{E}[\tau^2]/2 - i\,\mathrm{E}[\tau]/\omega}\right\} \\
&\quad= \mathrm{E}[\mu]\,\lim_{\omega\to 0}\mathrm{Re}\left\{\frac{\mathrm{E}[\tau^2] - 2i\,\mathrm{E}[\tau]/\omega - \mathrm{E}^2[\tau] - \omega^2\,\mathrm{E}^2[\tau^2]/4}{\mathrm{E}^2[\tau] + \omega^2\,\mathrm{E}^2[\tau^2]/4}\right\} \\
&\quad= \mathrm{E}[\mu]\,\lim_{\omega\to 0}\frac{\mathrm{E}[\tau^2] - \mathrm{E}^2[\tau] - \omega^2\,\mathrm{E}^2[\tau^2]/4}{\mathrm{E}^2[\tau] + \omega^2\,\mathrm{E}^2[\tau^2]/4}
\end{aligned}$$

$$
\begin{aligned}
&= \mathrm{E}[\mu]\,\frac{\mathrm{E}[\tau^2]-\mathrm{E}^2[\tau]}{\mathrm{E}^2[\tau]} \\
&= \mathrm{E}^3[\mu]\,\mathrm{Var}[\tau], \qquad \text{(B.58)}
\end{aligned}
$$

which is identical to Eq. (4.17).

Prob. 4.6 We begin by substituting $k = 2$ in Eq. (4.19), yielding

$$
\begin{aligned}
&\mathrm{E}\big\{Z(T)\,[Z(T)+1]\big\} \\
&\quad = 2\int_{0-}^{T}(T-t)\,G(t)\,dt \\
&\quad = \int_{-T}^{T}(T-|t|)\,G(t)\,dt + \int_{0-}^{0+}(T-|t|)\,G(t)\,dt \\
&\quad = \int_{-T}^{T}(T-|t|)\,G(t)\,dt + \int_{0-}^{0+}(T-|t|)\,\mathrm{E}[\mu]\,\delta(t)\,dt \\
&\quad = \int_{-T}^{T}(T-|t|)\,G(t)\,dt + T\,\mathrm{E}[\mu]. \qquad \text{(B.59)}
\end{aligned}
$$

For the integral over the infinitesimal region near the origin in Eq. (B.59), we have ignored all of $G(t)$ except for the delta function; see Eq. (3.50). Expressing the variance in terms of Eq. (B.59) leads to

$$
\begin{aligned}
\mathrm{Var}[Z(T)] &= \mathrm{E}\big\{Z(T)\,[Z(T)+1]\big\} - \mathrm{E}^2[Z(T)] - \mathrm{E}[Z(T)] \\
&= \int_{-T}^{T}(T-|t|)\,G(t)\,dt + T\,\mathrm{E}[\mu] - \int_{-T}^{T}(T-|t|)\,\mathrm{E}^2[\mu]\,dt - T\,\mathrm{E}[\mu] \\
&= \int_{-T}^{T}(T-|t|)\,\big\{G(t)-\mathrm{E}^2[\mu]\big\}\,dt, \qquad \text{(B.60)}
\end{aligned}
$$

in agreement with Eq. (4.21).

Prob. 4.7.1 We again begin with Eq. (3.6), the characteristic function of the interevent intervals:

$$
\begin{aligned}
\phi_\tau(\omega) &\equiv \int_0^\infty p_\tau(t)\,\exp(-i\omega\,t)\,dt \\
&= \int_0^\infty [\Gamma(\mathsf{m})]^{-1}\,\tau_0^{-\mathsf{m}}\,t^{\mathsf{m}-1}\,\exp(-t/\tau_0)\,\exp(-i\omega t)\,dt \\
&= [\Gamma(\mathsf{m})]^{-1}\,\tau_0^{-\mathsf{m}}\int_0^\infty t^{\mathsf{m}-1}\,\exp[-(1/\tau_0+i\omega)t]\,dt \\
&= [\Gamma(\mathsf{m})]^{-1}\,\tau_0^{-\mathsf{m}}\,(1/\tau_0+i\omega)^{-\mathsf{m}}\int_0^\infty x^{\mathsf{m}-1}\,\exp(-x)\,dx \\
&= [\Gamma(\mathsf{m})]^{-1}\,(1+i\omega\,\tau_0)^{-\mathsf{m}}\,\Gamma(\mathsf{m}) \\
&= (1+i\omega\,\tau_0)^{-\mathsf{m}}. \qquad \text{(B.61)}
\end{aligned}
$$

Proceeding to Eq. (3.8) we obtain

$$\begin{aligned} C_n &= i^n \frac{d^n}{d\omega^n} \ln\big[\phi_\tau(\omega)\big]_{\omega=0} \\ &= i^n \frac{d^n}{d\omega^n} \ln\big[(1+i\omega\,\tau_0)^{-\mathsf{m}}\big]_{\omega=0} \\ &= (-1)^{n+1}\,\mathsf{m}\,\tau_0^n \frac{d^n}{dx^n} \ln\big[(1+x)\big]_{x=0} \\ &= \Gamma(n)\,\mathsf{m}\,\tau_0^n, \end{aligned} \tag{B.62}$$

and in particular, we have

$$\begin{array}{lcllcl} \text{mean} & = & C_1 & = & \mathsf{m}\,\tau_0 \\ \text{variance} & = & C_2 & = & \mathsf{m}\,\tau_0^2 \\ & & C_3 & = & 2\mathsf{m}\,\tau_0^3 \\ & & C_4 & = & 6\mathsf{m}\,\tau_0^4 \\ \text{skewness} & = & C_3/C_2^{3/2} & = & 2/\sqrt{\mathsf{m}} \\ \text{kurtosis} & = & C_4/C_2^2 & = & 6/\mathsf{m}. \end{array} \tag{B.63}$$

Prob. 4.7.2 For the spectrum, we again substitute Eq. (B.61) into Eq. (4.16) to obtain

$$\begin{aligned} & S_N(f) \\ &= \mathrm{E}^2[\mu]\,\delta(f) + \mathrm{E}[\mu]\,\mathrm{Re}\left\{\frac{1+\phi_\tau(2\pi f)}{1-\phi_\tau(2\pi f)}\right\} \\ &= (\mathsf{m}\,\tau_0)^{-2}\,\delta(f) + (\mathsf{m}\,\tau_0)^{-1}\,\mathrm{Re}\left\{\frac{1+(1+2\pi i f\tau_0)^{-\mathsf{m}}}{1-(1+2\pi i f\tau_0)^{-\mathsf{m}}}\right\} \\ &= (\mathsf{m}\,\tau_0)^{-2}\,\delta(f) + (\mathsf{m}\,\tau_0)^{-1}\,\mathrm{Re}\left\{\frac{(1+i\theta)^{\mathsf{m}}+1}{(1+i\theta)^{\mathsf{m}}-1} \times \frac{(1-i\theta)^{\mathsf{m}}-1}{(1-i\theta)^{\mathsf{m}}-1}\right\} \\ &= (\mathsf{m}\,\tau_0)^{-2}\,\delta(f) + (\mathsf{m}\,\tau_0)^{-1}\,\mathrm{Re}\left\{\frac{(1+\theta^2)^{\mathsf{m}}+(1-i\theta)^{\mathsf{m}}-(1+i\theta)^{\mathsf{m}}-1}{(1+\theta^2)^{\mathsf{m}}-(1-i\theta)^{\mathsf{m}}-(1+i\theta)^{\mathsf{m}}+1}\right\} \\ &= (\mathsf{m}\,\tau_0)^{-2}\,\delta(f) + \frac{(\mathsf{m}\,\tau_0)^{-1}\left[(1+\theta^2)^{\mathsf{m}}-1\right]}{(1+\theta^2)^{\mathsf{m}}-2\mathrm{Re}\{(1+i\theta)^{\mathsf{m}}\}+1}, \end{aligned} \tag{B.64}$$

where we have defined $\theta \equiv 2\pi f\tau_0$ to simplify the notation. The two middle terms in the numerator on the line before Eq. (B.64) form a complex-conjugate pair, so that their difference has only an imaginary component; taking the real part yields zero. If desired, further simplification can be achieved by making use of

$$\begin{aligned} 1+i\theta &= \sqrt{1+\theta^2}\left\{\frac{1}{\sqrt{1+\theta^2}} + \frac{i\theta}{\sqrt{1+\theta^2}}\right\} \\ &= \sqrt{1+\theta^2}\left\{\cos\big[\arctan(\theta)\big] + i\,\sin\big[\arctan(\theta)\big]\right\} \end{aligned}$$

$$
\begin{aligned}
&= \sqrt{1+\theta^2}\,\exp\bigl[i\,\arctan(\theta)\bigr] \\
\bigl(1+i\theta\bigr)^{\mathsf{m}} &= \bigl(1+\theta^2\bigr)^{\mathsf{m}/2}\,\exp\bigl[i\mathsf{m}\,\arctan(\theta)\bigr] \\
\mathrm{Re}\bigl\{\bigl(1+i\theta\bigr)^{\mathsf{m}}\bigr\} &= \bigl(1+\theta^2\bigr)^{\mathsf{m}/2}\,\cos\bigl[\mathsf{m}\,\arctan(\theta)\bigr], \qquad \text{(B.65)}
\end{aligned}
$$

and substituting Eq. (B.65) into Eq. (B.64).

Prob. 4.7.3 We begin by substituting $\mathsf{m} = 2$ into Eq. (B.64)

$$
\begin{aligned}
S_N(f) &= (2\tau_0)^{-2}\,\delta(f) + \frac{(2\tau_0)^{-1}\left[(1+\theta^2)^2-1\right]}{(1+\theta^2)^2 - 2\mathrm{Re}\bigl\{(1+i\theta)^2\bigr\}+1} \\
&= (2\tau_0)^{-2}\,\delta(f) + \frac{(2\tau_0)^{-1}\left[1+2\theta^2+\theta^4-1\right]}{1+2\theta^2+\theta^4 - 2\mathrm{Re}\bigl\{1+2i\theta-\theta^2\bigr\}+1} \\
&= (2\tau_0)^{-2}\,\delta(f) + (2\tau_0)^{-1}\,\frac{2\theta^2+\theta^4}{4\theta^2+\theta^4} \\
&= (2\tau_0)^{-2}\,\delta(f) + (2\tau_0)^{-1}\,\frac{2+(2\pi f\tau_0)^2}{4+(2\pi f\tau_0)^2} \\
&= (2\tau_0)^{-2}\,\delta(f) + (2\tau_0)^{-1}\left[1-\frac{1/2}{1+(\pi f\tau_0)^2}\right]. \qquad \text{(B.66)}
\end{aligned}
$$

We next substitute Eq. (B.66) into Eq. (3.58) to obtain

$$
\begin{aligned}
G(t) &= \int_{-\infty}^{\infty} S_N(f)\,\exp(i2\pi ft)\,df \\
&= \int_{-\infty}^{\infty}\left\{(2\tau_0)^{-2}\,\delta(f) + (2\tau_0)^{-1}\left[1-\frac{1/2}{1+(\pi f\tau_0)^2}\right]\right\}\exp(i\,2\pi ft)\,df \\
&= (2\tau_0)^{-2} + (2\tau_0)^{-1}\,\delta(t) - (4\tau_0)^{-1}\int_{-\infty}^{\infty}\frac{\exp(i2\pi ft)}{1+(\pi f\tau_0)^2}\,df \\
&= (2\tau_0)^{-1}\,\delta(t) + (2\tau_0)^{-2} - (4\tau_0)^{-1}\,(\pi\tau_0)^{-1}\,\pi\exp\bigl(-|2t/\tau_0|\bigr) \\
&= (2\tau_0)^{-1}\,\delta(t) + (2\tau_0)^{-2}\left[1-\exp\bigl(-|2t/\tau_0|\bigr)\right]. \qquad \text{(B.67)}
\end{aligned}
$$

As a next step, substitution of Eq. (B.67) into Eq. (3.52) yields

$$
\begin{aligned}
F(T) &= \frac{1}{\mathrm{E}[\mu]\,T}\int_{-T}^{T}\bigl\{G(t)-\mathrm{E}^2[\mu]\bigr\}\,(T-|t|)\,dt \\
&= \frac{1}{(2\tau_0)^{-1}\,T}\int_{-T}^{T}\Bigl\{(2\tau_0)^{-1}\,\delta(t) + (2\tau_0)^{-2}\left[1-\exp\bigl(-|2t/\tau_0|\bigr)\right] \\
&\qquad - (2\tau_0)^{-2}\Bigr\}\,(T-|t|)\,dt \\
&= 1 - \frac{1}{2\tau_0\,T}\int_{-T}^{T}\exp\bigl(-|2t/\tau_0|\bigr)\,(T-|t|)\,dt
\end{aligned}
$$

$$
\begin{aligned}
&= 1 - \frac{T}{\tau_0}\int_0^1 \exp(-2xT/\tau_0)\,(1-x)\,dx \\
&= 1 - \frac{T}{\tau_0}\left[\frac{\tau_0}{2T} + \frac{\tau_0^2}{4T^2}\,\exp(-2T/\tau_0) - \frac{\tau_0^2}{4T^2}\right] \\
&= \frac{1}{2} + \frac{\tau_0}{4T}\left[1 - \exp(-2T/\tau_0)\right], \qquad \text{(B.68)}
\end{aligned}
$$

and, finally, Eqs. (B.68) and (3.41) lead to

$$
\begin{aligned}
A(T) &= 2F(T) - F(2T) \\
&= 1 + \frac{\tau_0}{2T}\left[1 - \exp(-2T/\tau_0)\right] - \frac{1}{2} - \frac{\tau_0}{8T}\left[1 - \exp(-4T/\tau_0)\right] \\
&= \frac{1}{2} + \frac{\tau_0}{8T}\left[3 + \exp(-4T/\tau_0) - 4\exp(-2T/\tau_0)\right]. \qquad \text{(B.69)}
\end{aligned}
$$

Prob. 4.8.1 For $f = 0$, the fraction in Eq. (3.67) vanishes for all k except $k = 0$, whereupon it assumes a value of unity. Thus, the sum collapses to a single term, and $S_\lambda(0,T) = S_N(0)$: the delta function in the point process spectrum carries forward unchanged into the rate spectrum. For $0 < |f| < 1/T$, we have $S_N(0) = \mu$, as specified in Eq. (4.9c). Equation (3.67) then becomes

$$
\begin{aligned}
S_\lambda(f,T) &= \sum_{k=-\infty}^{\infty} S_N(f + k/T)\frac{\sin^2(\pi f T)}{(\pi f T + \pi k)^2} \\
&= \sum_{k=-\infty}^{\infty} \mu\,\frac{\sin^2(\pi f T)}{(\pi f T + \pi k)^2} \\
&= \mu \qquad \text{(B.70)}
\end{aligned}
$$

(see Gradshteyn & Ryzhik, 1994, Eq. 1.422.4). The periodicity of $S_\lambda(f,T)$ means that delta functions appear at frequencies $f = k/T$ for any integer k; the rate and point process spectra do not agree at these frequencies (hence the frequency limit in the problem specification). However, they do coincide for all other frequencies.

Prob. 4.8.2 From the solution of Prob. 4.7.3, we have

$$
S_N(f) = (2\tau_0)^{-2}\delta(f) + (2\tau_0)^{-1} - \frac{(4\tau_0)^{-1}}{1 + (\pi f \tau_0)^2}\,. \qquad \text{(B.71)}
$$

The first two terms are identical to those for the case of the homogeneous Poisson process, and we know from the solution of Prob. 4.8.1 that the results for the two spectra coincide. Since Eq. (3.67) describes a linear relation, we can use these results for the problem at hand. This leads to

$$
\begin{aligned}
&S_\lambda(f,T) \\
&\quad = \sum_{k=-\infty}^{\infty} S_N(f + k/T)\frac{\sin^2(\pi f T)}{(\pi f T + \pi k)^2}
\end{aligned}
$$

$$
\begin{aligned}
&= (2\tau_0)^{-2}\delta(f) + (2\tau_0)^{-1} - \sum_{k=-\infty}^{\infty} \frac{(4\tau_0)^{-1}}{1 + (\pi f\tau_0 + \pi k\tau_0/T)^2} \frac{\sin^2(\pi fT)}{(\pi fT + \pi k)^2} \\
&= (2\tau_0)^{-2}\delta(f) + (2\tau_0)^{-1} \\
&\quad - (4\tau_0)^{-1} + (4\tau_0)^{-1} \frac{(\tau_0/T)\coth(T/\tau_0)}{\coth^2(T/\tau_0) + \cot^2(\pi fT)} \\
&= (2\tau_0)^{-2}\delta(f) + (4\tau_0)^{-1} + \frac{(4T)^{-1}\coth(T/\tau_0)}{\coth^2(T/\tau_0) + \cot^2(\pi fT)}\,, \qquad \text{(B.72)}
\end{aligned}
$$

where we used symbolic math software to obtain the line before Eq. (B.72). Alternatively, one could substitute Eq. (B.67) into Eq. (3.54), and that result, in turn, into Eq. (3.47), but this approach requires far more algebra.

Prob. 4.8.3 To establish agreement, we take the limit $T \to 0$ in Eq. (B.72):

$$
\begin{aligned}
&\lim_{T\to 0} S_\lambda(f,T) \\
&\quad = (2\tau_0)^{-2}\delta(f) + (4\tau_0)^{-1} + \lim_{T\to 0} \frac{(4T)^{-1}\coth(T/\tau_0)}{\coth^2(T/\tau_0) + \cot^2(\pi fT)} \\
&\quad = (2\tau_0)^{-2}\delta(f) + (4\tau_0)^{-1} + \frac{(4T)^{-1}(T/\tau_0)^{-1}}{(T/\tau_0)^{-2} + (\pi fT)^{-2}} \\
&\quad = (2\tau_0)^{-2}\delta(f) + (4\tau_0)^{-1} + (4\tau_0)^{-1}\frac{(\pi f\tau_0)^2}{1 + (\pi f\tau_0)^2} \\
&\quad = (2\tau_0)^{-2}\delta(f) + (2\tau_0)^{-1}\left[1 - \frac{1/2}{1 + (\pi f\tau_0)^2}\right], \qquad \text{(B.73)}
\end{aligned}
$$

which accords with $S_N(f)$ in Eq. (B.66).

Prob. 4.9.1 We begin by reiterating Eq. (4.38), which is valid when the rate process $\mu(t)$ varies slowly over the time scale of a single event,

$$
\begin{aligned}
\mathrm{E}[\tau^n] &= \mathrm{E}[\mu^{1-n}]/\mathrm{E}[\mu] \\
\mathrm{E}[\tau] &= 1/\mathrm{E}[\mu] \\
\mathrm{E}[\tau^2] &= \mathrm{E}[\mu^{-1}]/\mathrm{E}[\mu] \\
\mathrm{Var}[\tau] &= \mathrm{E}[\tau^2] - \mathrm{E}^2[\tau] \\
&= \mathrm{E}[\mu^{-1}]/\mathrm{E}[\mu] - 1/\mathrm{E}^2[\mu] \\
&= \frac{\mathrm{E}[\mu]\,\mathrm{E}[\mu^{-1}] - 1}{\mathrm{E}^2[\mu]} \\
\frac{\mathrm{Var}[\tau]}{\mathrm{E}^2[\tau]} &= \mathrm{E}[\mu]\,\mathrm{E}[\mu^{-1}] - 1
\end{aligned}
$$

$$C_\tau \;=\; \sqrt{\mathrm{E}[\mu]\,\mathrm{E}[\mu^{-1}]-1}\,. \tag{B.74}$$

Prob. 4.9.2 For a gamma-distributed rate, the associated probability density function takes the form of Eq. (4.45),

$$p_\mu(x) = \begin{cases} [\Gamma(\mathsf{m})]^{-1}\,\mu_0^{-\mathsf{m}}\,x^{\mathsf{m}-1}\,\exp(-x/\mu_0) & x>0 \\ 0 & x\le 0, \end{cases} \tag{B.75}$$

with its associated moments

$$\begin{aligned} \mathrm{E}[\mu^n] &\equiv \int_{-\infty}^{\infty} x^n p_\mu(x)\,dx \\ &= \int_0^{\infty} x^n [\Gamma(\mathsf{m})]^{-1}\mu_0^{-\mathsf{m}} x^{\mathsf{m}-1}\exp(-x/\mu_0)\,dx \\ &= [\Gamma(\mathsf{m})]^{-1}\mu_0^{-\mathsf{m}}\int_0^{\infty} x^{n+\mathsf{m}-1}\exp(-x/\mu_0)\,dx \\ &= [\Gamma(\mathsf{m})]^{-1}\mu_0^{-\mathsf{m}}\mu_0^{n+\mathsf{m}}\int_0^{\infty} y^{n+\mathsf{m}-1}\exp(-y)\,dy \\ &= [\Gamma(\mathsf{m})]^{-1}\mu_0^{n}\,\Gamma(n+\mathsf{m}) \\ \mathrm{E}[\mu] &= \mathsf{m}\mu_0 \qquad\qquad (\mathrm{B.76}) \\ \mathrm{E}[\mu^{-1}] &= \mu_0^{-1}/(\mathsf{m}-1). \qquad\qquad (\mathrm{B.77}) \end{aligned}$$

Substituting Eqs. (B.76) and (B.77) into Eq. (B.74) yields

$$\begin{aligned} C_\tau &= \sqrt{\mathrm{E}[\mu]\,\mathrm{E}[\mu^{-1}]-1} \\ &= \sqrt{\mathsf{m}\,\mu_0\,\mu_0^{-1}/(\mathsf{m}-1)-1} \\ &= \sqrt{\mathsf{m}/(\mathsf{m}-1)-(\mathsf{m}-1)/(\mathsf{m}-1)} \\ &= 1/\sqrt{\mathsf{m}-1}\,. \end{aligned} \tag{B.78}$$

Prob. 4.9.3 We require $\mathsf{m}>1$ so that the integral defining $\mathrm{E}[\mu^{-1}]$ converges, thereby making Eqs. (B.77) and (B.78) meaningful.

Prob. 4.10.1 For the mean rate we have

$$\begin{aligned} \mathrm{E}[\mu(t)] &= \mathrm{E}\Big\{\mu_0\big[1+\cos(\omega_0 t+\theta)\big]\Big\} \\ &= \mu_0 + \mu_0\,\mathrm{E}\big[\cos(\omega_0 t+\theta)\big] \\ &= \mu_0 + \mu_0\int_0^{2\pi}(2\pi)^{-1}\,\cos(\omega_0 t+\theta)\,d\theta \\ &= \mu_0. \end{aligned} \tag{B.79}$$

For the autocorrelation of the rate we first set forth the trigonometric identity

$$\begin{aligned}
&\frac{\cos(x+y)+\cos(x-y)}{2} \\
&\quad = \tfrac{1}{2}\big[\cos(x)\,\cos(y)-\sin(x)\,\sin(y)+\cos(x)\,\cos(y)+\sin(x)\,\sin(y)\big] \\
&\quad = \cos(x)\,\cos(y). \qquad \text{(B.80)}
\end{aligned}$$

We then proceed as follows:

$$\begin{aligned}
\mathrm{E}[\mu(s)\,\mu(t)] &= \mathrm{E}\Big\{\mu_0\big[1+\cos(\omega_0 s+\theta)\big]\,\mu_0\big[1+\cos(\omega_0 t+\theta)\big]\Big\} \\
&= \mu_0^2+\mu_0^2\,\mathrm{E}\big[\cos(\omega_0 s+\theta)\big]+\mu_0^2\,\mathrm{E}\big[\cos(\omega_0 t+\theta)\big] \\
&\quad +\mu_0^2\,\mathrm{E}\big[\cos(\omega_0 s+\theta)\,\cos(\omega_0 t+\theta)\big] \\
&= \mu_0^2+0+0 \\
&\quad +\tfrac{1}{2}\mu_0^2\,\mathrm{E}\left\{\cos\big[\omega_0(s+t)+2\theta\big]+\cos\big[\omega_0(s-t)\big]\right\} \\
&= \mu_0^2+\tfrac{1}{2}\mu_0^2\left\{0+\cos\big[\omega_0(s-t)\big]\right\} \\
R_\mu(t) &= \mu_0^2+\tfrac{1}{2}\mu_0^2\cos(\omega_0\,t), \qquad \text{(B.81)}
\end{aligned}$$

where we have made use of Eq. (B.80), and noted that the expectation of any sine or cosine function with θ or 2θ in its argument becomes zero, as in Eq. (B.79).

For the coincidence rate we use Eq. (4.24) with Eq. (B.81) to obtain

$$\begin{aligned}
G(t) &= R_\mu(t)+\mathrm{E}[\mu]\,\delta(t) \\
&= \mu_0^2+\tfrac{1}{2}\mu_0^2\cos(\omega_0\,t)+\mu_0\,\delta(t). \qquad \text{(B.82)}
\end{aligned}$$

Finally, for the normalized variance we employ Eqs. (3.52), (B.79), and (B.82), to obtain

$$\begin{aligned}
F(T) &= \frac{1}{\mathrm{E}[\mu]\,T}\int_{-T}^{T}\left\{G(t)-\mathrm{E}^2[\mu]\right\}(T-|t|)\,dt \\
&= \frac{1}{\mu_0\,T}\int_{-T}^{T}\left\{\frac{\mu_0^2}{2}\,\cos(\omega_0 t)+\mu_0\,\delta(t)\right\}(T-|t|)\,dt \\
&= 1+\mu_0\,T\int_0^1\cos(\omega_0 T x)\,(1-x)\,dx \\
&= 1+\mu_0\,T\Big[(\omega_0 T)^{-1}\,\sin(\omega_0 T x)\,(1-x)-(\omega_0 T)^{-2}\,\cos(\omega_0 T x)\Big]_0^1 \\
&= 1+\mu_0\,\omega_0^{-2}\,T^{-1}\left[1-\cos(\omega_0 T)\right] \\
&= 1+2\mu_0\,\omega_0^{-2}\,T^{-1}\,\sin^2(\omega_0 T/2). \qquad \text{(B.83)}
\end{aligned}$$

Prob. 4.10.2 With $2\pi\mu_0/\omega_0$ irrational, we sample all possible phases of the rate and can avoid troublesome cases such as $\mu_0 = n\omega_0/(2\pi)$ where interevent intervals cycle

through n different values that sum to $2\pi/\omega_0$, but the n values depend on θ. The condition $\mu_0/\omega_0 \gg 1$ also permits the use of Eqs. (4.37) and (4.38), but first we require an expression for the probability density of the rate. Restricting ourselves to $0 \le x \le 2\mu_0$, the limits of possible values of the rate, we have

$$\begin{aligned}
\Pr\{\mu < x\} &= \Pr\Big\{\mu_0\big[1+\cos(\omega_0 t+\theta)\big] < x\Big\} \\
&= \Pr\big\{\cos(\omega_0 t+\theta) < x/\mu_0 - 1\big\} \\
&= \Pr\big\{\omega_0\, t+\theta \bmod \pi > \arccos\big(x/\mu_0 - 1\big)\Big\} \\
&= \Pr\left\{\frac{\omega_0 t+\theta}{\pi} \bmod 1 > \frac{1}{\pi}\arccos\big(x/\mu_0 - 1\big)\right\} \\
&= 1 - \frac{1}{\pi}\arccos\big(x/\mu_0 - 1\big) \\
p_\mu(x) &= \frac{d}{dx}\Pr\{\mu < x\} \\
&= \frac{d}{dx}\left[1 - \frac{1}{\pi}\arccos\big(x/\mu_0 - 1\big)\right] \\
&= \frac{1}{\pi}\left[1-\big(x/\mu_0-1\big)^2\right]^{-1/2}\mu_0^{-1} \\
&= \pi^{-1}\big[x(2\mu_0 - x)\big]^{-1/2}, \qquad \text{(B.84)}
\end{aligned}$$

where $\bmod(\cdot)$ indicates the modulo operation. Substituting Eq. (B.84) into Eq. (4.37) yields

$$\begin{aligned}
p_\tau(t) &= \mathrm{E}[\mu]^{-1}\, t^{-3}\, p_\mu(1/t) \\
&= \mu_0^{-1}\, t^{-3}\, \pi^{-1}\left[(1/t)\,(2\mu_0 - 1/t)\right]^{-1/2} \\
&= (\pi\mu_0)^{-1}\, t^{-2}\,(2\mu_0\, t - 1)^{-1/2}. \qquad \text{(B.85)}
\end{aligned}$$

Prob. 4.10.3 An attempt to calculate the second moment of τ from Eq. (B.85) leads to

$$\begin{aligned}
\mathrm{E}[\tau^2] &= \int_{1/(2\mu_0)}^{\infty} t^2\,(\pi\mu_0)^{-1}\, t^{-2}\,(2\mu_0\, t-1)^{-1/2}\, dt \\
&= (2/\pi)\int_0^{\infty} x^{-1/2}\, dx \\
&= \infty, \qquad \text{(B.86)}
\end{aligned}$$

where we use the substitution $x \equiv t/(2\mu_0 - 1)$. Alternatively, we could employ Eqs. (4.38) and (B.84), but the numerator $\mathrm{E}[\mu^{-1}]$ would suffer from the corresponding problem of a singularity ($\mu^{-3/2}$) near the origin.

The faulty assumption lies in the rate varying an infinitesimal amount during an interevent interval. This remains true except for t near the minima of the rate, at which

times the effective rate approaches zero; here $\mu(t)/\omega_0 \gg 1$ does not hold (although $\mu_0/\omega_0 \gg 1$ still does), and the effective interevent time approaches infinity, which leads to a diverging second moment.

One way to eliminate this problem is to decrease the modulation depth a below unity ($a < 1$) by making use of the rate function

$$\mu(t) = \mu_0\big[1 + a\cos(\omega_0\, t + \theta)\big] \tag{B.87}$$

in place of Eq. (4.46). Equation (4.46) then becomes a special case of Eq. (B.87) with $a = 1$.

Prob. 4.11.1 We begin by defining

$$\begin{aligned} a_1 &= \mu_1\, T \\ a_2 &= \mu_2\, \tau_0 \end{aligned} \tag{B.88}$$

to simplify the notation. We note that the number of events in each secondary counting process $N_{2,k}(\tau_0)$ has a mean equal to the rate μ_2 times its duration τ_0, or a_2. Equation (4.41) then simply yields the mean number of events in $dN_3(t)$ as

$$\begin{aligned} \mathrm{E}[N_3(T)] &= \mu_3\, T \\ &= \mathrm{E}[\mu_1]\,\mathrm{E}[M_k]\, T \\ &= \mu_1\, a_2\, T \\ &= a_1\, a_2. \end{aligned} \tag{B.89}$$

Since we have $T/\tau_0 \gg 1$ and $\mu_1\tau_0 \ll 1$, we can assume that the events counted in an interval T will include full clusters of events, and effectively none of the secondary processes will span the edges of the counting window T. The secondary processes form identical segments of homogeneous Poisson point processes with identical rates for identical times. Therefore, the numbers of events in the secondary counting processes $N_{2,k}(\tau_0)$ follow a Poisson counting distribution with mean value a_2. Similarly, the numbers of events in the primary point process $dN_1(t)$ also follow a Poisson counting distribution, but with mean value a_1.

We now proceed to calculate the variance, beginning by conditioning on the number of events in the primary process

$$\begin{aligned} &\mathrm{Var}\big[N_3(T) \,\big|\, N_1(T) = n\big] \\ &\quad = n^2\,\mathrm{Var}\big[N_{2,k}(\tau_0)\big] \\ &\quad = n^2\, a_2 \\ &\mathrm{Var}\big[N_3(T)\big] \\ &\quad = \sum_{n=0}^{\infty} \mathrm{Var}\big[N_3(T) \,\big|\, N_1(T) = n\big]\ \Pr\{N_1(T) = n\} \\ &\quad = \sum_{n=0}^{\infty} n^2\, a_2\ \exp(-a_1)\, a_1^n/n! \end{aligned}$$

$$
\begin{aligned}
&= a_2 \exp(-a_1) \sum_{n=1}^{\infty} n\, a_1^n/(n-1)! \\
&= a_2 \exp(-a_1) \sum_{m=0}^{\infty} (m+1)\, a_1^{m+1}/\, m! \\
&= a_2 \exp(-a_1)\, a_1 \big[\exp(a_1) + a_1 \exp(a_1)\big] \\
&= a_1\, a_2 (1 + a_1) \\
&= \mu_1\, \mu_2\, \tau_0\, T(1 + \mu_1 T). \qquad \text{(B.90)}
\end{aligned}
$$

Finally, we obtain the normalized variance as the ratio of Eqs. (B.90) and (B.89):

$$
F(T) = \frac{\mu_1\, \mu_2\, \tau_0\, T(1 + \mu_1\, T)}{\mu_1\, \mu_2\, \tau_0\, T} = 1 + \mu_1 T. \qquad \text{(B.91)}
$$

This point process thus has a normalized variance that increases linearly with the counting time, unlike the Poisson process for which the normalized variance assumes a constant value of unity. The associated counting distribution, known as the Neyman Type-A distribution (Neyman, 1939), is discussed in Sec. 10.2.1.

Prob. 4.11.2 When the rate is zero, the primary process generates no events; with no primary events, no secondary events occur either. Therefore, transmitting a "zero" and receiving a "one" cannot occur.

To determine the probability of transmitting a "one" and receiving a "zero," we first condition on the number of events generated by the primary point process $dN_1(t)$. For each event in $dN_1(T)$, the probability of generating zero events in the associated counting process $N_{2,k}(\tau_0)$ simply becomes e^{-a_2} from the definition of the Poisson counting distribution [see Eq. (4.7)]. With $N_1(T) = n$, for $N_3(T) = 0$ we require that all n events fail to generate secondary events; employing the mutual independence of the secondary point process $dN_{2,k}(t)$ yields a probability $[e^{-a_2}]^n = e^{-na_2}$. The unconditional probability is obtained by summing over the possible conditions for $N_1(T)$:

$$
\begin{aligned}
&\Pr\{N_3(T) = 0 \,\big|\, \mu_1(t) = \mu_1\} \\
&\quad = \sum_{n=0}^{\infty} \Pr\{N_3(T) = 0 \,\big|\, N_1(T) = n\} \Pr\{N_1(T) = n\} \\
&\quad = \sum_{n=0}^{\infty} e^{-n\, a_2}\, e^{-a_1}\, a_1^n/n! \\
&\quad = \exp(-a_1) \sum_{n=0}^{\infty} \left(e^{-a_2}\, a_1\right)^n/n! \\
&\quad = \exp(-a_1) \exp\left(e^{-a_2}\, a_1\right) \\
&\quad = \exp\left[-a_1 \left(1 - e^{-a_2}\right)\right]. \qquad \text{(B.92)}
\end{aligned}
$$

B.5 FRACTAL AND FRACTAL-RATE POINT PROCESSES

Prob. 5.1.1 Using a straight edge on the descending low-frequency portions of the COMPUTER and GENICULATE data presented in Fig. 5.1, we find that $\widehat{\alpha}_S \approx 0.8$ for the COMPUTER curve and $\widehat{\alpha}_S \approx 2.0$ for the GENICULATE curve. Using the same straight edge on the ascending large-counting-time portions of the COMPUTER and GENICULATE data presented in Fig. 5.2, we find that $\widehat{\alpha}_A \approx 0.7$ for the COMPUTER curve and $\widehat{\alpha}_A \approx 1.9$ for the GENICULATE curve. Thus, $\widehat{\alpha}_A + (-\widehat{\alpha}_S) \approx 0$ for both sets of data. The two exponents do not sum precisely to zero because both estimators exhibit variance, as discussed in Chapter 12.

Prob. 5.1.2 The normalized-variance scaling exponent $\widehat{\alpha}_F \approx 0.8$ for the COMPUTER data accords well with the normalized Haar-wavelet variance result $\widehat{\alpha}_A \approx 0.7$ as well as with the spectral result $\widehat{\alpha}_S \approx 0.8$. For the GENICULATE data, on the other hand, $\widehat{\alpha}_F \approx 1.0$; this lies significantly below the spectral and wavelet values $\widehat{\alpha}_S \approx 2.0$ and $\widehat{\alpha}_A \approx 1.9$, respectively, which are computed using the same data. The normalized-variance scaling exponent cannot exceed unity, in accordance with the restriction provided in Eq. (5.27). This example signals that one must use caution when making use of the normalized variance.

Another example in which the scaling exponent provided by the normalized variance can be misleading arises when nonstationarity is present. Careful analysis reveals that nonstationarity in a nonfractal point process can masquerade as fractal behavior with $\widehat{\alpha}_F = 1.0$, as shown in Eq. (5.33). A demonstration of this is provided by the spike train recorded at the lateral superior olivary complex in the mammalian auditory system (Teich et al., 1990).

Prob. 5.2.1 Using a straight edge to measure the slopes of the curves in Figs. 5.1 and 5.7, we find that $\widehat{\alpha}_S$ and $\widehat{\alpha}_{S\tau}$ lie below unity for four sets of data: CORTEX, COMPUTER, COCHLEA, and RETINA; and lie above unity for the remainder.

Prob. 5.2.2 (i) Because of the decreasing power-law dependence of the rate spectrum, it appears that all seven data sets can be represented by fractal-based point processes. However, one measure alone is seldom sufficient to reach such a conclusion. (ii) In accordance with the criteria set forth in Sec. 5.5.1, data sets that exhibit $\widehat{\alpha}_S > 1$ cannot be fractal point processes. Thus, use of the point-process spectrum alone leaves four point processes as possible fractal point processes: CORTEX, COMPUTER, COCHLEA, and RETINA. (iii) Based only on the data presented in Fig. 5.1, these four processes could represent fractal renewal processes. (iv) According to the characteristics specified in Sec. 5.5.2, all seven point processes are possibly fractal-rate point processes.

Prob. 5.2.3 (i) Again, because of the decreasing power-law dependence of the rate spectrum, it appears that all seven data sets represent fractal-based point processes. However, this conclusion is strengthened substantially for all data sets because two different fractal measures exhibit the power-law dependence. (ii) The fractal expo-

nents extracted from the interval spectrum are quite similar to those obtained from the point-process spectrum. This confirms that the same four point processes specified above could be fractal point processes: CORTEX, COMPUTER, COCHLEA, and RETINA. (iii) However, the power-law behavior in the interval spectrum tells us that these four fractal-based point processes *cannot* be fractal renewal processes. As discussed in Sec. 5.5.4, the interval spectrum of a fractal renewal process resembles that of a nonfractal renewal process, such as the homogeneous Poisson, which does not have power-law behavior. (iv) All seven point processes remain candidate fractal-rate point processes. In fact, since fractal point processes other than the fractal renewal process are encountered only infrequently, it is likely that all seven point processes are indeed fractal-rate point processes. This hypothesis can be tested in other ways, such as by examining the generalized dimension (see Prob. 5.5) and by using surrogate-data techniques (see Secs. 11.4 and 11.5).

Prob. 5.2.4 The close agreement between $\widehat{\alpha}_S$ and $\widehat{\alpha}_{S\tau}$ suggests that $\widehat{S}_\tau(\mathsf{f})$ can indeed be used to provide a good estimate of the fractal exponent, at least for some fractal-based point processes (assuredly not for fractal renewal processes). The limitations of using interval-based measures as identification tools for fractal-based point processes are addressed in more detail in Sec. 12.3.1.

Prob. 5.2.5 Computation of the interval spectrum treats the data as a collection of discrete-time samples so that the maximum interval frequency $\mathsf{f} = \frac{1}{2}$ by construction.

Prob. 5.3.1 Using a straight edge to measure the slopes of the curves in Figs. 5.2 and 5.8, we find that $\widehat{\alpha}_A$ and $\widehat{\alpha}_{A\tau}$ both lie below unity for four sets of data, CORTEX, COMPUTER, COCHLEA, and RETINA, and above unity for the remainder. The result matches that obtained by examining Figs. 5.1 and 5.7 (see Prob. 5.2.1).

Prob. 5.3.2 (i) Because the normalized Haar-wavelet variance increases as a power-law function of the counting time, it seems that all seven data sets can be represented by fractal-based point processes. However, again, one measure alone is seldom sufficient to assure such a conclusion. (ii) Data sets that exhibit $\widehat{\alpha}_A > 1$ cannot be fractal point processes, according to Sec. 5.5.1. Using this measure alone again leaves only four point processes as possible fractal point processes: CORTEX, COMPUTER, COCHLEA, and RETINA. (iii) These same four processes could be fractal renewal processes. (iv) According to Sec. 5.5.2, all seven point processes could be fractal-rate point processes.

Prob. 5.3.3 (i) All seven data sets are likely representable by fractal-based point processes since two separate fractal measures indicate the presence of power-law behavior. (ii) The fractal exponents extracted from the normalized interval wavelet variance are similar to those from the normalized Haar-wavelet variance. This confirms that the same four point processes with $\widehat{\alpha} < 1$ could be fractal point processes. (iii) However, the presence of power-law behavior in the normalized interval wavelet variance indicates that the four possible fractal point processes indicated above cannot be fractal renewal processes. Like all interval-based measures, the normalized

interval wavelet variance for a fractal renewal process resembles that for a nonfractal renewal process, which is devoid of power-law behavior. (iv) All seven point processes still remain candidates as fractal-rate point processes. Together with the information provided by the point-process and interval spectra (see Prob. 5.2), this is very likely the case.

Prob. 5.3.4 The reasonable agreement between the values of $\widehat{\alpha}_A$ and $\widehat{\alpha}_{A\tau}$ again suggests that $\widehat{A}_\tau(k)$ can be used to provide a good estimate of the fractal exponent, subject to the various limitations discussed in Sec. 12.3.1.

Prob. 5.3.5 As with the interval spectrum (see Prob. 5.2.5), the data are taken as discrete-time samples so that the minimum value of k is 2 by construction.

Prob. 5.4.1 The interevent-interval histogram, in isolation, reveals little about the nature of the underlying point process. In particular, it cannot be used to determine whether a point process represents a fractal-based point process, a fractal point process, a fractal renewal process, a fractal-rate point process, or indeed a nonfractal point process in many cases. However, it does allow elimination of the options of fractal point process and fractal renewal process if the histogram fails to exhibit a power-law region. However, the converse is not true: the presence of power-law behavior in the interevent-interval histogram does *not* definitively indicate that the point process is a fractal renewal process. This is because the ordering of the intervals can conspire to create a power-law interevent-interval histogram even though the intervals are not independent and identically distributed. Indeed, we will examine just such an example in Probs. 7.8 and 11.12.

Examining all of the histograms in Fig. 5.9 reveals that only three of the point processes exhibit what could be even remotely considered a region of power-law behavior: SYNAPSE, CORTEX, and COMPUTER. Each of these histograms displays approximately straight-line behavior over a range of interevent intervals whose ratio is about 30. While this is not sufficient to provide a convincing argument for the presence of power-law behavior, the other four point processes exhibit far less, if any at all. Of all the point processes, therefore, only these three can conceivably belong to the class of fractal renewal processes.

Prob. 5.4.2 The solution to Prob. 5.2 tells us that $\widehat{\alpha}_S$ and $\widehat{\alpha}_{S\tau}$ lie below unity for four sets of data: CORTEX, COMPUTER, COCHLEA, and RETINA. The use of the rate and interval spectra thus leave these four point processes as possible fractal point processes. However, as explained in the solution to Prob. 5.2, the presence of power-law behavior in the interval spectrum for all of these data sets indicates that these four processes *cannot* be fractal renewal point processes. These conclusions are confirmed by the results for the normalized Haar-wavelet variance and normalized interval wavelet variance, as reported in Prob. 5.3.

Combining this information, we conclude that all seven data sets very likely represent fractal-based point processes. None can be a fractal renewal process but four (CORTEX, COMPUTER, COCHLEA, and RETINA) can conceivably be fractal point

processes other than fractal renewal processes. The generalized dimension D_q provides a more definitive test (see Prob. 5.5).

Prob. 5.5.1 Since we normalize by the estimated mean interval, we can use any theoretical mean values to simulate the data sets. We choose unity for convenience. Figure B.3 presents the results of these simulations. For the fractal renewal process,

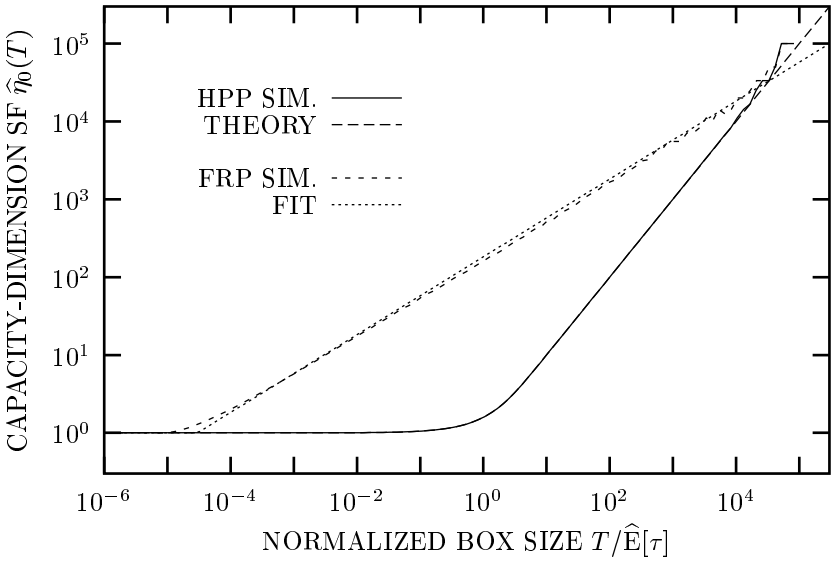

Fig. B.3 Capacity-dimension scaling functions (SF) $\widehat{\eta}_0(T)$, based on Eq. (3.74), for two simulated point processes: a homogeneous Poisson process (solid curve) and a fractal renewal process (short-dash curve). We also include the theoretical result for the former process (long-dash curve), discussed in Prob. 4.3, and a power-law fit given by $\sqrt{T/T_0}$, with $T_0 \equiv 3 \times 10^{-5}$ for this particular simulation (dotted curve).

the capacity-dimension scaling function provided in Eq. (3.74) increases as $T^\gamma = \sqrt{T}$ over a broad range of counting times T, yielding $\widehat{D}_0 = \frac{1}{2}$ and identifying the data as a fractal point process rather than a fractal-rate point process. The homogeneous Poisson process, in contrast, yields a scaling function that varies only as integer powers of the counting time: zero for $T \ll \widehat{\mathrm{E}}[\tau]$, and unity for $T \gg \widehat{\mathrm{E}}[\tau]$.

Prob. 5.5.2 All of the experimental curves displayed in Fig. 5.10 bear a strong similarity to those associated with the homogeneous Poisson process shown in Fig. B.3, exhibiting slopes (power-law exponents) of zero for short times and unity for longer times. None of these data sets has a fractional value of $\widehat{D}_0$. As expected for any data set, some variability exists for larger values of $T/\widehat{\mathrm{E}}[\tau]$, where the sum extends over relatively few boxes. The principal distinction among the curves in Fig. 5.10 occurs near $T = \widehat{\mathrm{E}}[\tau]$, where the sharpness of the transition region varies. The HEARTBEAT

data set displays the sharpest transition (sharper even than the homogeneous Poisson process) whereas the SYNAPSE data set exhibits the most gradual transition.

The variation in sharpness of the curves near $T = \widehat{\mathrm{E}}[\tau]$ stems from the local variability inherent in the corresponding point processes. For a perfectly periodic point process ($\mathrm{Var}[\tau] = 0$) and $T \geq \tau$, the point-process events will be distributed as evenly as possible among the counting windows. This gives rise to the minimum number of windows that are devoid of events [$Z_k(T) = 0$], which maximizes the sum in Eq. (3.74) and thereby minimizes $\eta_0(T)$. The HEARTBEAT data most closely follow such a periodic form, and therefore exhibit the lowest value of $\widehat{\eta}_0(\widehat{\mathrm{E}}[\tau])$. The largest value of $\widehat{\eta}_0(\widehat{\mathrm{E}}[\tau])$ obtains for the SYNAPSE data, which exhibits significant variability, departing most strongly from a periodic form. A number of measures can be used to index point-process variability as it affects $\widehat{\eta}_0(T)$. The count-based coefficient of variation evaluated at $T = \widehat{\mathrm{E}}[\tau]$ turns out to accurately predict the behavior. Although not quite as reliable, the interval-based coefficient of variation C_τ [Eq. (3.5)] also provides a useful guide near $T = \widehat{\mathrm{E}}[\tau]$. Visual inspection of Fig. 5.9 confirms that the SYNAPSE and HEARTBEAT data have large and small values of $\widehat{C}_\tau$, respectively. The interval-based serial correlation coefficient [Eq. (3.17)] has little relevance to $\widehat{\eta}_0(\widehat{\mathrm{E}}[\tau])$ for the data sets examined. We confirmed this by randomly shuffling the intervals (see Sec. 11.5) of the SYNAPSE data and recomputing $\widehat{\eta}_0(T)$; the results nearly coincided with those of the original data.

Prob. 5.5.3 Except for transition regions of various widths, and variability associated with small numbers of boxes, the curves lie parallel to each other so that $\widehat{D}_q$ has essentially the same value, whatever the value of q. All curves exhibit power-law exponents of zero for short times, and unity for longer times, just as for the homogeneous Poisson process, a nonfractal object (see Prob. 4.3 and Fig. B.3). We conclude that neither a fractal point process nor a multifractal point process provides a good description for these data. A fractal-rate point process, rather, describes these data.

To determine why the curves for different values of q are parallel, rather than coincident, we examine the transition times $\widehat{T}_{Dq}$ at which the slopes change. Although $\widehat{T}_{Dq}$ lies within an order of magnitude of $\widehat{\mathrm{E}}[\tau]$ for the SYNAPSE data displayed in Fig. 5.11, it clearly decreases as q increases: it diminishes by a factor of about 7 between $q = -1$ (solid curve) and $q = 2$ (dash-dot curve). On the other hand, for the INTERNEURON data displayed in Fig. 11.18, as well as for a simulated homogeneous Poisson process (not shown), $\widehat{T}_{Dq}$ essentially coincides with $\widehat{\mathrm{E}}[\tau]$, regardless of q.

As part of a diagnostic process to determine the role played by interevent-interval ordering with respect to the dependence of $\widehat{T}_{Dq}$ on q, we shuffle the SYNAPSE data (see Sec. 11.5) before computing the generalized-dimension scaling functions $\widehat{\eta}_q(T)$. The values of $\widehat{T}_{Dq}$ then turn out *not* to depend on q, and the behavior of the shuffled SYNAPSE data is similar to that of the (unshuffled) INTERNEURON and simulated-Poisson-process data. This indicates that interval ordering plays an important role in determining the dependence of $\widehat{T}_{Dq}$ on q. In contrast, interval ordering plays essentially no role in determining the sharpness of the transition in $\widehat{\eta}_0(T)$ near $T = \widehat{\mathrm{E}}[\tau]$, as discussed in Prob. 5.5.2.

Calculation of the interval serial correlation coefficient [Eq. (3.17)] proves useful in elucidating this role. As mentioned above, this measure does not prove useful for explaining the sharpness of the transition in $\widehat{\eta}_0(T)$ near $T = \widehat{\mathrm{E}}[\tau]$. The outcome is $\widehat{\varrho}_\tau(1) \approx 0.3$ for the SYNAPSE data, while it is far smaller for the INTERNEURON data [$\widehat{\varrho}_\tau(1) \approx 0.08$] and for the simulated homogeneous Poisson process with the same number of intervals (2644) as the SYNAPSE data [$\widehat{\varrho}_\tau(1) \approx 1/\sqrt{2644}$]. The decrease of $\widehat{T}_{Dq}$ with increasing q appears to be linked to the presence of correlated intervals; it also depends on the presence of heavy tails.

To confirm this connection, we generated a correlated random sequence from a homogeneous Poisson process, with unity mean rate and 2644 intervals, by adding $0.01k$ to the kth interval. If $\{\tau_k\}$ is the sequence of independent, identically distributed intervals comprising the initial process, the modified process then has the sequence $\{\tau_k + 0.01k\}$. The modified process has a large positive interval serial correlation coefficient (0.98), although it does not have nearly the range of values that the SYNAPSE data does (the modified-Poisson process has skewness and kurtosis near zero, whereas for the SYNAPSE data these values are 6 and 69, respectively). Nevertheless, the progression of $\widehat{T}_{Dq}$ with q for the correlated random sequence and for the SYNAPSE data are similar.

What is the underlying origin of this progression? As q increases, the quantity $\eta_q(T) = [\sum_k Z_k^q(T)/N(L)]^{1/(q-1)}$ depends more and more strongly on the largest value of $Z_k(T)$ over k, which $\eta_q(T)$ approaches for very large values of q. Similarly, for large-magnitude negative q, the smallest value of $Z_k(T)$ dominates $\eta_q(T)$. We now compare the expected results for a clustered point process on the one hand, with those for a nonclustered point process (such as the homogeneous Poisson process) on the other hand: the clustered process will have a greater number of larger and smaller values of $Z_k(T)$ than will the nonclustered process. For large q, this will result in a larger effective value of $\widehat{\eta}_q(T)$, whereas for large-magnitude negative q, it will result in a smaller effective value of $\eta_q(T)$. We conclude that for clustered point processes, the curves for large positive q will be shifted to the left, while those for large-magnitude negative q will be shifted to the right. This is precisely the behavior observed in the SYNAPSE data displayed in Fig. 5.11. The effect is more pronounced for intervals with heavy tails since the clustering effect is then that much stronger.

Prob. 5.6 The difference between these two expressions for $R_Z(k,T)$ lies in the evaluation of the integral. We have

$$\begin{aligned}
&\int_{k-1}^{k+1} x^{\alpha-1}\big(1-|x-k|\big)\,dx \\
&\quad= \int_{k-1}^{k} x^{\alpha-1}\big[1-(k-x)\big]\,dx + \int_{k}^{k+1} x^{\alpha-1}\big[1-(x-k)\big]\,dx \\
&\quad= \int_{k-1}^{k} \big[(1-k)\,x^{\alpha-1} + x^{\alpha}\big]\,dx + \int_{k}^{k+1} \big[(1+k)\,x^{\alpha-1} - x^{\alpha}\big]\,dx \\
&\quad= (1-k)\frac{k^\alpha-(k-1)^\alpha}{\alpha} + \frac{k^{\alpha+1}-(k-1)^{\alpha+1}}{\alpha+1}
\end{aligned}$$

$$
\begin{aligned}
& + (1+k)\frac{(k+1)^\alpha - k^\alpha}{\alpha} - \frac{(k+1)^{\alpha+1} - k^{\alpha+1}}{\alpha+1} \\
= \; & \frac{(\alpha+1)\,k^\alpha - (\alpha+1)\,k^{\alpha+1} + (\alpha+1)\,(k-1)^{\alpha+1} + \alpha\,k^{\alpha+1}}{\alpha\,(\alpha+1)} \\
& + \frac{-\alpha\,(k-1)^{\alpha+1} + (\alpha+1)\,(k+1)^{\alpha+1} - (\alpha+1)\,k^\alpha}{\alpha\,(\alpha+1)} \\
& + \frac{-(\alpha+1)\,k^{\alpha+1} - \alpha\,(k+1)^{\alpha+1} + \alpha\,k^{\alpha+1}}{\alpha\,(\alpha+1)} \\
= \; & \frac{(k-1)^{\alpha+1} - 2k^{\alpha+1} + (k+1)^{\alpha+1}}{\alpha\,(\alpha+1)}, \qquad \text{(B.93)}
\end{aligned}
$$

in accordance with Eq. (5.13).

Prob. 5.7 The expressions in the domains $\alpha < 1$ and $\alpha > 1$ differ only in the signs of two of the factors. These changes ensure that each factor is positive. Since the two sign changes cancel for the product, this leaves the result unchanged. For simplicity, we chose the form for $\alpha < 1$ for comparison with that for $\alpha = 1$:

$$
\begin{aligned}
\lim_{\alpha\to 1} \frac{\cos(\pi\alpha/2)\,\Gamma(\alpha+2)}{(2-2^\alpha)} &= \Gamma(1+2)\lim_{\alpha\to 1}\frac{\cos(\pi\alpha/2)}{(2-2^\alpha)} \\
&= 2\lim_{\alpha\to 1}\frac{-(\pi/2)\sin(\pi\alpha/2)}{-2^\alpha\ln(2)} \\
&= 2\frac{(\pi/2)\sin(\pi/2)}{2\ln(2)} \\
&= \frac{\pi}{2\ln(2)}, \qquad \text{(B.94)}
\end{aligned}
$$

as promised, where we have made use of l'Hôpital's rule.

Prob. 5.8 Equation (3.61) yields the normalized variance given the spectrum

$$
\begin{aligned}
F(T) &= \frac{2}{\pi^2\,\mathrm{E}[\mu]\,T}\int_{0+}^{\infty} S_N(f)\,\sin^2(\pi f T)\,f^{-2}\,df \\
&= 1 + \frac{2}{\pi^2\,\mathrm{E}[\mu]\,T}\int_{1/B}^{\infty} \mathrm{E}[\mu]\,(f_S/f)\,\sin^2(\pi f T)\,f^{-2}\,df \\
&= 1 + \frac{2f_S}{\pi^2\,T}\int_{1/B}^{\infty} \sin^2(\pi f T)\,f^{-3}\,df \\
&= 1 + \frac{2f_S}{\pi^2 T}\,(\pi T)^2\int_{\pi T/B}^{\infty} \sin^2(x)\,x^{-3}\,dx. \qquad \text{(B.95)}
\end{aligned}
$$

Now consider the limit

$$
\lim_{\epsilon\to 0}\frac{\displaystyle\int_\epsilon^\infty \sin^2(x)\,x^{-3}\,dx}{\ln(1/\epsilon)} = \lim_{\epsilon\to 0}\frac{-\sin^2(\epsilon)\,\epsilon^{-3}}{-1/\epsilon}
$$

$$\begin{aligned} &= \lim_{\epsilon \to 0} \left[\frac{\sin(\epsilon)}{\epsilon} \right]^2 \\ &= 1. \end{aligned} \tag{B.96}$$

Combining Eqs. (B.95) and (B.96), we obtain the approximation

$$\begin{aligned} F(T) &\approx 1 + \frac{2f_S}{\pi^2 T} (\pi T)^2 \ln(B/\pi T) \\ &= 1 + 2f_S T \ln(B/\pi T) \\ &\approx 1 + 2f_S T \ln(B/T), \end{aligned} \tag{B.97}$$

where the last step in Eq. (B.97) obtains because in the limit $B/T \gg 1$, the term $\ln(B/T)$ dominates $\ln(\pi)$.

Substituting Eq. (B.97) into Eq. (3.41) yields the normalized Haar-wavelet variance

$$\begin{aligned} A(T) &= 2F(T) - F(2T) \\ &= 2 + 4f_S T \ln(B/T) - 1 - 4f_S T \ln(B/2T) \\ &= 1 + 4f_S T \big[\ln(B/T) - \ln(B/2T)\big] \\ &= 1 + 4f_S T \ln[(B/T)\,(2T/B)] \\ &= 1 + 4\ln(2) f_S T, \end{aligned} \tag{B.98}$$

linear in T as we expect for $A(T)$ with $\alpha = 1$. Interestingly, retaining the factor of π within the logarithm in Eq. (B.97) leaves the result of Eq. (B.98) unchanged [see Eq. (A.37)].

Proceeding to the normalized coincidence rate, we use Eq. (3.55) with Eq. (B.97), yielding

$$\begin{aligned} G(t) &= \mathrm{E}^2[\mu] + \frac{\mathrm{E}[\mu]}{2} \frac{d^2}{dT^2} \big[TF(T)\big]_{T=t} \\ G(t) - \mathrm{E}^2[\mu] &\approx \frac{\mathrm{E}[\mu]}{2} \frac{d^2}{dt^2} \big[t + 2f_S\, t^2 \ln(B/t)\big] \\ &= \mathrm{E}[\mu]\, f_S \frac{d^2}{dt^2} \big[t^2 \ln(B) - t^2 \ln(t)\big] \\ &= \mathrm{E}[\mu]\, f_S \big[2\ln(B) - 3 - 2\ln(t)\big] \\ &= \mathrm{E}[\mu]\, f_S\, 2\ln(B/e^{3/2}t) \\ &\approx 2\mathrm{E}[\mu]\, f_S \ln(B/t), \end{aligned} \tag{B.99}$$

where we ignore the factor of $e^{3/2} \doteq 4.481689$, for the same reason as in Eq. (B.97).

Finally, we substitute Eq. (B.99) into Eq. (3.54), and obtain

$$R_Z(k,T) = \int_{-T}^{T} G(kT + t)\,(T - |t|)\, dt$$

$$\begin{aligned} &\approx \int_{-T}^{T} \left\{ \mathrm{E}^2[\mu] + 2\mathrm{E}[\mu]\, f_S \ln[B/(kT+t)] \right\} (T-|t|)\, dt \\ &= \mathrm{E}^2[\mu]\, T^2 + 2\mathrm{E}[\mu]\, f_S \int_{-T}^{T} \ln[B/(kT+t)](T-|t|)\, dt. \end{aligned} \quad \text{(B.100)}$$

We assume that $k \gg 1$ as before, and that the delta function in the coincidence rate does not lie within the limits of integration in Eq. (B.100). Furthermore, since $k \gg 1$, the argument of the logarithm in Eq. (B.100) changes little over the range of integration, so that we can ignore the t term in the denominator, whereupon

$$\begin{aligned} R_Z(k,T) &\approx \mathrm{E}^2[\mu]\, T^2 + 2\mathrm{E}[\mu]\, f_S \int_{-T}^{T} \ln[B/(kT)]\, (T-|t|)\, dt \\ &= \mathrm{E}^2[\mu]\, T^2 + 2\mathrm{E}[\mu]\, f_S \ln[B/(kT)]\, T^2. \end{aligned} \quad \text{(B.101)}$$

Prob. 5.9 Calculation of the spectrum proceeds by substituting Eq. (5.50) into Eq. (3.57), which yields

$$\begin{aligned} S_N(f) &= \int_{-\infty}^{\infty} G(t)\, e^{-i2\pi ft}\, df \\ &= \mathrm{E}[\mu] + \mathrm{E}^2[\mu]\, \delta(f) + \mathrm{E}^2[\mu] \operatorname{sgn}(t_G)\, |t_G|^{1-\alpha} \\ &\quad \times \int_{-\infty}^{\infty} |t|^{\alpha-1}\, e^{-|t|/B}\, e^{-i2\pi ft}\, df. \end{aligned} \quad \text{(B.102)}$$

Rearranging Eq. (B.102) leads to

$$\begin{aligned} &S_N(f) - \mathrm{E}^2[\mu]\, \delta(f) \\ &= \mathrm{E}[\mu] + \operatorname{sgn}(t_G)\, \mathrm{E}^2[\mu]\, |t_G|^{1-\alpha} \int_0^{\infty} t^{\alpha-1}\, e^{-t/B} \left[e^{i2\pi ft} + e^{-i2\pi ft} \right] df \\ &= \mathrm{E}[\mu] + 2\operatorname{sgn}(t_G)\, \mathrm{E}^2[\mu]\, |t_G|^{1-\alpha}\, \mathrm{Re}\left\{ \int_0^{\infty} t^{\alpha-1}\, e^{-t/B}\, e^{i2\pi ft}\, df \right\} \\ &= \mathrm{E}[\mu] + 2\operatorname{sgn}(t_G)\, \mathrm{E}^2[\mu]\, |t_G|^{1-\alpha}\, \mathrm{Re}\left\{ (1/B + i2\pi f)^{-\alpha} \int_0^{\infty} x^{\alpha-1} e^{-x}\, dx \right\} \\ &= \mathrm{E}[\mu] + 2\operatorname{sgn}(t_G)\, \mathrm{E}^2[\mu]\, |t_G|^{1-\alpha}\, \Gamma(\alpha)\, \mathrm{Re}\left\{ (1/B + i2\pi f)^{-\alpha} \right\}. \end{aligned} \quad \text{(B.103)}$$

Focusing now on the scaling region $f \gg 1/B$, the delta function at zero frequency can be ignored since we are concerned with positive frequencies only. Equation (B.103) then becomes

$$\begin{aligned} S_N(f) &\approx \mathrm{E}[\mu] + 2\operatorname{sgn}(t_G)\Gamma(\alpha)\mathrm{E}^2[\mu]|t_G|^{1-\alpha}\mathrm{Re}\left\{(i2\pi f)^{-\alpha}\right\} \\ &= \mathrm{E}[\mu] + 2\operatorname{sgn}(t_G)\Gamma(\alpha)\mathrm{E}^2[\mu]|t_G|^{1-\alpha}(2\pi f)^{-\alpha}\mathrm{Re}\left\{(e^{i\pi/2})^{-\alpha}\right\} \\ &= \mathrm{E}[\mu] + 2\operatorname{sgn}(t_G)\Gamma(\alpha)\mathrm{E}^2[\mu]|t_G|^{1-\alpha}(2\pi f)^{-\alpha}\mathrm{Re}\left\{e^{i\alpha\pi/2}\right\} \\ &= \mathrm{E}[\mu] + 2\operatorname{sgn}(t_G)\Gamma(\alpha)\mathrm{E}^2[\mu]|t_G|^{1-\alpha}(2\pi f)^{-\alpha}\cos(\alpha\pi/2) \\ S_N(f)/\mathrm{E}[\mu] &= 1 + \underbrace{2\operatorname{sgn}(t_G)\Gamma(\alpha)\mathrm{E}[\mu]|t_G|}_{\times}\underbrace{\cos(\alpha\pi/2)}_{\times}\underbrace{(2\pi f|t_G|)^{-\alpha}}_{\cdot} \end{aligned} \quad \text{(B.104)}$$

We display the last term on the right-hand-side of Eq. (B.104) as a product of three factors (delineated by braces). The first has the same sign as t_G. Its magnitude could easily exceed unity, and would lie near unity for a process with non-negligible fractal behavior. The second factor assumes negative values for $1 < \alpha < 3$, and lies within an order of magnitude of unity for $1.06377 < \alpha < 2.93623$. The final factor can be much larger than unity, given a sufficiently large value of B. The product of these three factors, then, can easily achieve large magnitudes, certainly exceeding unity. If t_G were to have a positive value, then the spectrum would lie below unity for low frequencies, which is not possible. We conclude that t_G cannot be positive.

We now compute the normalized variance $F(T)$. This proceeds from Eq. (3.52), which leads to

$$\begin{aligned} F(T) &= \frac{1}{\mathrm{E}[\mu]T} \int_{-T}^{T} \left\{ G(t) - \mathrm{E}^2[\mu] \right\} (T - |t|)\, dt \\ &= \frac{1}{\mathrm{E}[\mu]T} \int_{-T}^{T} \Big\{ \mathrm{E}[\mu]\, \delta(t) \\ &\qquad + \mathrm{E}^2[\mu]\, \mathrm{sgn}(t_G)\, (|t/t_G|)^{\alpha-1}\, e^{-|t|/B} \Big\} (T - |t|)\, dt \\ &= 1 + 2\, \mathrm{sgn}(t_G)\, \mathrm{E}[\mu] |t_G|^{1-\alpha}\, T^{-1} \int_0^T t^{\alpha-1}\, e^{-|t|/B}\, (T - t)\, dt. \end{aligned} \tag{B.105}$$

Focusing on the range of times $0 < T \ll B$ permits us to ignore the exponential factor in Eq. (B.105), which leads to

$$\begin{aligned} F(T) &\approx 1 + 2\, \mathrm{sgn}(t_G)\, \mathrm{E}[\mu]\, |t_G|^{1-\alpha}\, T^{-1} \int_0^T t^{\alpha-1} (T - t)\, dt \\ &= 1 + 2\, \mathrm{sgn}(t_G)\, \mathrm{E}[\mu]\, |t_G|^{1-\alpha}\, T^{-1} \frac{T^{\alpha+1}}{\alpha(\alpha+1)} \\ &= 1 + \mathrm{sgn}(t_G) \frac{2\mathrm{E}[\mu]\, |t_G|^{1-\alpha}}{\alpha(\alpha+1)}\, T^{\alpha}. \end{aligned} \tag{B.106}$$

By a similar argument as that provided for the spectrum, t_G cannot have a negative sign. Since t_G can be neither negative nor positive, it must be zero, indicating that the analytical form of the coincidence rate postulated in Eq. (5.50) is not suitable. The form of the normalized variance also confirms that something is awry; it exhibits an exponent that exceeds unity, which is impermissible.

Prob. 5.10 We begin with the normalized variance. The frequency range $f \ll f_S$ corresponds to the time scale $1/T \ll f_S$ or $f_S T \gg 1$; this leads to the limit $y_n \to \infty$. For large values of y_n, the y_n^2 term inside the parentheses in Eq. (5.17) dominates the other, constant terms, which we can then ignore. Substituting directly, we obtain

$$F(T) - 1 \;\to\; \frac{\sqrt{8}}{\sqrt{\pi}\, y_n} \sqrt{\sqrt{y_n^2}}$$

$$\begin{aligned} &= \frac{\sqrt{8}}{\sqrt{\pi y_n}} \\ &= \frac{2}{\pi\sqrt{f_S}}\, T^{-1/2}, \end{aligned} \tag{B.107}$$

in accordance with Eq. (5.20). Equation (3.41) provides $A(T)$ in terms of $F(T)$, leading to

$$\begin{aligned} A(T) &= 2F(T) - F(2T) \\ A(T) - 1 &= 2\frac{2}{\pi\sqrt{f_S}}\, T^{-1/2} - \frac{2}{\pi\sqrt{f_S}}\, (2T)^{-1/2} \\ &= \frac{4}{\pi\sqrt{f_S}}\, T^{-1/2} - \frac{2/\sqrt{2}}{\pi\sqrt{f_S}}\, T^{-1/2} \\ &= \frac{4-\sqrt{2}}{\pi\sqrt{f_S}}\, T^{-1/2}, \end{aligned} \tag{B.108}$$

which is Eq. (5.21). Finally, we can determine the normalized coincidence rate from the normalized variance through Eq. (3.55), yielding Eq. (5.19):

$$\begin{aligned} G(t) &= \mathrm{E}^2[\mu] + \frac{\mathrm{E}[\mu]}{2}\frac{d^2}{dT^2}\left[TF(T)\right]_{T=t} \\ G(t) - \mathrm{E}^2[\mu] &\approx \frac{\mathrm{E}[\mu]}{2}\frac{2}{\pi\sqrt{f_S}}\frac{d^2}{dt^2}\left(t \times t^{-1/2}\right) \\ &= \frac{\mathrm{E}[\mu]}{\pi\sqrt{f_S}}\frac{d^2}{dt^2}\left(t^{1/2}\right) \\ &= \frac{\mathrm{E}[\mu]}{\pi\sqrt{f_S}}\frac{-t^{-3/2}}{4} \\ &= -\frac{\mathrm{E}[\mu]}{4\pi\sqrt{f_S}}\, t^{-3/2}, \end{aligned} \tag{B.109}$$

where we can safely ignore the delta function at zero delay because the pertinent range of times does not include this value.

Prob. 5.11 We begin by computing the normalized variance. Substituting Eq. (5.15) into Eq. (3.61) yields

$$\begin{aligned} F(T) &= \frac{2}{\pi^2\mathrm{E}[\mu]\, T}\int_{0+}^{\infty} S_N(f)\, \sin^2(\pi f T)\, f^{-2}\, df \\ &= \frac{2}{\pi^2\mathrm{E}[\mu]\, T}\int_{0}^{\infty} \mathrm{E}[\mu]\left[1 + \sqrt{f/f_S}\, \exp(-f/f_S)\right] \sin^2(\pi f T)\, f^{-2}\, df \\ &= \frac{2}{\pi}\int_{0}^{\infty} \sin^2(u)\, u^{-2}\, du + \frac{4}{\pi y_n}\int_{0}^{\infty} v^{-3/2}\, \exp(-v) \sin^2(y_n v/2)\, dv \end{aligned}$$

$$
\begin{aligned}
&= 1 + \frac{4}{\pi y_n} \int_0^\infty v^{-3/2} \exp(-v) \frac{\exp(iy_n v) + \exp(-iy_n v) - 2}{-4}\, dv \\
&= 1 - \frac{1}{\pi y_n} \int_0^\infty v^{-3/2} \Big\{ \exp\big[-(1 - iy_n)v\big] \\
&\qquad + \exp\big[-(1 + iy_n)v\big] - 2\exp(-v) \Big\}\, dv \\
&= 1 - \frac{1}{\pi y_n} \left(\sqrt{1 - iy_n} + \sqrt{1 + iy_n} - 2 \right) \\
&\qquad \times \int_0^\infty w^{-3/2} \exp(-w)\, dw \qquad \text{(B.110)} \\
&= 1 - \frac{1}{\pi y_n} \left(2\sqrt{\frac{\sqrt{1 + y_n^2} + 1}{2}} - 2 \right) \Gamma\left(-\tfrac{1}{2}\right) \\
&= 1 - \frac{1}{\pi y_n} \left(\sqrt{2}\sqrt{\sqrt{1 + y_n^2} + 1} - 2 \right) \left(-2\sqrt{\pi}\right) \\
&= 1 + \frac{\sqrt{8}}{\sqrt{\pi} y_n} \left(\sqrt{\sqrt{1 + y_n^2} + 1} - \sqrt{2} \right), \qquad \text{(B.111)}
\end{aligned}
$$

in accordance with Eq. (5.17), where we have defined $y_n \equiv 2\pi f_S T$. The evaluation of the square roots in Eq. (B.110) follows from the relation provided in Eq. (A.38). The use of a gamma function with negative argument in Eq. (B.110) is permissible because the integrals from which it derives, in the lines above, are bounded near the origin. Since $\sin(\epsilon)$ varies as ϵ near the origin, the integral varies as $v^{-3/2+2} = \sqrt{v}$ for small arguments. Equations (5.16) and (5.18) for the coincidence rate and normalized Haar-wavelet variance follow from Eq. (5.17) in a straightforward manner, via the use of Eqs. (3.55) and (3.41), respectively.

Prob. 5.12 Data with nonstationary rates generally yield rate spectra that decay as f^{-2}. Consider a candidate data set of duration L that has a large nonstationary component, such that the rate changes significantly over the course of the data set. Estimating the spectrum involves calculating a Fourier transform of the data (for example, the familiar fast Fourier transform); this forces the data segment into a periodic form. The difference between the rate at the beginning and at the end of the signal becomes a jump discontinuity in the now-periodic signal. Such a discontinuity generally imparts a f^{-2} character to the estimated spectrum, so that $\widehat{\alpha}_S = 2$, by virtue of the basic properties of the Fourier transform. To illustrate this, consider the signal $x(t) = t/L$, defined for $0 \le t < L$. Its Fourier series has the form

$$
x(t) = \frac{1}{2} - \sum_{n=1}^{\infty} \frac{\sin(2\pi n t/L)}{n\pi}, \qquad \text{(B.112)}
$$

and thus decays with (discrete) frequency as $1/n$, or $1/f$ since f corresponds to n/L. The corresponding spectrum therefore decays as f^{-2}. A similar argument applies to

any signal with a jump discontinuity[1]; the nonstationarity need not follow the simple linear form used for the illustration provided here.

Data sets with rate nonstationarities therefore generally yield spectra that decay as f^{-2}. Three caveats apply, however. First, the effect depends on the size of the nonstationarity. For a point process with robust fractal behavior but a very small nonstationary component, the former effect will dominate the f^{-2} term generated by the latter effect. Second, not all nonstationarities engender this effect. Consider a point process $dN(t)$ and a counting time T such that the sequence of counts $\{Z_k(T)\}$ is essentially independent, all counts have the same mean, and the variance increases with count number k. As a result of this independence, the count autocorrelation $R_Z(k,T)$ is constant for $k > 0$, so that the spectrum has no f^{-2} component despite the large nonstationarity. However, point processes that take the form of this somewhat artificial example seldom occur in practice. Finally, employing explicit window functions ameliorates the effects of nonstationarities. As discussed in Sec. 12.3.9, the use of a Hanning window reduces the deleterious effects of rate nonstationarities, causing a spectral artifact to decay as f^{-6} rather than as f^{-2}, at the cost of effectively losing half the data.

Further discussion of these issues appears in Secs. 12.3.9 and A.8.1.

Prob. 5.13.1 We begin by dividing the unit interval into 3^k equal segments, with $0 < k < m$, each of length $T = 3^{-k}$; of these, a proportion $p = 2^k/3^k$ contains $N = 2^m/2^k$ points each of the Cantor-set approximation.

By the binomial theorem, the resulting normalized variance becomes

$$\begin{aligned} F(T) &= N(1-p) \\ &= (2^m/2^k)(1-2^k/3^k) \\ &= 2^m(2^{-k}-3^{-k}) \\ &= 2^m(T^D - T), \end{aligned} \tag{B.113}$$

where $D \equiv \log(2)/\log(3) \doteq 0.630930$ is the fractal dimension of the classic triadic Cantor set. Choosing different starting times for the counting durations (other than the origin) serves to reduce the normalized variance somewhat, but does not qualitatively change the argument.

Employing Eq. (3.41) leads to an equation for the normalized Haar-wavelet variance,

$$\begin{aligned} A(T) &= 2F(T) - F(2T) \\ &= 2^m(2T^D - 2T - 2^D T^D - 2T) \\ &= 2^m(2-2^D)T^D. \end{aligned} \tag{B.114}$$

[1]We could theoretically specify an infinite-extent signal, equal to the data set where it exists and to a constant value otherwise. We could then calculate the Fourier transform of this signal for all frequencies, not just for integer multiples of the inverse of the data set duration. However, this infinite-extent signal still has at least one discontinuity since the constant value cannot match both the beginning and the end of the data set. As a consequence, the f^{-2} form emerges for this case as well.

This expression does indeed vary in a power-law fashion with T, in accord with the fractal nature of the Cantor set itself.

Prob. 5.13.2 To consider the spectral properties of the modified Cantor set, we take Fourier transforms of Eq. (5.52). Convolutions become multiplications, yielding

$$\mathcal{F}\left\{dN_{m+1}(t)\right\} = 2e^{-i2\pi f/3^m}\cos(2\pi f/3^m)\,\mathcal{F}\left\{dN_m(t)\right\}. \tag{B.115}$$

Since

$$\mathcal{F}\left\{dN_0(t)\right\} = \mathcal{F}\left\{\delta(t)\right\} = 1, \tag{B.116}$$

an explicit result emerges:

$$\begin{aligned}\mathcal{F}\left\{dN_m(t)\right\} &= \prod_{k=1}^{m} 2e^{-i2\pi f/3^k}\cos(2\pi f/3^k)\\ \left|\mathcal{F}\left\{dN_m(t)\right\}\right|^2 &= 2^m\prod_{k=1}^{m}\cos^2(2\pi f/3^k).\end{aligned} \tag{B.117}$$

The same results have been obtained by others via different methods (Dettmann, Frankel & Taucher, 1994).

This expression does not exhibit scaling so that the spectral density does not reveal fractal behavior in the Cantor set; in particular, Eq. (3.62) does not hold. Thus, for nonstationary collections of points, we can no longer rely on the validity of relationships that are central to the description of fractal and fractal-rate point processes.

Nevertheless, the fractal character of the Cantor set does leave its imprint on this measure. Consider Eq. (B.117) evaluated over a range of frequencies extending from 0 to some maximum frequency $f_0 \gg 1$, where we require $f_0/3^m \ll 1$ to eliminate effects of finite m. Suppose we now change the maximum frequency to $f_0/3$. The result will resemble the unscaled version (Lowen & Teich, 1995, Fig. 6), as a result of the geometric progression of cutoff frequencies in the product; the form $\left|\mathcal{F}\left\{dN_m(t)\right\}\right|^2$ appears to contain copies of itself (Zhukovsky et al., 2001). Each factor $\cos^2(2\pi f/3^k)$ in Eq. (B.117) maps to $\cos^2(2\pi f/3^{k-1})$ in the scaled version. However, the mapping is not exact, since the factor $\cos^2(2\pi f)$ has no corresponding factor at a lower frequency; thus, plots of Eq. (B.117) are not true fractal objects.

B.6 PROCESSES BASED ON FRACTIONAL BROWNIAN MOTION

Prob. 6.1 Simply substitute the left-hand side of Eq. (6.6) into Eq. (6.1), to obtain

$$\begin{aligned} \mathrm{E}[B_H(as)\,B_H(at)] &= \tfrac{1}{2}\mathrm{E}[B_H^2(1)]\,\left(|at|^{2H}+|as|^{2H}-|at-as|^{2H}\right) \\ &= |a|^{2H}\,\tfrac{1}{2}\mathrm{E}[B_H^2(1)]\,\left(|t|^{2H}+|s|^{2H}-|t-s|^{2H}\right) \\ &= |a|^{2H}\,\mathrm{E}[B_H(s)\,B_H(t)], \end{aligned} \tag{B.118}$$

in agreement with the right-hand side of Eq. (6.6).

Prob. 6.2 Since $B_H(t)$ belongs to the family of Gaussian processes, the difference between values of the process at different times forms a Gaussian random variable; it thus suffices to prove that the increments have identical means and variances. Since $\mathrm{E}[B_H(t)]=0$ by construction, we need only prove that the variance of an increment depends only on the difference between the two times. We therefore have

$$\begin{aligned} &\mathrm{E}\Big\{\left[B_H(t+s)-B_H(t)\right]^2\Big\} \\ &\quad= \mathrm{E}\big[B_H^2(t+s)\big]+\mathrm{E}\big[B_H^2(t)\big]-2\mathrm{E}[B_H(t+s)\,B_H(t)] \\ &\quad= \mathrm{E}\big[B_H^2(1)\big]\,\left[|t+s|^{2H}+|t|^{2H}-2\cdot\tfrac{1}{2}\left(|t+s|^{2H}+|t|^{2H}-|s|^{2H}\right)\right] \\ &\quad= \mathrm{E}\big[B_H^2(1)\big]\,|s|^{2H}, \end{aligned} \tag{B.119}$$

which is independent of t. Thus, the increment statistics indeed depend only on the time span over which the increment exists (s) and not on the absolute time of the two values (t).

Prob. 6.3.1 Substituting Eq. (6.1) into Eq. (6.28) three times yields

$$\begin{aligned} \rho(s,t) &\equiv \frac{\mathrm{E}[B_H(s)\,B_H(t)]}{\left(\mathrm{E}\big[B_H^2(s)\big]\;\mathrm{E}\big[B_H^2(t)\big]\right)^{1/2}} \\ &= \frac{\tfrac{1}{2}\mathrm{E}[B_H^2(1)]\,\left(|t|^{2H}+|s|^{2H}-|t-s|^{2H}\right)}{\left(\mathrm{E}[B_H^2(1)]\,|s|^{2H}\,\mathrm{E}[B_H^2(1)]\,|t|^{2H}\right)^{1/2}} \\ &= \frac{|t|^{2H}+|s|^{2H}-|t-s|^{2H}}{2|s|^{H}\,|t|^{H}} \\ &= \tfrac{1}{2}\left(|t/s|^{H}+|s/t|^{H}-\left|\sqrt{|t/s|}-\mathrm{sgn}(s/t)\sqrt{|s/t|}\,\right|^{2H}\right), \end{aligned} \tag{B.120}$$

where $\mathrm{sgn}(x)$ denotes the sign of the argument x. Equation (B.120) indeed depends only on the ratio of the two times, s/t.

Prob. 6.3.2 For the special case $s = -t$, we make this substitution into Eq. (B.120) to obtain

$$\begin{aligned}\rho(-t,t) &= \tfrac{1}{2}\left(|-1|^H + |-1|^H - \left|\sqrt{1} - \mathrm{sgn}(-1)\sqrt{1}\,\right|^{2H}\right) \\ &= \tfrac{1}{2}\left(1 + 1 - |1-(-1)|^{2H}\right) \\ &= 1 - 2^{2H-1}. \end{aligned} \tag{B.121}$$

To make $B_H(t)$ and $B_H(-t)$ independent, it suffices to make them uncorrelated since first- and second-order statistics determine a Gaussian process, and $B_H(t)$ has zero mean. So we require that the autocorrelation coefficient assume a value of zero

$$\begin{aligned}\rho(-t,t) &= 0 \\ 1 - 2^{2H-1} &= 0 \\ 0 &= 2H-1 \\ H &= \tfrac{1}{2}, \end{aligned} \tag{B.122}$$

so that only for regular Brownian motion ($H = \frac{1}{2}$) do we have $B_H(t)$ and $B_H(-t)$ independent.

Prob. 6.4 The simplest method of proving this result invokes Eq. (2.15) directly, and leads to

$$\mathrm{E}\left[B^2(1)\right] = \min(1,1) = 1. \tag{B.123}$$

However, substituting $H = \frac{1}{2}$ into Eq. (6.2) yields the same result, as we now show. We first rewrite Eq. (6.2), making use of a property of the Gamma function presented in Eq. (5.8). Substituting $x = 2H$ in Eq. (5.8), and in turn substituting this into Eq. (6.2), leads to

$$\begin{aligned}\mathrm{E}[B_H^2(1)] &= \Gamma(1-2H)\cos(\pi H)/(\pi H) \\ &= \frac{\pi}{\sin(2\pi H)\,\Gamma(2H)}\,\frac{\cos(\pi H)}{(\pi H)} \\ &= \frac{\pi}{2\sin(\pi H)\,\cos(\pi H)\,\Gamma(2H)}\,\frac{\cos(\pi H)}{(\pi H)} \\ &= \left[2H\sin(\pi H)\,\Gamma(2H)\right]^{-1} \\ \mathrm{E}[B_{1/2}^2(1)] &= 1, \end{aligned} \tag{B.124}$$

as it must.

Prob. 6.5.1 We begin by defining

$$\begin{aligned} x_0 &\equiv B(k\tau_0) \\ x_1 &\equiv B[(k+1)\tau_0] \\ x_h &\equiv B[(k+\tfrac{1}{2})\tau_0]. \end{aligned} \tag{B.125}$$

We then have

$$x_h = a\mathcal{N}(0,1) + b + \tfrac{1}{2}(x_0 + x_1) \tag{B.126}$$

and it remains to find the constants a and b. Taking expectations of both sides of Eq. (B.126) immediately yields $b = 0$, so we may remove it from further consideration. Accounting for this result, we double, square, and take expectations of both sides of Eq. (B.126), to obtain

$$\begin{aligned} 4\mathrm{E}[x_h^2] &= 4a^2\,\mathrm{E}[\mathcal{N}^2(0,1)] + \mathrm{E}[x_0^2] + \mathrm{E}[x_1^2] \\ &\quad + 2\mathrm{E}[x_0\,x_1] + 2\mathrm{E}[x_0\,\mathcal{N}(0,1)] + 2\mathrm{E}[x_1\,\mathcal{N}(0,1)]. \end{aligned} \tag{B.127}$$

Since we assume that $\mathcal{N}(0,1)$ is independent of both x_0 and x_1, we can replace the expectation of the product with the product of the expectations in each case. But since at least one of the quantities has zero mean (actually, both do), the product of the expectations assumes a value of zero. Thus, the last two terms in Eq. (B.127) vanish. The first term on the right-hand side of Eq. (B.127) involves the mean square of $\mathcal{N}(0,1)$, which assumes a value of unity by construction. Eq. (B.127) therefore becomes

$$4\mathrm{E}[x_h^2] = 4a^2 + \mathrm{E}[x_0^2] + \mathrm{E}[x_1^2] + 2\mathrm{E}[x_0\,x_1]. \tag{B.128}$$

For the remaining terms, we employ Eq. (2.15). Assuming $k \geq 0$ for positive times, and substituting all of these simplifications into Eq. (B.128) yields

$$\begin{aligned} 4[(k+\tfrac{1}{2})\tau_0] &= 4a^2 + k\tau_0 + (k+1)\tau_0 + 2k\tau_0 \\ (4k+2)\tau_0 &= 4a^2 + (4k+1)\tau_0 \\ \tau_0 &= 4a^2 \\ a &= \sqrt{\tau_0}/2, \end{aligned} \tag{B.129}$$

which, in turn, we substitute into Eq. (B.126) to provide the final answer.

Prob. 6.5.2 This method is suitable for regular Brownian motion since $B(t)$ has independent increments; in particular, $B[(k+\frac{1}{2})\tau_0] - B(k\tau_0)$ and $B[(n+\frac{1}{2})\tau_0] - B(n\tau_0)$ are independent for $k \neq n$.

Prob. 6.5.3 Similarly, the method fails for fractional Brownian motion with $H \neq \frac{1}{2}$ because $B_H(t)$ does not have independent increments; in particular, $B_H[(k+\frac{1}{2})\tau_0] - B_H(k\tau_0)$ and $B_H[(n+\frac{1}{2})\tau_0] - B_H(n\tau_0)$ are *not* independent for $H \neq \frac{1}{2}$, regardless of the value of k or n.

Prob. 6.6.1 If $dN_1(t)$ has a spectrum that decays as $\sim f^{-\alpha_X}$ where $\frac{1}{2} < \alpha_X < 1$ over some large range of frequencies, then Eq. (5.44) indicates that $dN_1(t)$ must have a coincidence rate that decays as $\sim t^{\,\alpha_X - 1}$. Equation (4.24) reveals that the autocorrelation of the rates $X_k(t)$ must, over a wide range of delay times t and for some cutoff time t_1, have a similar form, such as

$$R_X(t) \approx (t/t_1)^{\alpha_X - 1}. \tag{B.130}$$

Subtracting the mean does not change Eq. (B.130).

Direct substitution of Eq. (B.130) into Eq. (6.16) yields

$$\begin{aligned} R_\mu(t) &= 2M\,R_X^2(t) + \mathrm{E}^2[\mu] \\ &\approx 2M(t/t_1)^{2\alpha_X - 2} + M^2\,\mathrm{Var}^2[X] \\ &= c_1\left[1 + (t/t_2)^{2\alpha_X - 2}\right], \end{aligned} \tag{B.131}$$

where c_1 and t_2 are constants implicitly defined by Eq. (B.131). Equation (B.131) shows that $\mu(t)$ has a different exponent than $X(t)$; since $2\alpha_X - 2 = \alpha_\mu - 1$, we have $\alpha_\mu = 2\alpha_X - 1$. Finally, using Eqs. (4.24) and (5.44) once again, we see that $dN_2(t)$ exhibits behavior of the form

$$S_{N_2}(f) \sim f^{-\alpha_\mu} = f^{1-2\alpha_X}, \tag{B.132}$$

which stands in contrast to the $S_{N_1}(f) \sim f^{-\alpha_X}$ behavior attendant to $dN_1(t)$. Since $\frac{1}{2} < \alpha_X < 1$, we have $0 < \alpha_\mu < 1$, and Eq. (5.44) indeed applies.

Prob. 6.6.2 A similar argument to that used for Prob. 6.6.1 shows that $R_X(t)$ must vary as $\sim t^{\alpha_X - 1}$ as before. But $R_X(t)$ approaches a nonzero value for large delay times t, so it must have a form similar to

$$R_X(t) \approx \mathrm{E}^2[X]\left[1 + (t/t_1)^{\alpha_X - 1}\right], \tag{B.133}$$

for some cutoff time t_1. Direct substitution of Eq. (B.133) into Eq. (6.16) yields

$$\begin{aligned} R_\mu(t) &= 2M\,R_X^2(t) + \mathrm{E}^2[\mu] \\ &\approx 2M\Big\{\mathrm{E}^2[X]\left[1 + (t/t_1)^{\alpha_X - 1}\right]\Big\}^2 + M^2\,\mathrm{E}^2[X^2] \\ &= 2M\,\mathrm{E}^4[X]\left[1 + 2(t/t_1)^{\alpha_X - 1} + (t/t_1)^{2\alpha_X - 2}\right] \\ &\quad + M^2\,\mathrm{E}^2[X^2]. \end{aligned} \tag{B.134}$$

The important times here lie in the range $t/t_1 \gg 1$, since the tail of the autocorrelation determines the fractal behavior of the process. The autocorrelation behavior for $t/t_1 \ll 1$ cannot follow the form above, since that would lead to a large autocorrelation that exceeds the mean square, an impossibility. Furthermore, $t/t_1 \ll 1$ corresponds to high frequencies, where the constant term $\mathrm{E}[X]$ dominates the spectrum of $dN_1(t)$, making other, subtle contributions to the spectrum irrelevant.

Taking the limit $t/t_1 \gg 1$, we see that the first two terms within the square brackets in Eq. (B.134) dominate the last, which we therefore neglect. Continuing, we obtain

$$\begin{aligned} R_\mu(t) &\approx 2M\,\mathrm{E}^4[X]\left[1 + 2(t/t_G)^{\alpha_X - 1}\right] + M^2\,\mathrm{E}^2[X^2] \\ &= c_2\left[1 + c_3(t/t_1)^{\alpha_X - 1}\right] \\ &= c_2\left[1 + (t/t_3)^{\alpha_X - 1}\right], \end{aligned} \tag{B.135}$$

where c_2, c_3, and t_3 are constants implicitly defined by Eq. (B.135).

Equation (B.135) shows that $\mu(t)$ has the same exponent as $X(t)$ for large mean values $\mathrm{E}[X]$. Equations (4.24) and (5.44) thus reveal that the spectrum for $dN_2(t)$ takes the form

$$S_{N2}(f) \sim f^{-\alpha_\mu} = f^{-\alpha_X}, \tag{B.136}$$

which is the same as that for $dN_1(t)$.

Prob. 6.7 The exponential transform of a Gaussian process gives rise to a lognormal process with a mean given by Eq. (6.21) with $n = 1$:

$$\mathrm{E}[\mu] = \exp\bigl(\mathrm{E}[X] + \mathrm{Var}[X]/2\bigr). \tag{B.137}$$

As shown in Eq. (3.59), this value $\mathrm{E}[\mu]$ becomes the high-frequency asymptote of the point-process spectrum. Turning now to the autocorrelation, Eq. (6.22) provides

$$\begin{aligned} R_\mu(t) &\approx \mathrm{E}^2[\mu]\,\exp\Bigl\{R_X(t) - \mathrm{E}^2[X]\Bigr\} \\ &= \mathrm{E}^2[\mu]\,\exp\Bigl\{\mathrm{E}^2[X] + c\ln(t_0/|t|) - \mathrm{E}^2[X]\Bigr\} \\ &= \mathrm{E}^2[\mu]\,\exp\bigl[c\ln(t_0/|t|)\bigr] \\ &= \mathrm{E}^2[\mu]\,(|t|/t_0)^{-c}. \end{aligned} \tag{B.138}$$

However, since the limit of the autocorrelation for large arguments must approach the square of the mean, we write

$$R_\mu(t) \approx \mathrm{E}^2[\mu]\Bigl[1 + (|t|/t_0)^{-c}\Bigr], \tag{B.139}$$

where we acknowledge the approximate nature of Eq. (6.29).

Taking the Fourier transform of the autocorrelation yields

$$\begin{aligned} S_\mu(f) &\approx \int_{-\infty}^{\infty} R_\mu(t)\,\exp(-i2\pi ft)\,dt \\ &= \int_{-\infty}^{\infty} \mathrm{E}^2[\mu]\Bigl[1 + (|t|/t_0)^{-c}\Bigr]\exp(-i2\pi ft)\,dt \\ &= \mathrm{E}^2[\mu]\,\delta(f) \\ &\quad + 2\mathrm{E}^2[\mu]\,t_0^c\,\cos[\pi(c-1)/2]\,(2\pi f)^{c-1}\,\Gamma(1-c). \end{aligned} \tag{B.140}$$

Combining Eqs. (B.140) and (4.25) yields

$$\begin{aligned} S_N(f) &= S_\mu(f) + \mathrm{E}[\mu] \\ &= \mathrm{E}^2[\mu]\,\delta(f) \\ &\quad + \mathrm{E}[\mu]\left\{1 + 2\cos[\pi(c-1)/2]\,\Gamma(1-c)\,(2\pi)^{c-1}\,\mathrm{E}[\mu]\,t_0^c\,f^{c-1}\right\} \\ &= \mathrm{E}^2[\mu]\,\delta(f) + \mathrm{E}[\mu]\left[1 + (f/f_S)^{-\alpha}\right], \end{aligned} \tag{B.141}$$

where we make the connection to Eq. (5.44a) by identifying

$$\begin{aligned} \alpha &= 1 - c \\ (2\pi f_S)^\alpha &= 2\cos(\pi\alpha/2)\,\Gamma(\alpha)\,\mathrm{E}[\mu]\,t_0^{1-\alpha}. \end{aligned} \tag{B.142}$$

Prob. 6.8.1 For a fixed membrane voltage V, spontaneous vesicular exocytosis would be expected to lack memory; knowledge of previous event occurrence times would yield no additional information about the future, beyond that provided by the mean rate μ of the exocytic events. This lack of memory dictates that the homogeneous Poisson process characterizes the exocytic events.

Prob. 6.8.2 Different *fixed* membrane voltages V would lead to spontaneous exocytic patterns different only in their mean rates; the homogeneous Poisson process would serve as a suitable model for each of these sequences of events, whatever the voltage. The Poisson rate for each cell would be exponentially related to its cellular membrane voltage, as prescribed by Eq. (6.30).

Prob. 6.8.3 Since the resting membrane voltage V exhibits $1/f$-type noise with a Gaussian amplitude distribution, we accommodate the attendant voltage fluctuations by replacing V by the fractal Gaussian process $V(t)$ in Eq. (6.30):

$$\mu(t) = \mathcal{A} \exp\{-\left[E_A - qV(t)\right] / \mathcal{RT}\}. \tag{B.143}$$

Because the rate $\mu(t)$ is the exponential transform of the Gaussian process $V(t)$, Eq. (B.143) dictates that the rate behave as fractal lognormal noise. A model for the discrete exocytic sequence therefore belongs to the Poisson-process family, but is governed by a rate that varies in accordance with lognormal statistics with a fractal spectrum. This leads to the fractal-lognormal-noise-driven Poisson process described in Sec. 6.5.

We connect the results developed here with those provided in Sec. 6.5 by defining $X(t)$ as a normalized[2] version of the membrane voltage $V(t)$:

$$X(t) \equiv \ln(\mathcal{A}) + \left[qV(t) - E_A\right] / \mathcal{RT}, \tag{B.144}$$

so that the rate in Eq. (B.143) can become

$$\mu(t) = \exp[X(t)]. \tag{B.145}$$

Since it is a linear transform of the Gaussian membrane voltage $V(t)$, the auxiliary process $X(t)$ also behaves as a Gaussian process, with associated mean, variance, and autocorrelation given by:

$$\begin{aligned} \mathrm{E}[X] &= \ln(\mathcal{A}) + (q\,\mathrm{E}[V] - E_A) / \mathcal{RT} \\ \mathrm{Var}[X] &= (q/\mathcal{RT})^2\,\mathrm{Var}[V] \\ R_X(t) &= \mathrm{E}^2[X] + (q/\mathcal{RT})^2 \left\{R_V(t) - \mathrm{E}^2[V]\right\}. \end{aligned} \tag{B.146}$$

The quantities in Eq. (B.146), when substituted into Eqs. (6.20)–(6.25), yield results for the point process that describes the exocytic events, and its rate, in terms of the statistics of the membrane voltage (Lowen et al., 1997a,b).

[2] The process $X(t)$ has mixed units. We use this somewhat unusual approach to simplify notation; making use of a dimensionless process for $X(t)$ yields the same results, albeit with more cumbersome algebra.

B.7 FRACTAL RENEWAL PROCESSES

Prob. 7.1 We can achieve $\alpha = \frac{1}{2}$ by employing either $\gamma = \frac{1}{2}$ or $\gamma = 2 - \frac{1}{2} = \frac{3}{2}$. For the former, we make use of Eq. (5.3) together with the first line of Eq. (7.8), which yield

$$\begin{aligned} \mathrm{E}[\mu]\left[1 + (f/f_S)^{-\gamma}\right] &= \mathrm{E}[\mu]\left\{1 + 2\big[\Gamma(1-\gamma)\big]^{-1}\cos(\pi\gamma/2)\,(2\pi f A)^{-\gamma}\right\} \\ (f/f_S)^{-1/2} &= 2\big[\Gamma(\tfrac{1}{2})\big]^{-1}\cos(\pi/4)\,(2\pi f A)^{-1/2} \\ 2\pi f_S\, A &= \left\{2\big[\sqrt{\pi}\,\big]^{-1}\,2^{-1/2}\right\}^2 \\ A &= \pi^{-2}/f_S \\ &\doteq 0.0101321 \text{ sec.} \end{aligned} \tag{B.147}$$

Equation (7.2) then provides

$$\begin{aligned} 1/\mathrm{E}[\mu] &= \frac{1/2}{1-1/2}\,(A/B)^{1/2}\,B\,\frac{1-(A/B)^{1-1/2}}{1-(A/B)^{1/2}} \\ &= \sqrt{AB} \\ &= \sqrt{(\pi^{-2}/f_S)\times 10^6(\pi^{-2}/f_S)} \\ \mathrm{E}[\mu] &= 10^{-3}\,\pi^2 f_S \\ &\doteq 0.0986960 \text{ events/sec.} \end{aligned} \tag{B.148}$$

The calculation for $\gamma = \frac{3}{2}$ proceeds along the same lines. Using the third line of Eq. (7.8) yields

$$\begin{aligned} 2\pi f_S\, A &= \left\{2(\tfrac{3}{2})^{-2}\,(\tfrac{3}{2}-1)\,\Gamma(2-\tfrac{3}{2})\,\big[-\cos(3\pi/4)\big]\right\}^2 \\ &= \left\{(\tfrac{4}{9})\,\Gamma(\tfrac{1}{2})\,2^{-1/2}\right\}^2 \\ A &= (4/81)/f_S \\ &\doteq 0.00493827 \text{ sec.} \end{aligned} \tag{B.149}$$

For this value of γ, Eq. (7.2) returns

$$\begin{aligned} 1/\mathrm{E}[\mu] &= \frac{3/2}{1-3/2}\,(A/B)^{3/2}\,B\,\frac{1-(A/B)^{1-3/2}}{1-(A/B)^{3/2}} \\ &= \frac{3A}{1+\sqrt{A/B}+A/B} \\ &= \frac{3(4/81)/f_S}{1+10^{-3}+10^{-6}} \\ \mathrm{E}[\mu] &\doteq 67.5676 \text{ events/sec.} \end{aligned} \tag{B.150}$$

Prob. 7.2 For the range of times $A \ll t \ll B$, both exponentials in Eq. (7.5) have small arguments and therefore approach unity. Furthermore, we have $\mathrm{K}_\gamma(z) \approx 2^{\gamma-1}\,\Gamma(\gamma)\,z^{-\gamma}$, valid for small values of the argument z (Gradshteyn & Ryzhik, 1994, Secs. 8.445 and 8.485). Employing these simplifications in Eq. (7.5) yields

$$\begin{aligned} p_\tau(t) &= \frac{(AB)^{\gamma/2}}{2\mathrm{K}_\gamma\Big(2\sqrt{A/B}\Big)}\, e^{-A/t}\, e^{-t/B}\, t^{-(\gamma+1)} \\ &\approx \frac{(AB)^{\gamma/2}}{2\,(2^{\gamma-1})\,\Gamma(\gamma)\left(2\sqrt{A/B}\right)^{-\gamma}}\, t^{-(\gamma+1)} \\ &= \frac{(AB)^{\gamma/2}}{\Gamma(\gamma)\,(A/B)^{-\gamma/2}}\, t^{-(\gamma+1)} \\ &= \frac{A^\gamma}{\Gamma(\gamma)}\, t^{-(\gamma+1)} \\ &= \gamma A^\gamma \big[\Gamma(1+\gamma)\big]^{-1}\, t^{-(\gamma+1)}, \end{aligned} \tag{B.151}$$

which, for $A \ll B$, differs from Eq. (7.1) only by the factor $\big[\Gamma(1+\gamma)\big]^{-1}$. By scaling arguments, the expression corresponding to Eq. (7.4) must also differ by this same factor, so that

$$1 - \phi_\tau(\omega) \approx \frac{\Gamma(1-\gamma)}{\Gamma(1+\gamma)}\,(i\omega\,A)^\gamma. \tag{B.152}$$

Prob. 7.3 Substituting Eq. (7.4) into Eq. (4.16) yields

$$\begin{aligned} S_N(f)/\mathrm{E}[\mu] &= \mathrm{Re}\left\{\frac{1+\phi_\tau(2\pi f)}{1-\phi_\tau(2\pi f)}\right\}, \quad B^{-1} \ll f \ll A^{-1} \\ &\approx \mathrm{Re}\left\{\frac{1+1-\Gamma(1-\gamma)\,(i2\pi f A)^\gamma}{1-\big[1-\Gamma(1-\gamma)\,(i2\pi f A)^\gamma\big]}\right\} \\ &\approx \mathrm{Re}\left\{\frac{2}{\Gamma(1-\gamma)\,(2\pi f A)^\gamma}\,\big[\exp(i\pi/2)\big]^{-\gamma}\right\} \\ &= 2\big[\Gamma(1-\gamma)\big]^{-1}(2\pi f A)^{-\gamma}\,\mathrm{Re}\{\exp(-i\gamma\pi/2)\} \\ &= 2\big[\Gamma(1-\gamma)\big]^{-1}\cos(\gamma\pi/2)\,(2\pi f A)^{-\gamma}, \end{aligned} \tag{B.153}$$

where we have made use of Eq. (A.35).

Prob. 7.4.1 For $1 < \gamma < 2$ and $A \ll B$, we can take the limit $B \to \infty$ in Eq. (7.1) before calculating the mean interevent interval. The generalized Pareto result emerges:

$$\begin{aligned} 1/\mathrm{E}[\mu] &\approx \gamma A^\gamma \int_A^\infty t^{-\gamma}\,dt \\ &\approx \gamma(\gamma-1)^{-1}\,A \end{aligned}$$

$$A \approx \left(1-\gamma^{-1}\right)/\,\mathrm{E}[\mu]. \tag{B.154}$$

Recall that the expression to the right of the large left brace in Eq. (7.8) assumes a value of unity at the fractal onset frequency f_S. Combining that result with Eq. (B.154) yields

$$2\gamma^{-2}\,(\gamma-1)\,\Gamma(2-\gamma)\,\left[-\cos(\pi\gamma/2)\right]\,\left[2\pi f_S\left(1-\gamma^{-1}\right)/\,\mathrm{E}[\mu]\right]^{\gamma-2} \approx 1, \tag{B.155}$$

which relates $\mathrm{E}[\mu]$ to f_S, as promised.

Prob. 7.4.2 For $0 < \alpha < 1$, we again begin with the mean interevent time; Eq. (7.2) yields

$$\begin{aligned}
1/\mathrm{E}[\mu] &= \frac{\gamma}{1-\gamma}\,(A/B)^{\gamma}\,B\,\frac{1-(A/B)^{1-\gamma}}{1-(A/B)^{\gamma}} \\
&\approx \frac{\gamma}{1-\gamma}\,(A/B)^{\gamma}\,B \\
&= \gamma(1-\gamma)^{-1}\,(B/A)^{1-\gamma}\,A \\
1/\mathrm{E}[\mu] &\gg A \\
\mathrm{E}[\mu] &\ll 1/A.
\end{aligned} \tag{B.156}$$

Ignoring factors of the order of unity in Eq. (7.8) we obtain

$$\begin{aligned}
1 &= 2\gamma^{-2}\,(\gamma-1)\,\Gamma(2-\gamma)\,\left[-\cos(\pi\gamma/2)\right]\,(2\pi f_S A)^{\gamma-2} \\
1 &\approx (2\pi f_S A)^{\gamma-2} \\
1 &\approx 2\pi f_S A \\
f_S &\approx 1/A.
\end{aligned} \tag{B.157}$$

Finally, combining Eqs. (B.156) and (B.157) leads to the inequality

$$\mathrm{E}[\mu] \ll f_S. \tag{B.158}$$

Prob. 7.5 We immediately take the limit $B \to \infty$ in Eq. (7.1), as in Prob. 7.4.1. Equation (3.6) then provides

$$1-\phi_\tau(\omega) \approx \gamma A^{\gamma}\int_A^{\infty}\left(1-e^{-i\omega t}\right)\,t^{-(\gamma+1)}\,dt. \tag{B.159}$$

We proceed to integrate by parts, with $U = 1-e^{-i\omega t}$ and $dV = \gamma t^{-(\gamma+1)}\,dt$, which leads to

$$\begin{aligned}
1-\phi_\tau(\omega) &\approx A^{\gamma}\,i\omega\int_A^{\infty} e^{-i\omega t}\,t^{-\gamma}\,dt \\
&= A^{\gamma}\,i\omega\int_{iA\omega}^{\infty} e^{-x}\,x^{-\gamma}\,dx\,(i\omega)^{\gamma-1} \\
&\approx (i\omega A)^{\gamma}\int_0^{\infty} e^{-x}\,x^{-\gamma}\,dx \\
&= \Gamma(1-\gamma)\,(i\omega A)^{\gamma}.
\end{aligned} \tag{B.160}$$

Prob. 7.6 For $\gamma = \frac{1}{2}$ we have

$$\mathrm{E}[\tau] = \sqrt{AB} = \sqrt{10^{-3} \times 10^{3}} = 1; \tag{B.161}$$

with a simulation duration of $L = 10^8$ the expected number of events is $\mathrm{E}[N(L)] = 10^8$. For $\gamma = \frac{3}{2}$, on the other hand, the mean interevent time becomes

$$\mathrm{E}[\tau] = \frac{3A}{1 + \sqrt{A/B} + A/B} = \frac{0.003}{1.001001} \tag{B.162}$$

so that

$$\mathrm{E}[N(L)] = 10^8 \times 1.001001/0.003 = 3.33667 \times 10^{10}. \tag{B.163}$$

Simulating this fractal renewal point process would thus take 333.667 times as long as for $\gamma = \frac{1}{2}$. Hence, the total computation time would lie in the neighborhood of 333.667 days, or about a year. Moreover, at four bytes per interval the expected file size would reach 133.4668 GB, which greatly exceeds the memory of the computer employed to carry out the calculations. This would necessitate reading in the entire file for each value of the counting time T, which would, in turn, greatly increase the calculation time. An educated guess would then put the computation time in excess of 20 years. Decreasing the duration L serves to reduce simulation times at the expense of accuracy in the resulting estimates. For purposes of illustrating fractal behavior, rather than producing smooth and accurate curves, a duration $\mathrm{E}[N(L)] = 10^6$ suffices, whereupon the estimated simulation time decreases to about 15 minutes (see Prob. 12.8).

Prob. 7.7 Since the overall error process has independent interevent intervals, we consider renewal-point-process models. It therefore remains only to find the form of the inter-error probability density function. Over long time scales the homogeneous Poisson process dominates, so that the probability density has an exponential tail. The long-time cutoff is thus $B = \tau_{\mathrm{HPP}}$. For time scales shorter than τ_{clk}, additional events do not register, thereby imposing on the process a practical short-time cutoff of $A = \tau_{\mathrm{clk}}$. For other time scales, however, the inter-error probability density function assumes a power-law form. Thus, Eq. (7.5) provides a good representation for the fractal renewal point process that characterizes the error events.

Prob. 7.8.1 As shown in Fig. B.4, for the upper and lower cutoffs we have $\widehat{B} \approx 5$ sec and $\widehat{A} \approx 20$ msec, respectively. For intermediate values of the interevent interval t, the estimated density function decreases roughly as a straight line on this doubly logarithmic plot. This indicates a power-law dependence on the interevent interval t; we estimate the exponent to be $-\widehat{\gamma} \approx -0.8$. Based on Eq. (7.9), a fractal renewal point process with $0 < \gamma < 1$ should exhibit $\alpha = \gamma$.

Prob. 7.8.2 The dashed curve shown in Fig. B.5 provides a fit of the power-law portion of Eq. (5.44c) to the normalized-Haar-wavelet-variance data. Relative refractoriness in the neural-spike-generation mechanism gives rise to the dip below unity of the

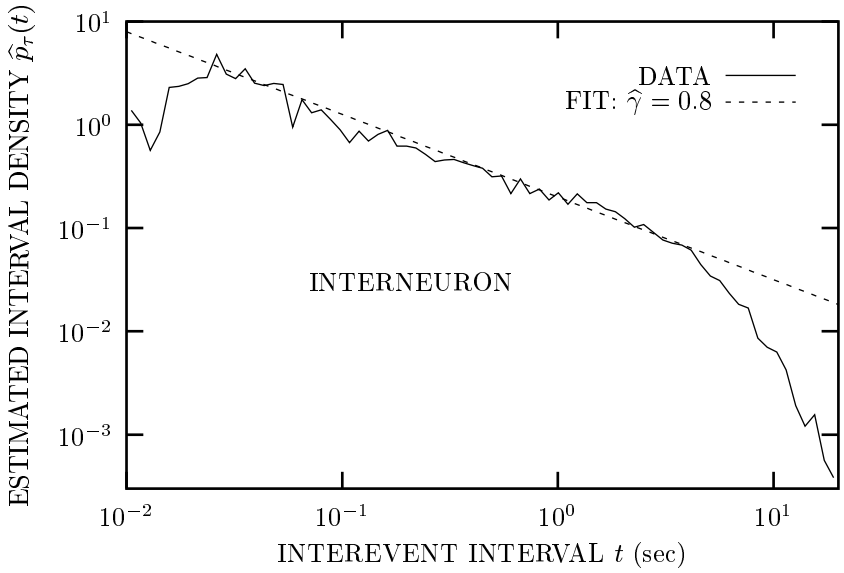

Fig. B.4 A decaying power-law function provides a good fit to the estimated interevent-interval density for the action-potential sequence recorded from the descending contralateral movement detector, a visual-system INTERNEURON in the locust (Turcott et al., 1995, Fig. 2, pp. 261–262, cell ADA062). The normalized Haar-wavelet variance for these same data is displayed in Fig. B.5.

normalized Haar-wavelet variance; it is also responsible for the soft lower cutoff A in the interevent-interval density (see Sec. 11.2.4). The curve increases with counting time T roughly as a straight line; estimating the slope and intercept of the curve gives $\widehat{\alpha}_A \approx 0.14$ and $\widehat{T}_A \approx 0.07$. Since the values of γ and α obtained from Figs. B.4 and B.5 differ so greatly, the data must not derive from a fractal renewal point process.

Prob. 7.8.3 The theoretical fractal-renewal-process power-law-decaying interevent-interval density fits the data well. In spite of this, the fractal renewal process is not a suitable model for characterizing this spike train, as will be definitively demonstrated in Prob. 11.12.

Prob. 7.9 There are four reasons why extensive data are not available for this process: First, a proper analysis requires comparative studies, which involve sequencing related proteins in a large number of different, related organisms, whereas most sequencing efforts (such as the Human Genome Project) focus on sequencing the entire genome of relatively few organisms. Second, other methods for estimating divergence dates yield imprecise results, making calibration of the model difficult. Third, evolution rates average about 10^{-7} substitutions per year for most proteins; in most cases, therefore, relatively few changes occur, making detailed calculation of the sequence-change

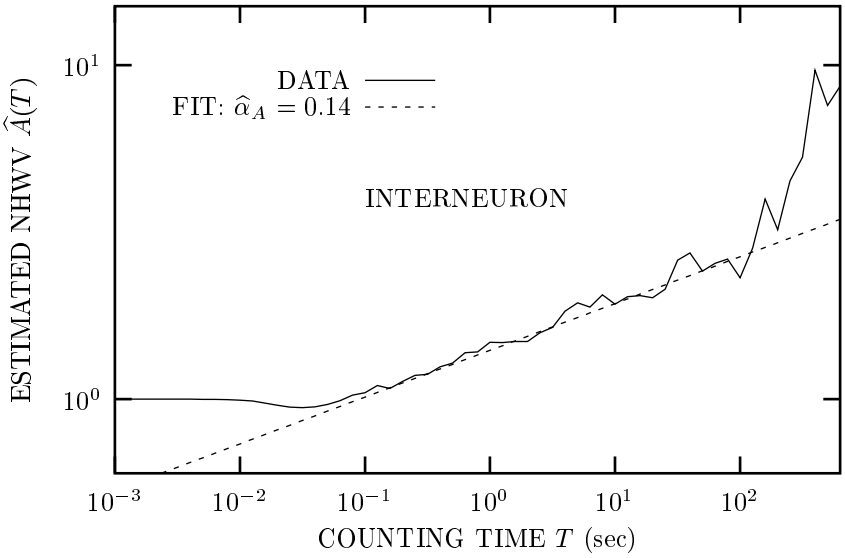

Fig. B.5 An increasing power-law function provides a good fit to the estimated normalized Haar-wavelet variance for the action-potential sequence recorded from the descending contralateral movement detector, a visual-system INTERNEURON in the locust (Turcott et al., 1995, Fig. 2, pp. 261–262, cell ADA062). However, the estimated exponent is in serious disagreement with that obtained from the estimated interevent-interval density shown in Fig. B.4.

statistics difficult. Finally, very few ancestral DNA samples exist, so substitution counts depend directly on the accuracy of cladistics, which is a particular method of phylogenetic analysis (Bickel, 2000). Nevertheless, there are sufficient data to rule out the homogeneous Poisson process, since it predicts fluctuations in the estimated substitution rate that are significantly smaller than those observed in real sequences (Gillespie, 1994). In fact, the data suggest a fractal model (West & Bickel, 1998). A variety of empirical fractal models exist for characterizing molecular evolution, including anomalous diffusion (West & Bickel, 1998), the fractal-shot-noise-driven Poisson process described in Chapter 10 (Bickel & West, 1998a), fractal Gaussian processes (Bickel, 2000), and fractal renewal point processes (Bickel & West, 1998b). The last proves simplest from a conceptual perspective so Occam's razor suggests its use, although the fractal Gaussian process is more tractable from an analytical point of view.

Prob. 7.10.1 Setting the integral of Eq. (7.26) to unity yields the normalization constant:

$$c \equiv E_0^{-1}\left[\exp(-E_L/E_0) - \exp(-E_H/E_0)\right]^{-1}. \tag{B.164}$$

Prob. 7.10.2 If we define characteristic time cutoffs $A \equiv \tau_0 \exp(E_L/\kappa\mathcal{T})$ and $B \equiv \tau_0 \exp(E_H/\kappa\mathcal{T})$, and the power-law exponent $\gamma \equiv \kappa\mathcal{T}/E_0$, the mean waiting time $q(E)$ is characterized by the power-law density

$$p_{q(E)}(s) = \frac{\gamma}{A^{-\gamma} - B^{-\gamma}} \times \begin{cases} s^{-(\gamma+1)} & A < s < B \\ 0 & \text{otherwise.} \end{cases} \tag{B.165}$$

Since the times spent in successive traps are independent, the fractal renewal process follows.

Prob. 7.10.3 Integrating over the conditioning yields

$$\begin{aligned} p_\tau(t) &= \int p_\tau\big[t|q(E) = s\big]\, p_{q(E)}(s)\, ds \\ &= \frac{\gamma}{A^{-\gamma} - B^{-\gamma}}\, t^{-(\gamma+1)} \int_{t/B}^{t/A} x^\gamma\, e^{-x}\, dx. \end{aligned} \tag{B.166}$$

For the case $A \ll t \ll B$, the limits in the integral of Eq. (B.166) can be approximated by zero and infinity, which provides

$$\begin{aligned} \lim_{\substack{A/t\to 0 \\ B/t\to\infty}} p_\tau(t) &= \frac{\gamma}{A^{-\gamma} - B^{-\gamma}}\, t^{-(\gamma+1)} \int_0^\infty x^\gamma\, e^{-x}\, dx \\ &= \frac{\gamma}{A^{-\gamma}}\, t^{-(\gamma+1)}\, \Gamma(\gamma+1) \\ &= \gamma\, \Gamma(\gamma+1)\, A^\gamma\, t^{-(\gamma+1)}. \end{aligned} \tag{B.167}$$

B.8 ALTERNATING FRACTAL RENEWAL PROCESS

Prob. 8.1 Since τ_a and τ_b have identical distributions, their means and characteristic functions must also coincide. We therefore have $\mathrm{E}[\tau_a] = \mathrm{E}[\tau_b] = \mathrm{E}[\tau]$, and $\phi_{\tau a}(\omega) = \phi_{\tau b}(\omega) = \phi_\tau(\omega)$. Using Eq. (8.5), we have

$$\begin{aligned} S_X(f) &= \mathrm{E}[X]\,\delta(f) + \frac{2(2\pi f)^{-2}}{\mathrm{E}[\tau_a] + \mathrm{E}[\tau_b]}\,\mathrm{Re}\left\{\frac{\left[1-\phi_{\tau a}(2\pi f)\right]\left[1-\phi_{\tau b}(2\pi f)\right]}{1-\phi_{\tau a}(2\pi f)\,\phi_{\tau b}(2\pi f)}\right\} \\ &= \frac{\mathrm{E}[\tau]}{\mathrm{E}[\tau]+\mathrm{E}[\tau]}\,\delta(f) + \frac{2(2\pi f)^{-2}}{\mathrm{E}[\tau]+\mathrm{E}[\tau]}\,\mathrm{Re}\left\{\frac{\left[1-\phi_\tau(2\pi f)\right]^2}{1-\phi_\tau^2(2\pi f)}\right\} \\ &= \frac{\delta(f)}{2} + \frac{(2\pi f)^{-2}}{\mathrm{E}[\tau]}\,\mathrm{Re}\left\{\frac{1-\phi_\tau(2\pi f)}{1+\phi_\tau(2\pi f)}\right\}, \end{aligned} \tag{B.168}$$

in accordance with Eq. (8.8).

Prob. 8.2 For the low frequency limit, Eq. (8.10) becomes

$$\begin{aligned} \lim_{f\to 0} S_X(f) &= \lim_{f\to 0} \frac{2\big(\mathrm{E}[\tau_a]+\mathrm{E}[\tau_b]\big)^{-1}}{(2\pi f)^2 + (2\pi f_S)^2} \\ &= \frac{2\big(\mathrm{E}[\tau_a]+\mathrm{E}[\tau_b]\big)^{-1}}{(2\pi f_S)^2} \\ &= \frac{2\big(\mathrm{E}[\tau_a]+\mathrm{E}[\tau_b]\big)^{-1}}{\big(1/\mathrm{E}[\tau_a]+1/\mathrm{E}[\tau_b]\big)^2} \\ &= \frac{2\mathrm{E}^2[\tau_a]\,\mathrm{E}^2[\tau_b]}{\big(\mathrm{E}[\tau_a]+\mathrm{E}[\tau_b]\big)^3} \\ &= \frac{\mathrm{E}^2[\tau_a]\,\mathrm{Var}[\tau_b] + \mathrm{E}^2[\tau_b]\,\mathrm{Var}[\tau_a]}{\big(\mathrm{E}[\tau_a]+\mathrm{E}[\tau_b]\big)^3}, \end{aligned} \tag{B.169}$$

in accordance with Eq. (8.6).

For the high-frequency limit, we demonstrate that as $f \to \infty$, the limit of the ratio of Eqs. (8.10) and (8.7) approaches unity:

$$\begin{aligned} &\lim_{f\to\infty} \frac{2\big(\mathrm{E}[\tau_a]+\mathrm{E}[\tau_b]\big)^{-1}}{(2\pi f)^2 + (2\pi f_S)^2} \Bigg/ 2(2\pi f)^{-2}\big(\mathrm{E}[\tau_a]+\mathrm{E}[\tau_b]\big)^{-1} \\ &\quad= \lim_{f\to\infty} \frac{(2\pi f)^2}{(2\pi f)^2 + (2\pi f_S)^2} \\ &\quad= \lim_{f\to\infty} \frac{1}{1+(f_S/f)^2} \\ &\quad= 1. \end{aligned} \tag{B.170}$$

Prob. 8.3 We calculated the characteristic function of an exponential random variable in Eq. (B.51). To cast this in a form more suitable to our present needs we replace μ by $\mathrm{E}^{-1}[\tau]$, which provides

$$\phi_\tau(\omega) = (1 + i\omega\,\mathrm{E}[\tau])^{-1}. \tag{B.171}$$

Substituting Eq. (B.171) into Eq. (8.5), and using the shorthand notations $u \equiv \mathrm{E}[\tau_u]$, $v \equiv \mathrm{E}[\tau_v]$, and $\omega \equiv 2\pi f$ yields

$$\begin{aligned}
S_X(f) &= \mathrm{E}[X]\,\delta(f) + \frac{2\omega^{-2}}{u+v}\,\mathrm{Re}\left\{\frac{\left[1-\phi_{\tau a}(\omega)\right]\left[1-\phi_{\tau b}(\omega)\right]}{1-\phi_{\tau a}(\omega)\,\phi_{\tau b}(\omega)}\right\} \\
&= \mathrm{E}[X]\,\delta(f) + \frac{2\omega^{-2}}{u+v}\,\mathrm{Re}\left\{\frac{\left[1-(1+i\omega u)^{-1}\right]\left[1-(1+i\omega v)^{-1}\right]}{1-(1+i\omega u)^{-1}\,(1+i\omega v)^{-1}}\right\} \\
&= \mathrm{E}[X]\,\delta(f) + \frac{2\omega^{-2}}{u+v}\,\mathrm{Re}\left\{\frac{\left[(1+i\omega v)-1\right]\left[(1+i\omega u)-1\right]}{(1+i\omega u)(1+i\omega v)-1}\right\} \\
&= \mathrm{E}[X]\,\delta(f) + \frac{2\omega^{-2}}{u+v}\,\mathrm{Re}\left\{\frac{-\omega^2 uv}{i\omega(u+v)-\omega^2 uv}\times\frac{-i(u+v)/\omega - uv}{-i(u+v)/\omega - uv}\right\} \\
&= \mathrm{E}[X]\,\delta(f) + \frac{2\omega^{-2}}{u+v}\,\mathrm{Re}\left\{\frac{\omega^2u^2v^2 + i\omega uv(u+v)}{\omega^2u^2v^2 + (u+v)^2}\right\} \\
&= \mathrm{E}[X]\,\delta(f) + \frac{2\omega^{-2}}{u+v}\times\frac{\omega^2}{\omega^2 + (u+v)^2u^{-2}v^{-2}} \\
&= \mathrm{E}[X]\,\delta(f) + \frac{2(u+v)^{-1}}{\omega^2 + (1/u + 1/v)^2}\,,
\end{aligned} \tag{B.172}$$

in accordance with Eq. (8.10).

Prob. 8.4 We make use of the Fourier relation between the spectrum of a real-valued process and its autocovariance. For algebraic convenience, we consider the case $t > 0$ for now. We begin by noting that in the range $1 < \gamma < 2$, and for $A/B \ll 1$, we have

$$\begin{aligned}
\mathrm{E}[\mu] &= \int_A^B t^{-(\gamma+1)}\,dt \Big/ \int_A^B t^{-\gamma}\,dt \\
&\approx \int_A^\infty t^{-(\gamma+1)}\,dt \Big/ \int_A^\infty t^{-\gamma}\,dt \\
&= \frac{A^{-\gamma}/\gamma}{A^{1-\gamma}/(\gamma-1)} \\
&= (\gamma-1)\,\gamma^{-1}\,A^{-1}.
\end{aligned} \tag{B.173}$$

Using Eq. (8.11), and then Eq. (B.173), we obtain in the mid-frequency range

$$\begin{aligned}
S_X(f) &\approx \tfrac{1}{2}(\gamma-1)^{-1}\,\Gamma(2-\gamma)\left[-\cos(\pi\gamma/2)\right]\mathrm{E}[\mu]A^\gamma\,(2\pi f)^{\gamma-2} \\
&= (2\gamma)^{-1}\,\Gamma(2-\gamma)\left[-\cos(\pi\gamma/2)\right]A^{\gamma-1}\,(2\pi f)^{\gamma-2}
\end{aligned}$$

$$\begin{aligned}
R_X(t) - \mathrm{E}^2[X] &= 2\int_{0+}^{\infty} S_X(f)\cos(2\pi f t)\,df \\
&= 2\int_0^{\infty} (2\gamma)^{-1}\,\Gamma(2-\gamma)\big[-\cos(\pi\gamma/2)\big]\,A^{\gamma-1}\,(2\pi f)^{\gamma-2} \\
&\quad \times \cos(2\pi f t)\,df \\
&= \gamma^{-1}\,\Gamma(2-\gamma)\big[-\cos(\pi\gamma/2)\big]\,A^{\gamma-1}\,t^{1-\gamma}\,(2\pi)^{-1} \\
&\quad \times \int_0^{\infty} x^{\gamma-2}\,\cos(x)\,dx \\
&= \gamma^{-1}\,\Gamma(2-\gamma)\big[-\cos(\pi\gamma/2)\big]\,A^{\gamma-1}\,t^{1-\gamma}\,(2\pi)^{-1} \\
&\quad \times \pi\Big/\Big\{2\Gamma(2-\gamma)\,\cos\big[(\pi/2)(2-\gamma)\big]\Big\} \\
&= (4\gamma)^{-1}\,A^{\gamma-1}\,t^{1-\gamma}, \qquad \text{(B.174)}
\end{aligned}$$

in accordance with Eq. (8.13). Since the correlation must be an even function, the foregoing result applies for $t < 0$ as well as $t > 0$. The notation $0+$ signifies that the integral does not contain the delta function in $S_X(f)$ at $f = 0$.

Prob. 8.5.1 Proceeding directly from the definition, we have

$$\begin{aligned}
\mathrm{E}[X_2^n] &= \mathrm{E}\{\,[b + (a-b)X_1]^n\,\} \\
&= \sum_{m=0}^{n} \binom{n}{m} b^m\,(a-b)^{n-m}\,\mathrm{E}\big[X_1^{n-m}\big] \\
&= b^n + \sum_{m=0}^{n-1} \binom{n}{m} b^m\,(a-b)^{n-m}\,\mathrm{E}[X_1] \\
&= b^n\,(1 - \mathrm{E}[X_1]) + \mathrm{E}[X_1] \sum_{m=0}^{n} \binom{n}{m} b^m\,(a-b)^{n-m} \\
&= b^n\,(1 - \mathrm{E}[X_1]) + \mathrm{E}[X_1]\;[b + (a-b)]^n \\
&= b^n + (a^n - b^n)\,\mathrm{E}[X_1]\,. \qquad \text{(B.175)}
\end{aligned}$$

Prob. 8.5.2 The definition of the autocorrelation provides

$$\begin{aligned}
R_{X2}(t) &\equiv \mathrm{E}[X_2(s)\,X_2(s+t)] \\
&= \mathrm{E}\big\{[b + (a-b)\,X_1(s)]\;[b + (a-b)\,X_1(s+t)]\big\} \\
&= b^2 + b(a-b)\,\mathrm{E}[X_1(s) + X_1(s+t)] \\
&\quad + (a-b)^2\,[X_1(s)\,X_1(s+t)] \\
&= b^2 + 2b(a-b)\,\mathrm{E}[X_1] + (a-b)^2 R_{X1}(t). \qquad \text{(B.176)}
\end{aligned}$$

Prob. 8.5.3 Suppose first that the times s and $s+t$ lie in the same "on" period. This will occur during a proportion p_1 of the times, and we then have $\mathrm{E}[X_2(s)\,X_2(s+t)] =$

$\mathrm{E}[a^2]$. For another proportion p_2 of the times, s and $s+t$ lie in different "on" periods, in which case $\mathrm{E}[X_2(s)\,X_2(s+t)] = \mathrm{E}^2[a]$. Taking expectations over the conditions, we then have the overall result

$$\mathrm{E}[X_2(s)\,X_2(s+t)] = p_1\mathrm{E}[a^2] + p_2\mathrm{E}^2[a]. \tag{B.177}$$

Equation (B.177) provides a meaningful result only if we impose the condition $\mathrm{E}[a^2] < \infty$; we therefore require this of the random variable a.

Prob. 8.5.4 To find an expression for $R_{X2}(t)$, it suffices to determine the values of p_1 and p_2 in Eq. (B.177). We can express p_1 as a product of the probability that a random time, s, lies in an "on" period, multiplied by the probability that the remaining time in this "on" period exceeds t. For the first element of this product we have simply

$$\mathrm{E}[X_1] = \frac{\mathrm{E}[\tau_a]}{\mathrm{E}[\tau_a] + \mathrm{E}[\tau_b]}\,, \tag{B.178}$$

whereas for the second we have the recurrence time

$$p_\vartheta(t) = \frac{1 - P_{\tau a}(t)}{\mathrm{E}[\tau_a]}. \tag{B.179}$$

The product of Eqs. (B.178) and (B.179) yields the probability p_1:

$$p_1 = \frac{\mathrm{E}[\tau_a]}{\mathrm{E}[\tau_a] + \mathrm{E}[\tau_b]} \times \frac{1 - P_{\tau a}(t)}{\mathrm{E}[\tau_a]} = \frac{1 - P_{\tau a}(t)}{\mathrm{E}[\tau_a] + \mathrm{E}[\tau_b]}. \tag{B.180}$$

For deterministic a fixed at $a = 1$, we see that both p_1 and p_2 contribute to $R_{X1}(t)$; this actually holds for any a, and we therefore have

$$p_1 + p_2 = R_{X1}(t). \tag{B.181}$$

Combining Eqs. (B.177), (B.180), and (B.181), we obtain the final result

$$\begin{aligned} R_{X2}(t) &= p_1\mathrm{E}[a^2] + p_2\mathrm{E}^2[a] \\ &= p_1\big(\mathrm{E}[a^2] - \mathrm{E}^2[a]\big) + R_{X1}(t)\,\mathrm{E}^2[a] \\ &= \mathrm{Var}[a]\,\frac{1 - P_{\tau a}(t)}{\mathrm{E}[\tau_a] + \mathrm{E}[\tau_b]} + \mathrm{E}^2[a]\,R_{X1}(t). \end{aligned} \tag{B.182}$$

We note that Eq. (B.176) with $b = 0$ agrees with Eq. (B.182) with deterministic a, as it must.

Prob. 8.6.1 Integrating the power-law density of Eq. (7.1) yields

$$P_\tau(t) = \begin{cases} 0 & t \le A \\ \left(A^{-\gamma} - t^{-\gamma}\right) / \left(A^{-\gamma} - B^{-\gamma}\right) & A < t < B \\ 1 & t \ge B. \end{cases} \tag{B.183}$$

We can set Eq. (B.183) equal to X_U and solve for τ.

However, since this can involve the difference between two large numbers, it proves more useful to set Eq. (B.183) equal to $1 - X_U$ instead. Since $1 - X_U$ and X_U have identical distributions, this improves the computational accuracy without changing the underlying mathematics. Solving for τ then yields

$$\tau \equiv AB\left[\left(B^\gamma - A^\gamma\right) X_U + A^\gamma\right]^{-1/\gamma}. \tag{B.184}$$

Finally, we set $\gamma = 2 - \alpha$ in accordance with Eq. (8.12), and choose $A = 1/f_H$ and $B = 1/f_L$. An alternating fractal renewal process constructed from these three parameters (γ, A, B) will therefore satisfy the design requirements.

Prob. 8.6.2 Turning to Eq. (8.17) we have the design constraints

$$\begin{aligned} \frac{|1-2r|}{\sqrt{Mr(1-r)}} &< \epsilon \qquad \text{a)} \\ \frac{1}{M}\left|\frac{1}{r(1-r)} - 6\right| &< \epsilon. \qquad \text{b)} \end{aligned} \tag{B.185}$$

Setting $r = \frac{1}{2}$ satisfies Eq. (B.185a) for any value of M, while choosing $r = \frac{1}{2} \pm 1/\sqrt{12}$ provides the same for Eq. (B.185b). Since the two values of r differ, one of the constraints must be satisfied by adjusting the value of M. Setting $r = \frac{1}{2}$ and solving Eq. (B.185b) yields $M > 2/\epsilon$, while setting $r = \frac{1}{2} \pm 1/\sqrt{12}$ yields $M > 2/\epsilon^2$ via Eq. (B.185a). Since $\epsilon < 1$, the former constraint proves less stringent, and we therefore set $r = \frac{1}{2}$ and choose for M the smallest integer $> 2/\epsilon$. We therefore choose components that are symmetric alternating fractal renewal processes, since $r = \frac{1}{2}$, and sum at least $2/\epsilon$ of them together.

B.9 FRACTAL SHOT NOISE

Prob. 9.1.1 With identical impulse response functions for each $X_m(t)$, the sole difference between the resulting process $X_R(t)$ and the component processes $X_m(t)$ becomes the times at which the impulse response functions begin. Since these points derive from an independent homogeneous Poisson process for each process $X_m(t)$, there is no memory at all within or among these point processes. Their superposition must therefore also lack memory, and must also belong to the homogeneous Poisson point-process family. The total rate is given by $\mu_R = \sum_{m=1}^{M} \mu_m$, but otherwise $X_R(t)$ and $X_1(t)$ do not differ. This defines $X_R(t)$ as a shot-noise process.

Prob. 9.1.2 We can still make use of a shot noise framework for characterizing $X_R(t)$ if we employ random values of K to index the appropriate impulse response function. In other words, define $h_R(K,t)$ so that $h_R(m,t) = h_m(t)$, and define K so that $K = m$ for a proportion μ_m/μ_R of the homogeneous Poisson point-process events. The absence-of-memory argument of Prob. 9.1.1 remains applicable, so the result $X_R(t)$ remains a shot-noise process.

Prob. 9.1.3 If the fractal exponents differ for any two of the component shot noise processes $X_m(t)$, say m_1 and m_2, then the spectrum assumes the form

$$S_{XR}(f) \approx (f/f_{Sm1})^{-\alpha_{m1}} + (f/f_{Sm2})^{-\alpha_{m2}}. \tag{B.186}$$

Equation (B.186) must have a breakpoint at some value of f, with different effective slopes (values of α) on either side of the breakpoint. The result does not belong to the fractal shot-noise family of processes. Thus, for $X_R(t)$ to belong to this family, we require that all $X_m(t)$ have the same value of α.

Prob. 9.1.4 For this impulse response function we have

$$\begin{aligned} h_m(t) &= \exp(-c_m t) \\ H_m(f) &= \int_0^\infty \exp(-c_m t)\, \exp(-i2\pi f t)\, dt \\ &= \frac{1}{c_m + i\,2\pi f} \\ |H_m(f)|^2 &= \frac{1}{c_m^2 + (2\pi f)^2} \\ |S_{Xm}(f)|^2 &= \mathrm{E}^2[X_m]\,\delta(f) + \frac{\mu_m}{c_m^2 + (2\pi f)^2}, \end{aligned} \tag{B.187}$$

by virtue of Eq. (9.27).

We now attempt to construct an approximation to a fractal shot-noise process through the sum of a number of component processes $X_m(t)$, with parameters related in a power-law fashion. Clearly, the component spectra $S_{Xm}(f)$ must cross

each other; otherwise, one would dominate over all frequencies and the trivial result $S_{XR}(f) \sim f^{-2}$ would ensue. Meaningful results thus obtain only if each component process dominates the whole over its own range of frequencies.

This occurs in the neighborhood of the crossover frequencies $f = c_m/(2\pi)$, whereupon

$$S_{XR}[c_m/(2\pi)] \approx \frac{\mu_m}{2c_m^2}. \tag{B.188}$$

Substituting Eq. (B.188) into the scaling equation $S_{XR}(f) \approx (f/f_S)^{-\alpha}$, and retaining the substitution $f = c_m/(2\pi)$, yields

$$\begin{aligned} \frac{\mu_m}{2c_m^2} &\approx \left(\frac{c_m}{2\pi f_S}\right)^{-\alpha} \\ \mu_m\, c_m^{\alpha-2} &\approx 2(2\pi f_S)^{\alpha}. \end{aligned} \tag{B.189}$$

To minimize variation about the ideal $f^{-\alpha}$ behavior of $S_{XR}(f)$, we maintain a fixed ratio between adjacent values of c_m. We therefore set

$$c_m = c_1\, a^{m-1}, \quad a > 1, \tag{B.190}$$

so that Eqs. (B.189) and (B.190) yield

$$\begin{aligned} \mu_m &= \mu_1\, b^{m-1} \\ \mu_1 &= 2(2\pi f_S)^{\alpha}\, c_1^{2-\alpha} \\ b &= a^{2-\alpha}; \end{aligned} \tag{B.191}$$

we also have $b > 1$ for $0 < \alpha < 2$.

Finally, we choose a frequency ratio a; this value for a, in combination with Eqs. (B.190) and (B.191), defines the fractal shot noise process $S_{XR}(f)$. As an example, we plot the spectrum for $\alpha = 1$, $f_S = 1$, $c_1 = 2\pi$, $a = 10$, and $M = 4$. From this, and Eq. (B.191), we obtain $\mu_1 = 2$ and $b = 0.1$, and the spectrum simplifies to

$$S_{XR}(f) = \sum_{m=1}^{M} \frac{10^{m-1}}{10^{2m-2} + f^2}. \tag{B.192}$$

Figure B.6 provides a plot of $S_{XR}(f)$ vs. f; it demonstrates a close approximation to the desired $1/f$ form. The component spectra do indeed achieve a value of precisely $1/f$ at the breakpoints, as designed; however, their overlap causes the sum to exceed $1/f$ specification by up to a factor of 1.42, or 1.5 dB. Nevertheless, over the design frequency range $10^0 \le f \le 10^3$, $f \times S_{XR}(f)$ remains constant to within ± 0.34 dB.

Prob. 9.2.1 Using Eq. (9.36) we have

$$\int_{-\infty}^{\infty} h(K,s)\, h(K, s+|t|)\, ds = \begin{cases} K - |t| & |t| < K \\ 0 & \text{otherwise.} \end{cases} \tag{B.193}$$

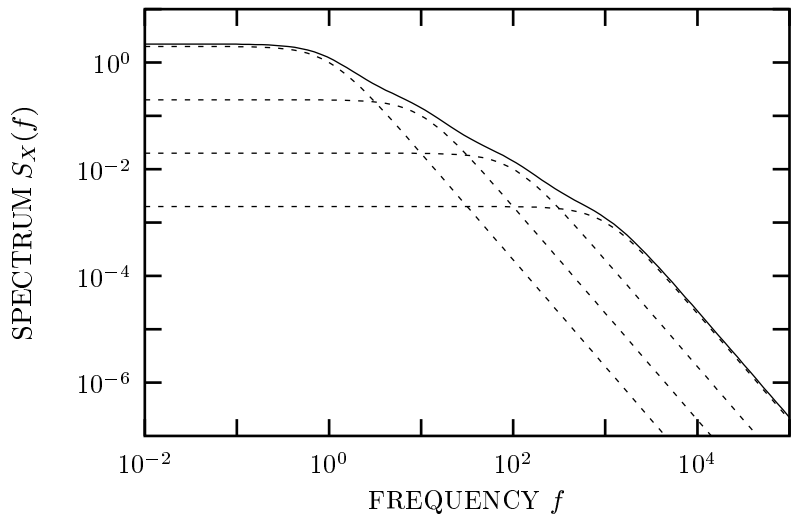

Fig. B.6 Spectrum as provided in Eq. (B.192) (solid curve). The graph also includes the four component spectra $S_{Xm}(f)$ (dashed curves).

Forming the expectation of Eq. (B.193) involves integrating the right-hand side against the probability density of K, for values of K in excess of $|t|$. We therefore have

$$R_h(t) \equiv \mathrm{E}\left[\int_{-\infty}^{\infty} h(K,s)\, h(K,s+|t|)\, ds\right] = \int_{x=|t|}^{\infty} (x-|t|)\, p_K(x)\, dx. \quad \text{(B.194)}$$

Equations (B.194) and (9.19) together yield $R_X(t)$.

Prob. 9.2.2 Solving Eq. (B.194) for the special case of Eq. (9.37) leads to

$$\begin{aligned} R_h(t) &= \int_{s=|t|}^{\infty} (s-|t|)\, p_K(s)\, ds \\ &= \int_{s=t}^{\infty} (s-t)\,(\beta-1)\, A^{\beta-1}\, s^{-\beta}\, ds \\ &= (\beta-1)\, A^{\beta-1} \left[s^{2-\beta}/(2-\beta) - t\, s^{1-\beta}/(1-\beta)\right]_t^{\infty} \\ &= (\beta-1)\, A^{\beta-1}\, t^{2-\beta} \left[(\beta-2)^{-1} - (\beta-1)^{-1}\right] \\ &= (\beta-2)^{-1}\, A^{\beta-1}\, t^{2-\beta}. \end{aligned} \quad \text{(B.195)}$$

Since we specified that $2 < \beta < 3$, the corresponding exponent for t lies in the range $-1 < 2-\beta < 0$, indicating a fractal form. Identifying this with the canonical form $t^{\alpha-1}$ for autocorrelation functions and related statistical measures provides

$$\begin{aligned} \alpha - 1 &= 2-\beta \\ \alpha &= 3-\beta, \end{aligned} \quad \text{(B.196)}$$

with α in the range $0 < \alpha < 1$.

Prob. 9.3 We begin with Eq. (9.38) and proceed by applying a monotonic transformation, and then substituting $x \equiv cm^{-D}$ and $\mathcal{M} \equiv Kt^{-\beta}$:

$$\begin{aligned} \Pr\{\mathcal{M} \geq m\} &= cm^{-D} \\ \Pr\{\mathcal{M}^{-D} \leq m^{-D}\} &= cm^{-D} \\ \Pr\left\{\left[Kt^{-\beta}\right]^{-D} \leq x/c\right\} &= x \\ \Pr\{c\,K^{-D}\,t^{\beta D} \leq x\} &= x \\ \Pr\{t \leq x\} &= x, \end{aligned} \tag{B.197}$$

where we make the identifications $\beta = 1/D$ and $K = c^{1/D}$. Equation (B.197) has the form of a random variable uniformly distributed in the unit interval.

Hence, with t a random time chosen uniformly in the unit interval, the function $Kt^{-\beta} = (t/c)^{-1/D}$ has the same probability distribution as that given in Eq. (9.38). Returning to the original specification of the problem, to obtain the total mass in a given region of space, we sum a Poisson-distributed number of these random variables. Consequently, a fractal shot-noise process with impulse response function given by Eq. (9.2), $B = 1$, and appropriate mean Poisson rate μ will have an amplitude distribution equivalent to the total mass in a cluster. For $0 < D < 1$, we have $1 < \beta < \infty$, yielding a one-sided stable distribution.

B.10 FRACTAL-SHOT-NOISE-DRIVEN POINT PROCESSES

Prob. 10.1 If two events from a fractal-shot-noise-driven Poisson process $dN_2(t)$ span a large interval, such that $\tau > B - A$, then the events must derive from different impulse response functions. Therefore, any relation between the two times must derive from the primary homogeneous Poisson process $dN_1(t)$. This process has an exponential form for the times between events, and this form propagates to $dN_2(t)$ in the absence of any other connection between the events.

Prob. 10.2 Substituting directly into Eq. (10.14), we obtain

$$\begin{aligned} F(T) &= 1 + \frac{2\mathrm{E}[K^2]}{\mathsf{a}T} \int_0^{\min(T,B-A)} (T-u) \int_A^{B-u} (t^2+ut)^{-\beta}\, dt\, du \\ &= 1 + \frac{2\mathrm{E}[K^2]}{\mathrm{E}[K]\,(B-A)\,T} \int_0^{\min(T,B-A)} (T-u) \int_A^{B-u} dt\, du \\ &= 1 + \frac{2\mathrm{E}[K^2]}{\mathrm{E}[K]\,(B-A)\,T} \int_0^{\min(T,B-A)} (T-u)\big[B-(u+A)\big]\, du \\ &= 1 + \frac{2\mathrm{E}[K^2]}{\mathrm{E}[K]\,(B-A)\,T} \left[TBu - (B+T-A)\frac{u^2}{2} + \frac{u^3}{3}\right]_0^{\min(T,B-A)}. \end{aligned} \tag{B.198}$$

We now specialize to the two cases: $T \le B - A$ and $T > B - A$. In the former, Eq. (B.198) becomes

$$\begin{aligned} F(T) &= 1 + \frac{2\mathrm{E}[K^2]}{\mathrm{E}[K]\,(B-A)\,T} \left[T^2B - (B+T-A)\frac{T^2}{2} + \frac{T^3}{3}\right] \\ &= 1 + \frac{2\mathrm{E}[K^2]}{\mathrm{E}[K]\,(B-A)\,T} \left[\frac{T^2\,(B+A)}{2} - \frac{T^3}{6}\right] \\ &= 1 + \frac{\mathrm{E}[K^2]\,T\,(B+A-T/3)}{\mathrm{E}[K]\,(B-A)}. \end{aligned} \tag{B.199}$$

Further specializing to the case $B/T \gg 1$ and $B/A \gg 1$, Eq. (B.199) simplifies to

$$\begin{aligned} F(T) &\approx 1 + \frac{\mathrm{E}[K^2]\,TB}{\mathrm{E}[K]\,B} \\ &= 1 + \frac{\mathrm{E}[K^2]}{\mathrm{E}[K]}\,T. \end{aligned} \tag{B.200}$$

For this value of β, Eq. (10.16) provides

$$\begin{aligned} F(T) &\approx 1 + \frac{\mathrm{E}[K^2]}{\mathrm{E}[K]} \frac{1-\beta}{1-2\beta}\, B^{-\beta}\, T \\ &= 1 + \frac{\mathrm{E}[K^2]}{\mathrm{E}[K]} \frac{1}{1}\, B^0\, T \end{aligned}$$

$$= 1 + \frac{\mathrm{E}[K^2]}{\mathrm{E}[K]}\,T, \tag{B.201}$$

in accordance with Eq. (B.200). Finally, for $T > B - A$, Eq. (B.198) gives rise to

$$\begin{aligned} F(T) &= 1 + \frac{2\mathrm{E}[K^2]}{\mathrm{E}[K]\,(B-A)\,T}\left[TB(B-A)\right. \\ &\qquad \left. - (B+T-A)\frac{(B-A)^2}{2} + \frac{(B-A)^3}{3}\right] \\ &= 1 + \frac{2\mathrm{E}[K^2]}{\mathrm{E}[K]\,T}\left[TB - T\,\frac{B-A}{2} - \frac{(B-A)^2}{2} + \frac{(B-A)^2}{3}\right] \\ &= 1 + \frac{\mathrm{E}[K^2]}{\mathrm{E}[K]}\left[B + A - \frac{(B-A)^2}{3T}\right]. \end{aligned} \tag{B.202}$$

Prob. 10.3 We start with Fig. 10.6, and consider a single impulse response function. The parameters include $\beta = 2$, $A = 1$, $B = 10^5$, and $\mathsf{a} = 100$, so we have

$$\begin{aligned} \mathsf{a} &\equiv \int h(t)\,dt = \int_A^B K\,t^{-\beta}\,dt \\ 100 &= K\int_1^{10^5} t^{-2}\,dt = K\left(1 - 10^{-5}\right) \\ K &\approx 100. \end{aligned} \tag{B.203}$$

The rate then follows the form $100/t^2$ for $A < t < B$. At a general time t, a typical interevent interval generated by this single impulse response function will have a duration equal to the inverse of this rate, so $\tau(t) \approx t^2/100$. By this time t, we will have generated about $N_2(t)$ intervals, where we obtain the counting process $N_2(t)$ through

$$\begin{aligned} N_2(t) &\approx \int_A^t h(s)\,ds \\ &\approx \int_1^t 100\,s^{-2}\,ds \\ &= 100\,(1 - 1/t). \end{aligned} \tag{B.204}$$

Combining this information, we can say that $N_2(t) \approx 100\,(1 - 1/t)$ intervals will lie below the limit $\tau \approx t^2/100$; eliminating t yields about

$$N_2 = 100\left[1 - \frac{1}{10\sqrt{\tau}}\right] \tag{B.205}$$

intervals less than τ. Normalizing Eq. (B.205) to unity as $\tau \to \infty$ leads to

$$\Pr\{\tau < s\} = 1 - \frac{1}{10\sqrt{s}}. \tag{B.206}$$

Finally, taking the derivative of Eq. (B.206) yields the probability density

$$p_\tau(s) = (20)^{-1}\, s^{-3/2}. \tag{B.207}$$

The argument presented above remains valid down to interevent intervals $\tau \approx 1/\left(KA^{-2}\right)$, the inverse of the maximum rate (which occurs at the onset of the impulse response function); at long interevent intervals, the times between the events of the primary point process $dN_1(t)$ dominate the interevent interval probability density, as discussed in Prob. 10.1. These limits, as well as the overall form of Eq. (B.207), are in good accord with the results displayed in Fig. 10.6. A similar argument, although with different power-law exponents, obtains for any value of $\beta > 1$; we require only that most of the area of the impulse response function reside near its onset.

Prob. 10.4.1 Equation (9.29) immediately provides a value for β. Given this value of β (or α) and the crossover frequency f_S, Eq. (10.27) links K and B. Equation (9.8), for $n = 1$, relates the average rate to the fractal-shot-noise-driven Poisson process parameters.

Prob. 10.4.2 For the specific case $\alpha = 1$ with $f_S = 1$ and fixed, deterministic K, we immediately have that $\beta = \frac{1}{2}$, whereupon Eq. (10.27) yields

$$\begin{aligned} \left(\mathrm{E}[K]/\mathrm{E}[K^2]\right)(2\pi f_S)^\alpha\, B^{\alpha/2} &= \alpha\,\Gamma^2(\alpha/2)/2 \\ (1/K)\,(2\pi)\sqrt{B} &= \left(\sqrt{\pi}\right)^2/2 \\ 4\sqrt{B} &= K. \end{aligned} \tag{B.208}$$

Turning to the cumulants of the rate and employing Eq. (B.208), Eq. (9.8) provides

$$\begin{aligned} C_1 &= \mu\mathrm{E}[K]\,\frac{B^{1-\beta} - A^{1-\beta}}{1-\beta} \\ &\approx \mu 4\sqrt{B}\,\frac{B^{1/2}}{1/2} \\ &= 8\mu B \\ C_2 &= \mu\mathrm{E}[K^2]\,\ln(B/A) \\ &= 16\mu B\,\ln(B/A) \\ C_3 &= \mu\mathrm{E}[K^3]\,\frac{A^{1-3/2} - B^{1-3/2}}{3/2-1} \\ &\approx \mu\, 64B^{3/2}\,\frac{A^{-1/2}}{1/2} \\ &= 128\mu B\sqrt{B/A}. \end{aligned} \tag{B.209}$$

Using Eq. (B.209) with Eq. (3.4) then leads to a square of the coefficient of variation of the rate given by

$$\frac{C_2}{C_1^2} = \frac{16\mu B\ln(B/A)}{(8\mu B)^2} = \frac{\ln(B/A)}{4\mu B}, \tag{B.210}$$

and a square of the skewness of the rate expressed as

$$\frac{C_3^2}{C_2^3} = \frac{\left(128\mu B\sqrt{B/A}\right)^2}{\left[16\mu B\ln(B/A)\right]^3} = \frac{4}{\mu A\left[\ln(B/A)\right]^3}. \tag{B.211}$$

For large values of the rate coefficient of variation we require small values of μB in Eq. (B.210), since the logarithm function varies so slowly. For small values of the rate skewness we require large values of μA in Eq. (B.211), again neglecting the logarithm. The conflict arises because the simultaneous specification of a small value of μB and a large value of μA leads to $A \gg B$, whereas we define $A < B$; in fact, obtaining a $1/f$ spectrum over an appreciable range of frequencies requires $B \gg A$. Thus, the rate either has a large coefficient of variation or a small skewness, but not both. Furthermore, we have not specified μ independently of A and B.

Prob. 10.4.3 Aside from $\beta = \frac{1}{2}$ which we established above, we have $A = 1/f_S = 1$, and from $B/A = 10^3$ we obtain $B = 10^3$. We also have a mean rate of unity, and Eq. (B.209) reveals that $C_1 = 8\mu B$; together this yields $\mu = (8B)^{-1} = 1/8000$. Also, Eq. (B.208) provides $K = 4\sqrt{B} = 4\sqrt{1\,000}$. In summary, we have

$$\begin{array}{rcl} \beta & = & \frac{1}{2} \\ A & = & 1 \\ B & = & 1\,000 \\ K & = & 40\sqrt{10} \\ \mu & = & 1/8000. \end{array} \tag{B.212}$$

For the coefficient of variation, we use the parameters provided in Eq. (B.212) in Eq. (B.210) to obtain

$$\frac{\sqrt{C_2}}{C_1} = \sqrt{\frac{\ln(B/A)}{4\mu B}} = \sqrt{\frac{\ln(10^3)}{8\mu B/2}} = \sqrt{6\ln(10)} \doteq 3.71692, \tag{B.213}$$

while Eq. (B.211) yields the skewness

$$\frac{C_3}{C_2^{3/2}} = \sqrt{\frac{4}{\mu A\left[\ln(B/A)\right]^3}} = \sqrt{\frac{32B/A}{8\mu B\left[\ln(10^3)\right]^3}} = \sqrt{\frac{32\,000}{\left[3\ln(10)\right]^3}} \doteq 9.85302. \tag{B.214}$$

Equation (B.212) defines a process with significant variation.

Prob. 10.5 We base our argument on the results provided in Table 9.1, which divides into two regions of interest. For $\beta \leq 1$ and $B = \infty$, the impulse response function $h(t)$ has infinite area in its tail, and the results in Sec. A.6.1 indicate that the resulting shot noise process has an infinite value at all times with probability one. Using this as a rate for a Poisson point process yields a collection of points infinitely dense at every time. We have $N_2(t+\epsilon) - N_2(t) = \infty$, with probability one, for any t and $\epsilon > 0$, even if we use the process itself or its rate to select t or ϵ. This is far from an orderly process.

For $\beta \geq 1$ and $A = 0$, the infinite area now lies near the origin. This leads to shot noise with a stable amplitude density; the corresponding point process remains well-behaved except near the onset times of the impulse response functions. Here an infinite number of events exist after each impulse response function commences. If we let t_k denote any of the events in the primary Poisson point process $dN_1(t)$ from which the shot noise derives, then we have $N_2(t_k + \epsilon) - N_2(t_k) = \infty$, with probability one, for any $\epsilon > 0$. Again, the resulting point process $dN_2(t)$ is not orderly.

Prob. 10.6.1 This description applies for $t > 0$. For $t < 0$ the electromagnetic shock wave generated by the particle has not yet reached the observation point, so that all fields remain zero and no photons are yet present there.

Prob. 10.6.2 The electric field becomes

$$\begin{aligned}
\mathbf{E} &= -\nabla\phi_L - \mathsf{c}^{-1}\,\partial\mathbf{A}_L/\partial t \\
&= -2\mathsf{q}J^2\mathsf{n}^{-2}\left[(x-\mathsf{v}t)^2 - J^2(y^2+z^2)\right]^{-3/2}\{x-\mathsf{v}t,\, y,\, z\} \\
&= 2\mathsf{q}J^2\mathsf{n}^{-2}\left[(\mathsf{v}t)^2 + 2Jd\mathsf{v}t\right]^{-3/2}\{\mathsf{v}t + Jd,\, 0,\, -d\} \\
&= 2\mathsf{q}J^2\mathsf{n}^{-2}\mathsf{v}^{-2}[t^2 + 2t_1 t]^{-3/2}\{t + t_1,\, 0,\, -d/\mathsf{v}\}\,, \qquad \text{(B.215)}
\end{aligned}$$

where we define $t_1 \equiv Jd/\mathsf{v} = d(\mathsf{n}^2\mathsf{c}^{-2} - \mathsf{v}^{-2})^{1/2}$. The magnetic field becomes

$$\begin{aligned}
\mathbf{H} &= \mathbf{B} \\
&= \nabla \otimes \mathbf{A}_L \\
&= 2\mathsf{q}\mathsf{v}\mathsf{c}^{-1}\left[(x-\mathsf{v}t)^2 - J^2(y^2+z^2)\right]^{-3/2}\left\{0,\, J^2 z,\, -J^2 y\right\} \\
&= 2\mathsf{q}d\mathsf{v}J^2\mathsf{c}^{-1}\left[(\mathsf{v}t)^2 + 2Jd\mathsf{v}t\right]^{-3/2}\{0,1,0\} \\
&= 2\mathsf{q}dJ^2\mathsf{c}^{-1}\mathsf{v}^{-2}[t^2 + 2t_1 t]^{-3/2}\{0,1,0\}\,, \qquad \text{(B.216)}
\end{aligned}$$

where $\otimes$ again denotes the vector cross product.

This leads to expressions for the Poynting vector and the photon flux density given by

$$\begin{aligned}
\mathbf{S} &\equiv (4\pi)^{-1}\mathsf{c}\,\mathbf{E}\otimes\mathbf{H} \\
&= (4\pi)^{-1}\mathsf{c}(2\mathsf{q}J^2\mathsf{n}^{-2}\mathsf{v}^{-2})(2\mathsf{q}dJ^2\mathsf{c}^{-1}\mathsf{v}^{-2})[t^2+2t_1t]^{-3} \\
&\qquad \times\{t+t_1,\,0,\,-d/\mathsf{v}\}\otimes\{0,1,0\} \\
&= \pi^{-1}\mathsf{q}^2 dJ^4\mathsf{n}^{-2}\mathsf{v}^{-4}[t^2+2t_1t]^{-3}\{d/\mathsf{v},\,0,\,t+t_1\} \qquad \text{(B.217)} \\
h(t) &\approx |\mathbf{S}|/h\mathrm{E}[\nu] \\
&= (\pi h\,\mathrm{E}[\nu])^{-1}\mathsf{q}^2 dJ^4\mathsf{n}^{-2}\mathsf{v}^{-4}\left[t^2+2t_1t\right]^{-3}\left[t^2+2t_1t+t_1^2+(d/\mathsf{v})^2\right]^{1/2} \\
&= (\pi h\mathrm{E}[\nu])^{-1}\mathsf{q}^2 dJ^4\mathsf{n}^{-2}\mathsf{v}^{-4}\left[t^2+2t_1t\right]^{-3}\left[t^2+2t_1t+(\mathsf{n}d/\mathsf{c})^2\right]^{1/2} \\
&= (\pi h\mathrm{E}[\nu])^{-1}\mathsf{q}^2 dJ^4\mathsf{n}^{-2}\mathsf{v}^{-4}\left[t^2+2t_1t\right]^{-3}\left[t^2+2t_1t+t_2^2\right]^{1/2}, \qquad \text{(B.218)}
\end{aligned}$$

where we define $t_2 \equiv \mathsf{n}d/\mathsf{c}$.

Casting this photon-flux-density time function in the form of a simple power-law impulse response function, as in Eq. (9.2), yields the following results. The photon flux density exhibits a power-law decay with a power-law exponent that increases at the crossover time $t = t_1$, and decreases at time $t = t_2$. No real medium will pass frequency components of arbitrarily high frequency, and indeed all systems have practical limits to the frequency components that appear at the output (see Sec. 2.3.1 for a discussion pertinent to this issue). The difference between the upper ν_u and lower ν_l frequency limits forms the system bandwidth, $\nu_u - \nu_l$. Similarly, the onset time of the light pulse cannot exceed a value roughly equal to the inverse of the bandwidth; we therefore define $t_0 \equiv (\nu_u - \nu_l)^{-1}$. In addition, the nonzero size of the charged particle imposes a limit on the onset time (Zrelov, 1968), although this limit proves relatively unimportant since we can assume that the wavelength of the generated photons greatly exceeds the particle size.

The photon-flux-density time function $h(t)$ thus follows the form

$$h(t) \sim \begin{cases} 0 & \text{for} \quad t < t_0 \\ t^{-3} & \qquad t_0 < t < t_1 \\ t^{-6} & \qquad t_1 < t < t_2 \\ t^{-5} & \qquad t > t_2. \end{cases} \tag{B.219}$$

Even for relatively narrow bandwidths, the onset time t_0 often remains several orders of magnitude smaller than t_1, ensuring a large range of times for which t^{-3} behavior is observed. For example, using a 150-mCi radon source, Čerenkov (1938) studied radiation from a number of liquids in the wavelength range 536 to 556 nm, which gives the onset time

$$t_0 \equiv (\nu_u - \nu_l)^{-1} = \left(\frac{3.00 \times 10^8 \,\text{m / s}}{536 \times 10^{-9} \,\text{m}} - \frac{3.00 \times 10^8 \,\text{m / s}}{556 \times 10^{-9} \,\text{m}} \right)^{-1} \approx 50 \text{ fsec.} \tag{B.220}$$

Particles traveling close to the speed of light through materials with a refractive index as low as 1.2, with d as small as 1 cm to the observation point, yield a crossover time $t_1 \approx 22$ psec, almost three orders of magnitude slower. Most media have much larger bandwidths, and correspondingly larger differences between t_0 and t_1. For such particles we can make the approximation that $h(t) = 0$ for $t < t_0$, and similarly $h(t) = 0$ for $t > t_1$, since the power-law decay exponent increases at $t = t_1$. The energy-flow time-response functions associated with a single charged particle emitting Čerenkov radiation then closely follow

$$h(t) \approx \begin{cases} Kt^{-3} & \text{for } A < t < B \\ 0 & \text{otherwise,} \end{cases} \tag{B.221}$$

where we identify $A = t_0$ and $B = t_1$.

Prob. 10.6.3 In media whose index of refraction differs only slightly from unity, the power-law crossover time t_1 of the impulse response function $h(t)$ becomes very small, possibly smaller that the onset time t_0. In that case $h(t)$ lacks the t^{-3} portion,

and instead exhibits a faster power-law decay,

$$h(t) \approx \begin{cases} Kt^{-5} & \text{for } t > t_0 \\ 0 & \text{otherwise.} \end{cases} \tag{B.222}$$

However, since the energy production is proportional to J^4, if the index of refraction differs only slightly from unity, then J assumes a small value, as does the total light energy. In that case, the charged particles generate few photons.

Prob. 10.6.4 The foregoing thus illustrates that a single particle gives rise to a photon flux density that follows a decaying power-law time function. If a number of particles travel along the x-axis, they stimulate noninterfering sets of photons, as long as these particles remain sufficiently separated so that their respective electric and magnetic fields do not overlap significantly. Since the form of the Poynting vector involves a vector multiplication, overlap means cross-products between the two sets of fields so that the resulting sequence of photons generated will not follow the simple linear superposition that results from two separately arriving charged particles. Radioactive sources, such as alpha- and beta-emitters, and particle accelerators operated at low current levels, generate Poisson time sequences of energetic charged particles with essentially identical positions and velocities. When these particles pass through a transparent medium under the conditions specified above, the point process resulting from the generated Čerenkov photon events will obey the fractal-shot-noise-driven Poisson process model.

Prob. 10.7.1 From the cluster start time, and the lack of any mechanism terminating the clusters, we have immediately $A = 2.3$ days and $B = \infty$. The average number of earthquakes per cluster is simply the area, so we also have $\mathsf{a} = 6$. With a mean of $\mathrm{E}[X] = 22$ earthquakes per year, we have a rate for the primary Poisson process given by

$$\mu = \frac{\mathrm{E}[X]}{\mathsf{a}} \approx \frac{22 \text{ yr}^{-1}}{6} \frac{1 \text{ yr}}{365 \text{ day}} \approx 0.01/\text{day}. \tag{B.223}$$

It remains to find K and β.

Postulating an impulse response function $h(t)$ of the form given in Eq. (9.2), the area remaining in the tail has the form

$$\begin{aligned} \mathsf{a} - h_t(K, 0) &\equiv \int_t^\infty h(u)\, du \\ &= \int_t^\infty K u^{-\beta}\, du \\ &= \frac{K}{\beta - 1}\, t^{1-\beta}, \end{aligned} \tag{B.224}$$

where we consider $t > A$ and make use of the fact that $B = \infty$. We will justify the assumption that $\beta > 1$ shortly. Since we know that the number of earthquakes remaining in a cluster decays as $t^{-1/4}$, we have $t^{1-\beta} = t^{-1/4}$ so that $\beta = \frac{5}{4}$, which

is indeed larger than unity, verifying our original assumption. Evaluating Eq. (B.224) at $t = A$ yields the area, which we know has a value of six earthquakes per cluster, so that

$$\begin{aligned} \mathsf{a} &= \frac{K}{\beta - 1}\, A^{1-\beta} \\ 6 &= \frac{K}{1/4}\, 2.3^{-1/4} \\ K &= 1.85. \end{aligned} \tag{B.225}$$

Prob. 10.7.2 Equation (B.224) provides the average number of events remaining in a cluster. However, an exponential transform yields the probability of zero events remaining in the cluster, much as Eq. (10.3) does for the shot-noise-driven Poisson process. If we set the probability of zero events remaining at 0.8 or greater, we then have

$$\begin{aligned} \Pr\{\text{zero events after } t\} &= \exp\big\{-\big[\mathsf{a} - h_t(K,0)\big]\big\} \\ &= \exp\left(-\frac{K}{\beta-1}\, t^{1-\beta}\right) \\ &= \exp\big[-\mathsf{a}\,(t/A)^{1-\beta}\big] \\ 0.8 &> \exp\Big[-6\,(t/2.3)^{-1/4}\Big] \\ \ln(0.8)/(-6) &> (t/2.3)^{-1/4} \\ [\ln(0.8)/(-6)]^{-4} &< t/2.3 \\ t &> 2.3\,[\ln(0.8)/(-6)\,]^{-4} \\ t &> 1\,200\,000 \text{ days} = 3\,300 \text{ years}, \end{aligned} \tag{B.226}$$

a surprisingly large number.

Prob. 10.8.1 We define $K \equiv u_0(4\pi\Delta)^{-D_{\mathrm{E}}/2}$ and $t_0 \equiv |\mathbf{x} - \mathbf{x}_0|^{\,2}/4\Delta$, and rewrite Eq. (10.38) as

$$u(\mathbf{x}, t) = K \exp(-t_0/t)\, t^{-D_{\mathrm{E}}/2}. \tag{B.227}$$

We further identify $A = t_0$ and $B = t_1$, yielding a response to a single deposit event that is essentially identical to that in Eq. (9.2), the only difference being in the nature of the lower cutoff. Fractal shot noise then describes the total concentration $u_\Sigma(\mathbf{x}, t)$ arising from the sequence of deposit events, which serves as the rate for the series of secondary events: the result is the fractal-shot-noise-driven Poisson process.

Prob. 10.8.2 The exponents $\beta = \frac{1}{2}$, 1, and $\frac{3}{2}$, corresponding to diffusion in one, two, and three dimensions, respectively, occur most often. In particular, the spectrum precisely follows a $1/f$ form for $\beta = \frac{1}{2}$; thus, diffusion in one dimension can give rise to a $1/f$-type spectrum.

Other values of β also obtain if the particles remain in a fractal set. In that case, the expression for the power-law exponent becomes $\beta = \frac{1}{2}D_s$, where D_s represents the spectral dimension of the fractal set, defined by

$$D_s \equiv 2D_{\mathrm{HB}}/(2 + D_d), \tag{B.228}$$

where D_{HB} is the Hausdorff–Besicovitch dimension and D_d is the exponent that describes the power-law variation of the diffusion constant with distance (Alexander & Orbach, 1982; Rammal & Toulouse, 1983). For percolation clusters at threshold, the spectral dimension D_s lies between 1 and 2, and approaches a limit of $\frac{4}{3}$ for an infinite-dimensional embedding space (Rammal & Toulouse, 1983).

Prob. 10.8.3 Employing stochastic values for K readily incorporates the effect of packets having various values of the initial concentration u_0, and using stochastic values of both K and A admits packets arriving at differing points $\mathbf{x}$.

Prob. 10.8.4 Despite yielding mathematically plausible fractal exponents, the parameters associated with various diffusion processes sometimes make this process unrealistic as a physical model. For example, the diffusion of neurotransmitter across a synapse might appear to provide an explanation for the fractal behavior observed in a variety of neural firing patterns (Lowen & Teich, 1990). However, synapses typically span distances that are quite small (perhaps 5 nm), so that over millisecond time scales the Gaussian form of Eq. (10.38) becomes a linear concentration gradient. Moreover, neurotransmitter transport and metabolism impose a finite lifetime on the extracellular concentration at least as short as this time scale. Thus, no plausible mechanism exists whereby diffusion can impart power-law decay to neurotransmitter concentration over time scales of seconds or longer, as would be required if this process were to underlie fractal action-potential patterns.

Prob. 10.9.1 The solution to this semiconductor recombination problem is closely related to a similar problem: molecular reactions involving two species that combine in pairs (Burlatsky, Oshanin & Ovchinnikov, 1989; Oshanin, Burlatsky & Ovchinnikov, 1989). A cursory analysis for a diffusion process suggests that the concentration of electrons and holes would decay in time as $t^{-D_{\mathrm{E}}/2}$, where D_{E} represents the (integer) dimension of the space within which the electrons and holes move. The concentration would indeed follow this form if the distributions of the two types of carriers were highly correlated. However, often the two carrier distributions are independent of each other, at least over short distances. Consider a sub-volume of the depletion region which, as a result of the variance of the Poisson distribution, happens to have an excess of electrons at $t = 0$. The holes in this section readily recombine with local electrons, but the remaining excess electrons have to diffuse out of this region before encountering any additional holes. This requires more time, slowing the annihilation process. This effect appears on all time and length scales, and results in a concentration that decays as $t^{-D_{\mathrm{E}}/4}$ rather than $t^{-D_{\mathrm{E}}/2}$. If the particle concentrations exhibit correlation over distances longer than some dependence length l_d, then the concentration decays as $t^{-D_{\mathrm{E}}/2}$ for time $t > t_1 = l_d^2/\Delta$, where Δ is again a diffusion

constant (Ovchinnikov & Zeldovich, 1978; Toussaint & Wilczek, 1983). At the creation of an electron-hole pair, there is a finite distance between the two particles, so the concentrations of electrons and holes will remain highly correlated over regions larger than an effective mean length.

Prob. 10.9.2 In the presence of drift, the distance traveled by a carrier along the direction of drift changes from $\sim t^{1/2}$ (diffusion alone) to $\sim t^1$ (with drift). Since we postulate that the electrons and holes diffuse through D_{E} dimensions, the total volume encountered increases as $t^{D_{\mathrm{E}}/2}$ with diffusion alone. The inclusion of drift changes this to $D_{\mathrm{E}}-1$ dimensions, each varying as $t^{1/2}$, and one dimension varying as t^1, for a total volume that increases as $t^{(D_{\mathrm{E}}+1)/2}$. Since the particle concentration decays as the inverse square-root of the volume encountered, it varies as $t^{-(D_{\mathrm{E}}+1)/4}$ for independent electron and hole distributions, and as $t^{-(D_{\mathrm{E}}+1)/2}$ for dependent distributions (Kang & Redner, 1984).

Prob. 10.9.3 We begin by considering the point process corresponding to the times of the electron-hole recombinations. These recombinations cause the decay in the number of electrons and holes, so the rate of recombination equals the rate of decrease in the number of particles. In the presence of drift and diffusion, the rate of recombination takes the form

$$h(t) \sim \begin{cases} 0, & t < A, \\ t^{-1-(D_{\mathrm{E}}+1)/4} & A < t < B, \\ t^{-1-(D_{\mathrm{E}}+1)/2} & t > B, \end{cases} \tag{B.229}$$

where we identify $A = x_0^2/\Delta$ and $B = x_c^2/\Delta$, where x_0 is a minimum separation for created electron-hole pairs, x_c is the maximum separation corresponding to a correlation length, and Δ is a combined effective diffusion constant. Equation (9.2) closely approximates this impulse response function, with $\beta = 1 + (D_{\mathrm{E}}+1)/4$.

Prob. 10.9.4 As indicated in the solution to Prob. 10.6.4, in many applications energetic particles impinge on the detector at discrete times corresponding to a one-dimensional Poisson point process. In these cases, the fractal-shot-noise-driven Poisson process is suitable for describing the resulting recombination process.

Prob. 10.10 Since the mean and variance of the numbers of conduction event onsets assume similar values, the homogeneous Poisson process provides the simplest explanation. In the absence of other evidence to the contrary, we rely on Occam's razor and choose this process as the point of departure. A similar argument holds for the numbers of conductance changes within a conduction event. Together, these suggest the Bartlett–Lewis point-process model. Since the spectrum varies as $1/f$, we further narrow our purview to the fractal version described in Sec. 10.6.4. In particular, we have $1/f = 1/f^{\alpha}$, so $\alpha = 1$. Equation (10.31) yields $\alpha = z + 3$ for $-3 < z < -1$, which gives rise to $z = -2$, which indeed falls within the range $-3 < z < -1$ and validates this result. With this choice of z, the process described in Sec. 10.6.4 successfully models the auxiliary process of conductance changes (Azhar & Gopala, 1992).

B.11 OPERATIONS

Prob. 11.1 Shuffling a point process yields a new process with completely independent intervals; this operation therefore essentially generates a renewal point process with the same interevent-interval distribution as the original. On the other hand, the transformation of the interevent intervals replaces the original interevent interval distribution with a new one, exponential in this case. Since shuffling does not affect the interevent-interval distribution, and interevent-interval transformation does not affect the relative ordering, the two operations do not influence each other. The same result therefore obtains regardless of which operation is carried out first. Since the resultant point process is renewal in nature, it is completely specified by its interevent-interval distribution (see Sec. 4.2). A renewal process with exponentially distributed intervals defines the homogeneous Poisson process (see Sec. 4.1). Therefore, shuffling and exponentialization, carried out in either order, leads to a homogeneous Poisson process.

Prob. 11.2.1 A monofractal process can comprise only a single fractal exponent; we thus require $\alpha_1 = \alpha_2$ for a true fractal-based point process.

Prob. 11.2.2 We immediately have $\alpha_R = \alpha_1 = \alpha_2$ and we also have $\mathrm{E}[\mu_R] = \mathrm{E}[\mu_1] + \mathrm{E}[\mu_2]$ from first principles. To determine f_{SR}, we transform Eq. (11.41) to the frequency domain and set $M = 2$ to obtain

$$\begin{aligned} S_{NR}(f) &= S_{N1}(f) + S_{N2}(f) \\ \mathrm{E}[\mu_R]\left[1 + (f/f_{SR})^{-\alpha}\right] &= \mathrm{E}[\mu_1]\left[1 + (f/f_{S1})^{-\alpha}\right] + \mathrm{E}[\mu_2]\left[1 + (f/f_{S2})^{-\alpha}\right] \\ \mathrm{E}[\mu_R]\,(f/f_{SR})^{-\alpha} &= \mathrm{E}[\mu_1]\,(f/f_{S1})^{-\alpha} + \mathrm{E}[\mu_2]\,(f/f_{S2})^{-\alpha} \\ f_{SR}^{\alpha} &= \frac{\mathrm{E}[\mu_1]\,f_{S1}^{\alpha} + \mathrm{E}[\mu_2]\,f_{S2}^{\alpha}}{\mathrm{E}[\mu_1] + \mathrm{E}[\mu_2]}. \end{aligned} \tag{B.230}$$

Equation (B.230) enables the calculation of the cutoff frequency f_{SR}.

Prob. 11.2.3 Although a true fractal-based point process can have only a single fractal exponent, small contributions representing other exponents sometimes prove undetectable in practice. Figure B.7 depicts the spectrum of two such fractal-based point processes, with $\alpha_2 = 2\alpha_1$. For $f \gg f_{S2}$, we actually have $S_{N1}(f) > S_{N2}(f)$, but since there are only small fractal fluctuations in $dN_2(t)$ at these frequencies, we can model the contribution of $dN_1(t)$ to $dN_R(t)$ as a homogeneous Poisson point process, which leads to what is effectively monofractal behavior in $dN_R(t)$.

Prob. 11.3 Table B.1 summarizes the nine possibilities. If shuffling completely destroys any fractal behavior in a point process, while transforming the interevent intervals does not alter the fractal qualities, then the ordering of the intervals must completely account for this fractal behavior. Conversely, if transforming the intervals eliminates the fractal characteristics of a process while shuffling does not, then the

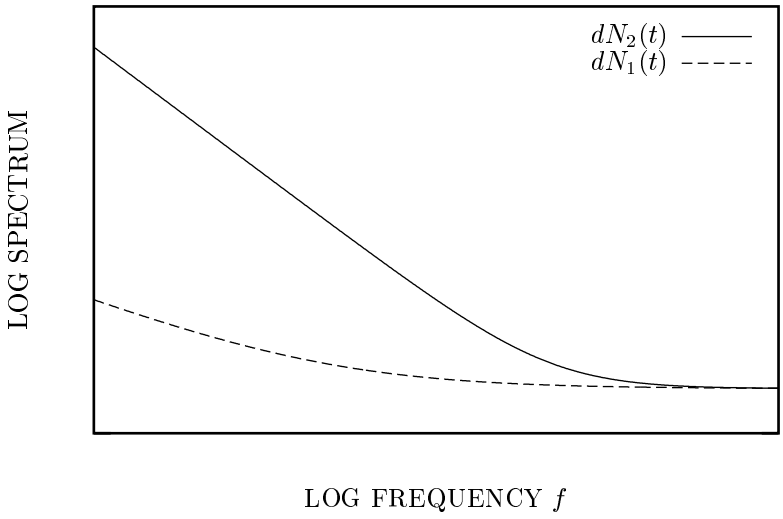

Fig. B.7 Spectrum for a superposed fractal-based point process. One of the component point processes imparts low-intensity fractal fluctuations (dashed curve), which are masked by the much larger contribution from the other process (solid curve).

		INTEREVENT-INTERVAL TRANSFORMATION		
		UNCHANGED	REDUCED	ELIMINATED
SHUFFLING	UNCHANGED	impossible	distribution dominant	distribution only
	REDUCED	ordering dominant	both important	impossible
	ELIMINATED	ordering only	impossible	impossible

Table B.1 Fractal behavior following shuffling and interval transformation.

distribution of the intervals must underlie the fractal nature of the process. If both operations decrease but do not eliminate the fractal behavior, then both effects prove important. For a monofractal process, both effects must have the same fractal exponent.

The situation is somewhat more complex when shuffling reduces the strength of the fractal fluctuations but interval transformation leaves them unchanged. The distribution of the intervals then contributes low-intensity fractal fluctuations, masked by the more robust fractal characteristics imparted by the ordering of the intervals. In this case, the two fractal contributions need not share the same fractal exponent (we considered a related scenario in Prob. 11.2.3, where the fractal behavior from one component dominated that of another). The converse holds when the results are unmodified by shuffling but reduced by interval transformation.

We conclude by considering the four possibilities that cannot occur. If shuffling completely eliminates any fractal behavior, then the interevent-interval distribution cannot play any role; similarly, if transforming the interevent intervals results in a nonfractal point process, then the ordering is irrelevant to the fractal characteristics of the process. Similarly, the two operations cannot both leave the same fractal-based point process unchanged.

Prob. 11.4 Beginning with Eq. (B.230) we have

$$\begin{aligned} f_{SR}^{\alpha} &= \frac{\mathrm{E}[\mu_1]\, f_{S1}^{\alpha} + \mathrm{E}[\mu_2]\, f_{S2}^{\alpha}}{\mathrm{E}[\mu_1] + \mathrm{E}[\mu_2]} \\ f_{SR}^{\alpha}/\,\mathrm{E}^{\alpha}[\mu_R] &= \frac{\mathrm{E}^{1+\alpha}[\mu_1]\left(f_{S1}^{\alpha}/\,\mathrm{E}^{\alpha}[\mu_1]\right) + \mathrm{E}^{1+\alpha}[\mu_2]\left(f_{S2}^{\alpha}/\,\mathrm{E}^{\alpha}[\mu_2]\right)}{\mathrm{E}^{1+\alpha}[\mu_R]} \\ c_{fR}^{\alpha} &= c_{f1}^{\alpha}\left(\frac{\mathrm{E}[\mu_1]}{\mathrm{E}[\mu_R]}\right)^{1+\alpha} + c_{f2}^{\alpha}\left(\frac{\mathrm{E}[\mu_2]}{\mathrm{E}[\mu_R]}\right)^{1+\alpha}. \end{aligned} \tag{B.231}$$

For c_{fR} to exceed both c_{f1} and c_{f2}, it must exceed the larger of c_{f1} and c_{f2}. Assume that $c_{f1} \geq c_{f2}$ without loss of generality. Suppose we keep $\mathrm{E}[\mu_1]$, $\mathrm{E}[\mu_2]$, and c_{f1} fixed. Increasing c_{f2} increases c_{fR}, so to achieve the largest ratio c_{fR}/c_{f1} we increase c_{f2} until it equals c_{f1} (further increases would cause c_{f2} to assume the role of the larger fractal content). Setting $c_{f1} = c_{f2}$ then leads to a simplification of Eq. (B.231):

$$c_{fR}^{\alpha} = c_{f1}^{\alpha}\left[\left(\frac{\mathrm{E}[\mu_1]}{\mathrm{E}[\mu_R]}\right)^{1+\alpha} + \left(\frac{\mathrm{E}[\mu_2]}{\mathrm{E}[\mu_R]}\right)^{1+\alpha}\right]$$

$$c_{fR}/c_{f1} = \left[x^{1+\alpha} + (1-x)^{1+\alpha}\right]^{1/\alpha} \tag{B.232}$$

$$x \equiv \mathrm{E}[\mu_1]/\mathrm{E}[\mu_R], \tag{B.233}$$

where x can assume any value between zero and unity. For any value of α, the right-hand side of Eq. (B.232) achieves a maximum value of unity for $x = 0$ or $x = 1$, and a minimum value of $\frac{1}{2}$ for $x = \frac{1}{2}$. We conclude that c_{fR} can never exceed either c_{f1} or c_{f2}, although it can approach either one for small rates of the other process.

Prob. 11.5.1 Since we increase the rate of $dN_1(t)$ by a factor of two, and then keep only half of the resulting events in $dN_2(t)$, the mean rate remains unchanged: $\mathrm{E}[\mu_R] = \mathrm{E}[\mu_1]$. The simple scaling operations considered do not modify the overall fractal structure of the process, so we maintain $\alpha_R = \alpha_1$.

To determine the fractal onset frequency, we begin with Eq. (5.44a), and make use of Eqs. (11.5) and (11.7), in turn, to obtain

$$\begin{aligned} S_{N1}(f) &= \mathrm{E}[\mu_1]\left[1 + (f/f_{S,1})^{-\alpha}\right] \\ S_{N2}(f) &= c^{-1}\mathrm{E}[\mu_1]\left[1 + (cf/f_{S,1})^{-\alpha}\right] \\ S_{NR}(f) &= c^{-1}\mathrm{E}[\mu_1]\left[r + r^2(cf/f_{S,1})^{-\alpha}\right] \\ &= \mathrm{E}[\mu_1]\left[1 + \left(c^{1-1/\alpha}\, f/f_{S,1}\right)^{-\alpha}\right], \end{aligned} \tag{B.234}$$

where the last step follows from the fact that $r = c$ since the mean rate remains unchanged. Comparing Eq. (B.234) with Eq. (5.44a) for $dN_R(t)$, we have

$$\begin{aligned} \mathrm{E}[\mu_1]\left[1 + \left(c^{1-1/\alpha}\, f/f_{S,1}\right)^{-\alpha}\right] &= \mathrm{E}[\mu_R]\left[1 + (f/f_{S,R})^{-\alpha}\right] \\ \left(c^{1-1/\alpha}\, f/f_{S,1}\right)^{-\alpha} &= \left(f/f_{S,R}\right)^{-\alpha} \\ c^{1-1/\alpha}\, f/f_{S,1} &= f/f_{S,R} \\ f_{S,R} &= c^{1/\alpha - 1}\, f_{S,1}. \end{aligned} \tag{B.235}$$

In general, the fractal onset frequencies for $dN_1(t)$ and $dN_R(t)$ differ; however, for $\alpha = 1$ they coincide.

Prob. 11.5.2 Independent, random deletion of a homogeneous Poisson process, case (a1), results in another homogeneous Poisson process with reduced rate. Similarly, deleting every other event in an integrate-and-reset process, case (b2), does not alter the nature of the process but halves its rate. Retaining every other event in a Poisson process, case (a2), leads to the gamma renewal process (see Prob. 4.7). And finally, randomly and independently deleting points in an integrate-and-reset process, case (b1), gives rise to geometrically distributed interevent intervals and binomial counts. This latter point process finds use in auditory neurophysiology when using low-frequency tonal stimuli, provided that measurement times are sufficiently short so that fractal behavior does not affect the results (see, for example, Teich et al., 1993).

Prob. 11.6 Consider an event of the resulting point process $dN_R(t)$. Following this event we have a fixed interval of duration τ_f, followed by an exponentially distributed random interval of mean duration τ_r, followed by yet another exponentially distributed random interval of mean duration $1/\mu_1$. The next event of $dN_R(t)$ follows immediately after this last interval. The sum of three more intervals, one fixed and two exponentially distributed, comprises the next interevent interval, and all are independent of their counterparts in the previous interevent interval. Their sum must also be independent; continuing this argument we find no dependency among the in-

terevent intervals of the output point process $dN_R(t)$, so that it belongs to the renewal family of point processes.

The mean interevent interval $\mathrm{E}[\tau]$ is the simple sum of the components associated with the homogeneous Poisson point process and the two forms of dead time

$$\mathrm{E}[\tau] = \mu_1^{-1} + \tau_f + \tau_r. \tag{B.236}$$

The inverse of this quantity yields the effective mean rate

$$\begin{aligned} \mathrm{E}[\mu_R] &= 1/\mathrm{E}[\tau] \\ &= \left(\mu_1^{-1} + \tau_f + \tau_r\right)^{-1} \\ &= \frac{\mu_1}{1 + \mu_1(\tau_f + \tau_r)}. \end{aligned} \tag{B.237}$$

The interevent-interval variance consists of the sum of the variances associated with the two stochastic components

$$\mathrm{Var}[\tau] = \mu_1^{-2} + \tau_r^2. \tag{B.238}$$

Similarly, the convolution of the contributions from the three components yields the interevent-interval probability density $p_\tau(t)$. For $t \le \tau_f$, this assumes a value of zero; for larger times we have

$$p_\tau(t) = \begin{cases} \mu_1(1-\mu_1\tau_r)^{-1}\left[e^{-\mu_1(t-\tau_f)} - e^{-(t-\tau_f)/\tau_r}\right] & \mu_1\tau_r < 1 \\ \mu_1^2(t-\tau_f)\, e^{-\mu_1(t-\tau_f)} & \mu_1\tau_r = 1 \\ \mu_1(\mu_1\tau_r - 1)^{-1}\left[e^{-(t-\tau_f)/\tau_r} - e^{-\mu_1(t-\tau_f)}\right] & \mu_1\tau_r > 1. \end{cases} \tag{B.239}$$

The product of the characteristic functions of the individual quantities yields the characteristic function of the interevent interval τ itself

$$\begin{aligned} \phi_\tau(\omega) &= e^{-i\omega\tau_f}(1 + i\omega/\mu_1)^{-1}(1 + i\omega\tau_r)^{-1} \\ &= \frac{\mu_1 e^{-i\omega\tau_f}}{(\mu_1 + i\omega)(1 + i\omega\tau_r)}. \end{aligned} \tag{B.240}$$

Finally, substituting Eq. (B.240) into Eq. (4.16) yields the spectrum of the point process; for $\tau_r = 0$ this reduces to

$$\begin{aligned} S_{NR}(f) &= \mathrm{E}^2[\mu_R]\,\delta(f) + \mathrm{E}[\mu_R]\,\mathrm{Re}\left[\frac{1 + \phi_\tau(2\pi f)}{1 - \phi_\tau(2\pi f)}\right] \\ &= \mathrm{E}^2[\mu_R]\,\delta(f) + \frac{\pi^2 \mathrm{E}[\mu_R] f^2}{\pi^2 f^2 + \pi\mu_1 f \sin(2\pi\tau_f f) + \mu_1^2 \sin^2(\pi\tau_f f)}. \end{aligned} \tag{B.241}$$

Prob. 11.7 We begin by substituting Eqs. (7.1) and (7.2) into Eq. (11.46). Making extensive use of the relations $A \ll t \ll B$ then yields

$$\mathsf{S}_{\vartheta 1}(t) = \mathrm{E}[\mu_1] \int_t^\infty (v - t)\, p_{\tau 1}(v)\, dv$$

$$\begin{aligned}
&\approx \frac{1-\gamma}{\gamma}\, A^{-\gamma}\, B^{\gamma-1}\, \gamma A^{\gamma} \int_t^B (v-t)\, v^{-(\gamma+1)}\, dv \\
&= (1-\gamma)\, B^{\gamma-1} \left[\frac{B^{1-\gamma} - t^{1-\gamma}}{1-\gamma} - t\, \frac{t^{-\gamma} - B^{-\gamma}}{\gamma} \right] \\
&= 1 - \gamma^{-1} (t/B)^{1-\gamma} + \left(\gamma^{-1} - 1\right) t/B \\
&\approx 1 - \gamma^{-1}\, (t/B)^{1-\gamma}, \qquad \text{(B.242)}
\end{aligned}$$

in accordance with Eq. (11.51).

We now make use of the relation $t \ll B$ and note that the second term in Eq. (11.51) lies much closer to zero than unity. We then employ the approximation $(1+x)^M \approx 1 + Mx$ for small x, which derives from the first two terms of the associated binomial series. This yields Eq. (11.52).

Taking the derivative of Eq. (3.12) provides

$$\begin{aligned}
p_{\vartheta}(t) &= \mathsf{S}_{\tau}(t) / \mathrm{E}[\tau] \\
dp_{\vartheta}(t)/dt &= -p_{\tau}(t) / \mathrm{E}[\tau] \\
p_{\tau}(t) &= -\mathrm{E}[\tau]\, dp_{\vartheta}(t)/dt \\
&= \mathrm{E}[\tau]\, d^2 \mathsf{S}_{\vartheta}(t)/dt^2. \qquad \text{(B.243)}
\end{aligned}$$

In the context of Eq. (11.52), Eqs. (B.243) and (7.2) lead to

$$\begin{aligned}
p_{\tau R}(t) &= \mathrm{E}[\tau]\, d^2 \mathsf{S}_{\vartheta R}(t)/dt^2 \\
p_{\tau R}(t) &\approx M^{-1}\, \frac{\gamma}{1-\gamma}\, (A/B)^{\gamma}\, B \frac{d^2}{dt^2} \left[1 - M\gamma^{-1}\, (t/B)^{1-\gamma}\right] \\
&= M^{-1}\, \frac{\gamma}{1-\gamma}\, (A/B)^{\gamma}\, B\gamma(1-\gamma)\, M\gamma^{-1}\, t^{-(1+\gamma)}\, B^{\gamma-1} \\
&= \gamma A^{\gamma} t^{-(\gamma+1)} \qquad \text{(B.244)}
\end{aligned}$$

as provided in Eq. (11.53); this indeed coincides with Eq. (7.1) over the range $A \ll t \ll B$.

Repeating this procedure for $\gamma > 1$ yields different results. Substituting Eqs. (7.1) and (7.2) for this range of γ into Eq. (11.46) yields

$$\begin{aligned}
\mathsf{S}_{\vartheta 1}(t) &= \mathrm{E}[\mu_1] \int_t^{\infty} (v-t)\, p_{\tau 1}(v)\, dv \\
&\approx (1 - 1/\gamma) A^{-1} \int_t^{\infty} (v-t) \gamma A^{\gamma}\, v^{-(\gamma+1)}\, dv \\
&= (\gamma - 1) A^{\gamma-1} \int_1^{\infty} t(x-1) t^{-\gamma} x^{-(\gamma+1)}\, dx \\
&= (\gamma - 1) A^{\gamma-1}\, t^{1-\gamma} \int_1^{\infty} \left[x^{-\gamma} - x^{-(\gamma+1)}\right] dx
\end{aligned}$$

$$
\begin{aligned}
&= (\gamma-1)A^{\gamma-1}\,t^{1-\gamma}\left(\frac{1}{\gamma-1}-\frac{1}{\gamma}\right)\\
&= \gamma^{-1}(t/A)^{1-\gamma},
\end{aligned}
\tag{B.245}
$$

where we again make use of the inequalities $A \ll t \ll B$, and substitute $x \equiv v/t$. This gives Eq. (11.54). Proceeding, we obtain

$$
\begin{aligned}
\mathsf{S}_{\vartheta R}(t) &= \left[\mathsf{S}_{\vartheta 1}(t)\right]^M\\
&= \left[\gamma^{-1}(t/A)^{1-\gamma}\right]^M\\
&= \gamma^{-M}(t/A)^{M(1-\gamma)},
\end{aligned}
\tag{B.246}
$$

in accordance with Eq. (11.55). We note that in this regime of γ, the binomial expansion does not apply, but rather a power-law form with a changed exponent emerges. Finally, substituting Eq. (B.246) into Eq. (B.243), and employing the shorthand notation $c \equiv 1 + M(\gamma-1)$, yields Eq. (11.56):

$$
\begin{aligned}
p_{\tau R}(t) &= \mathrm{E}[\tau_R]\,d^2\mathsf{S}_{\vartheta R}(t)/dt^2\\
&= M^{-1}\gamma(\gamma-1)^{-1}A\frac{d^2}{dt^2}\left[\gamma^{-M}(t/A)^{1-c}\right]\\
&= M^{-1}\gamma^{1-M}(\gamma-1)^{-1}A^c\frac{d^2}{dt^2}\,t^{1-c}\\
&= M^{-1}\gamma^{1-M}(\gamma-1)^{-1}A^c(c-1)\,ct^{-(c+1)}\\
&= c\,\gamma^{1-M}A^c\,t^{-(c+1)}.
\end{aligned}
\tag{B.247}
$$

Prob. 11.8.1 Figure B.8 presents the resulting spectrum $S_{NR}(f)$. The block shuffling operation destroys correlations at times significantly smaller than the block size $T = 100/f_S$. This effectively reduces the spectrum to the high-frequency limit for frequencies much larger than the inverse of the block size; we then have $S_{NR}(f) \approx \mathrm{E}[\mu]$ for $f \gg 1/T = f_S/100$. However, correlations at times much larger than T remain essentially unchanged, so that $S_{NR}(f) \approx S_{N1}(f)$ for $f \ll 1/T$. In the transition region $f \approx 1/T$, the abrupt cutoff of the blocks leads to oscillations in the frequency domain. More precisely, the Fourier transform of a rectangular block of duration $1/T$ yields a sinc$(\cdot)$ function $\sin(\pi fT)/(\pi fT)$; its square modulates the spectrum. The overall form, verified by simulation, then becomes

$$
S_{NR}(f) \approx \mathrm{E}[\mu]\left\{1 + \left[\frac{\sin(\pi fT)}{\pi fT}\right]^2 (f/f_S)^{-\alpha}\right\}. \tag{B.248}
$$

Prob. 11.8.2 Figure B.9 presents the resulting spectrum $S_{NR}(f)$. As with block shuffling, the displacement operation destroys correlations at times significantly smaller than the block size $T = 100/f_S$, so we again have $S_{NR}(f) \approx \mathrm{E}[\mu]$ for

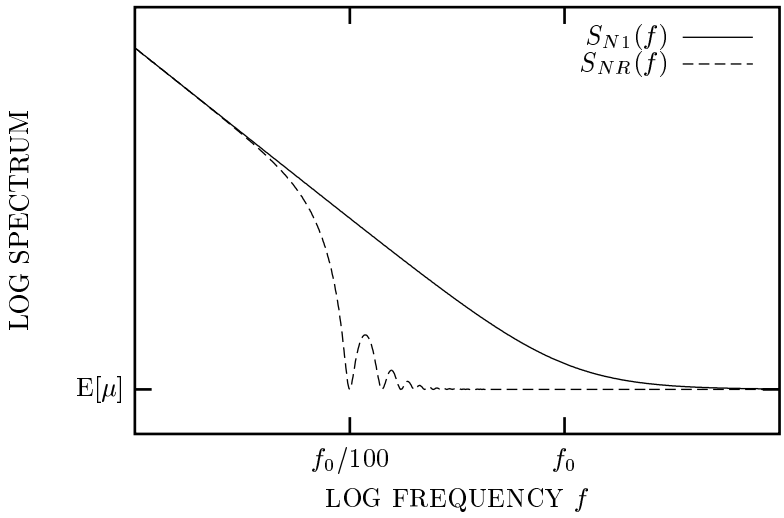

Fig. B.8 Spectrum for a fractal-rate point process $dN_1(t)$ that follows the form of Eq. (5.44a) (solid curve). Block shuffling with a block size $T = 100/f_S$ yields a point process $dN_R(t)$ with a spectrum reduced at frequencies above $1/T$, as provided in Eq. (B.248) (dashed curve).

$f \gg 1/T = f_S/100$. Also, as before, the slow components remain unchanged so that $S_{NR}(f) \approx S_{N1}(f)$ for $f \ll 1/T$. The transition region exhibits different behavior from that engendered by block shuffling. Focusing on the rate, the displacement closely resembles a noncausal filter of unit area, centered on $t = 0$, with a Gaussian shape and a standard deviation σ given by $100/f_S$ in this case.[3] In the spirit of Eq. (9.35), we then have

$$\begin{aligned} h(t) &= \frac{1}{\sqrt{2\pi}\,\sigma}\,\exp\left(-\frac{t^2}{2\sigma^2}\right) \\ H(2\pi f) &= \int_{-\infty}^{\infty} \frac{1}{\sqrt{2\pi}\,\sigma}\,\exp\left(-\frac{t^2}{2\sigma^2}\right)\exp(-i2\pi f t)\,dt \\ &= \frac{1}{\sqrt{\pi}}\int_{-\infty}^{\infty}\exp\left[-\left(\frac{t}{\sqrt{2}\,\sigma}+\frac{i2\pi\sigma f}{\sqrt{2}}\right)^2\right] \\ &\qquad \times \exp\left[-\frac{(2\pi\sigma f)^2}{2}\right]\frac{dt}{\sqrt{2}\,\sigma} \end{aligned}$$

[3] We absorb the factor $\mathrm{E}[\tau]$ into σ to simplify the notation instead of presenting it explicitly, as in Eq. (11.38).

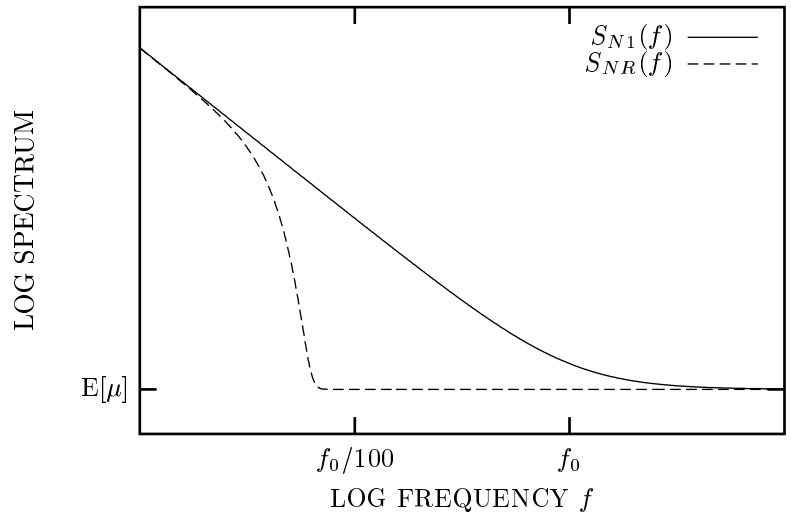

Fig. B.9 Spectrum for a fractal-rate point process $dN_1(t)$ that follows the form of Eq. (5.44a) (solid curve). Event-time displacement with a standard deviation of $T = 100/f_S$ yields a point process $dN_R(t)$ with a spectrum reduced at frequencies above $1/T$, as provided in Eq. (B.250) (dashed curve).

$$\begin{aligned} &= \exp\left[-\frac{(2\pi\sigma f)^2}{2}\right] \frac{1}{\sqrt{\pi}} \int_{-\infty}^{\infty} \exp(-u^2)\, du \\ &= \exp\left[-\frac{(2\pi\sigma f)^2}{2}\right] \\ |H(2\pi f)|^2 &= \exp\Big[-(2\pi\sigma f)^2\Big]. \end{aligned} \tag{B.249}$$

The overall form, verified by simulation, then becomes

$$S_{NR}(f) \approx \mathrm{E}[\mu]\left\{1 + \exp\big[-(2\pi\sigma f)^2\big](f/f_S)^{-\alpha}\right\}. \tag{B.250}$$

Prob. 11.9.1 The original process $dN_1(t)$ has independent intervals. Since we postulate an independent deletion operation, the interval following an event that survives the deletion remains independent of previous intervals. This defines a renewal point process.

Prob. 11.9.2 We condition on the number of deleted events between each adjacent surviving pair of events in $dN_R(t)$. Given no deletion, we have a probability density $p_{\tau 1}(t)$; this happens with probability r. For one deletion, we have $p_{\tau 1} \star p_{\tau 1}(t)$, where

$\star$ represents the convolution operation, and we expect this to occur with probability $r(1-r)$. Summing over all possibilities, we have

$$\begin{aligned} p_{\tau R}(t) &= rp_{\tau 1}(t) + r(1-r)p_{\tau 1}^{\star 2}(t) + r(1-r)^2 p_{\tau 1}^{\star 3}(t)\ldots \\ &= r\sum_{n=1}^{\infty}(1-r)^{n-1}p_{\tau 1}^{\star n}(t), \end{aligned} \tag{B.251}$$

where $p_{\tau 1}^{\star n}(t)$ denotes the n-fold convolution of $p_{\tau 1}(t)$ with itself.

Prob. 11.9.3 Taking the Fourier transform of Eq. (B.251) yields a related equation for the characteristic function

$$\begin{aligned} \phi_{\tau R}(\omega) &= r\sum_{n=1}^{\infty}(1-r)^{n-1}\phi_{\tau 1}^{n}(\omega) \\ &= \frac{r\phi_{\tau 1}(\omega)}{1-(1-r)\,\phi_{\tau 1}(\omega)}\,. \end{aligned} \tag{B.252}$$

For the specific case of a fractal renewal point process with $0 < \gamma < 1$, Eq. (7.4) yields

$$\begin{aligned} 1-\phi_{\tau R}(\omega) &= 1-\frac{r\phi_{\tau 1}(\omega)}{1-(1-r)\,\phi_{\tau 1}(\omega)} \\ &= \frac{1-\phi_{\tau 1}(\omega)}{(1-r)\,[1-\phi_{\tau 1}(\omega)]+r} \\ &\approx \frac{\Gamma(1-\gamma)\,(i\omega A)^{\gamma}}{(1-r)\,\Gamma(1-\gamma)\,(i\omega A)^{\gamma}+r} \\ &\approx r^{-1}\Gamma(1-\gamma)\,(i\omega A)^{\gamma}\,, \end{aligned} \tag{B.253}$$

where the last line results from the condition $\omega \ll A^{-1}$. Equation (B.253) differs from Eq. (7.4) only by a factor r^{-1}; thus, over the range $B^{-1} \ll \omega \ll A^{-1}$, corresponding to $A \ll t \ll B$, the randomly deleted process resembles the original process with A replaced by $r^{-1/\gamma}A$.

For $\gamma \geq 1$, the results provided in Eq. (B.253) are not valid, and in fact the probability densities $p_{\tau 1}^{\star n}(t)$ assume different shapes for different values of n. This leads to a process $dN_R(t)$ that does not have well-defined scaling regions: the process is, in general, nonfractal, except for $r \approx 0$ in which case $dN_R(t) \approx dN_1(t)$. The change in behavior at $\gamma = 1$ parallels the results presented at the end of Sec. 11.6.2 for the superposition of fractal renewal processes.

Prob. 11.10.1 Figure B.10a) is a simulation for various values of the dead-time parameter $\mu_1\tau_e$. The mean of the initial Poisson counting distribution ($\mu_1\tau_e = 0$) is $\mu_1 T = 15$. Increasing the dead time results in a decrease of both the mean and variance. The count mean decreases with dead time according to $\mathrm{E}[\mu_R]\,T = \mu_1 T/(1+\mu_1\tau_e)$, while the variance decreases more rapidly by virtue of the cube in the denominator of $\mathrm{Var}[n] \approx \mu_1 T/(1+\mu_1\tau_e)^3$.

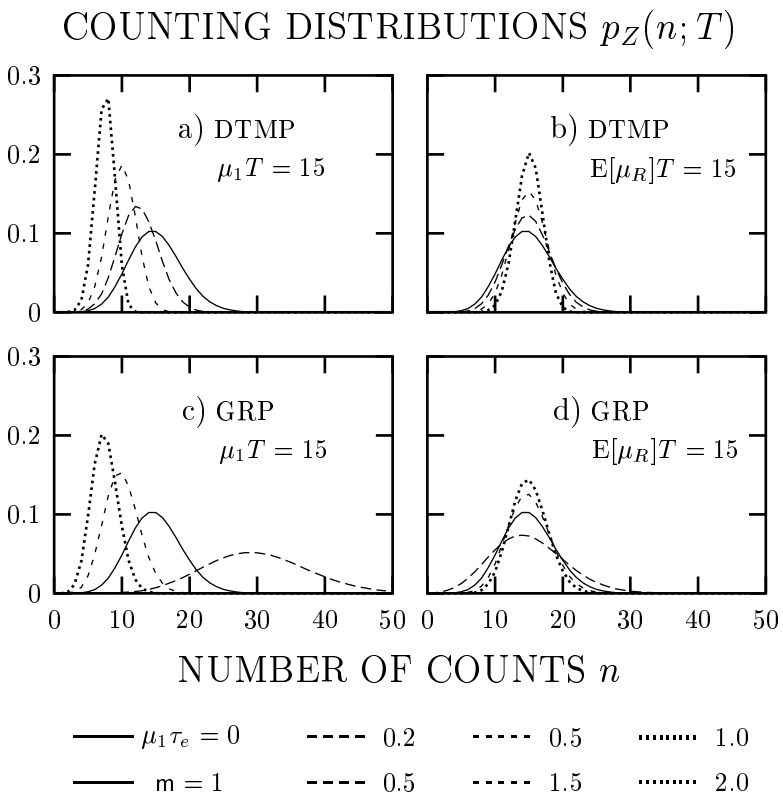

Fig. B.10 (a) Simulated dead-time-modified Poisson (DTMP) counting distributions with $\mu_1 T = 15$ and different dead-time parameters: $\mu_1\tau_e = 0$ (solid curve, Poisson distribution), 0.2 (long-dash curve), 0.5 (short-dash curve), and 1.0 (dotted curve). The count mean and variance both decrease as the dead-time parameter increases, but at different rates. (b) Same as a) but with $\mu_1 T$ adjusted to compensate for the dead-time loss such that all dead-time modified counting distributions have the same final mean, $\mathrm{E}[\mu_R]\,T = 15$. The counting distributions become narrower as the dead time increases. (c) Simulated gamma-renewal-process (GRP) counting distributions with $\mathsf{m} = 1$ (solid curve, Poisson distribution), 0.5 (long-dash curve), 1.5 (short-dash curve), and 2.0 (dotted curve). The counting distribution is broader than the Poisson for $\mathsf{m} < 1$ and narrower for $\mathsf{m} > 1$. (d) Same as c) but with $\mu_1 T$ adjusted to compensate for the decimation so that all counting distributions have the same final mean, $\mathrm{E}[\mu_R]\,T = 15$. All distributions are simulated using 10^8 intervals. Adapted from Fig. 3 of Teich & Vannucci (1978) and Fig. 14 of Teich et al. (1984).

Prob. 11.10.2 We illustrate dead-time-modified Poisson counting distributions with a final mean $\mathrm{E}[\mu_R]\,T = 15$ in Fig. B.10b). The relative width clearly narrows as the dead-time parameter becomes larger, as a consequence of the increasing regularity of the event occurrences.

Prob. 11.10.3 Given that the two processes have the same initial mean rate, dead time is more effective in decreasing the mean and variance for the fractal-rate process. This occurs because the increased event clustering engendered by the rate modulation causes more events to be lost in each dead-time period.

Prob. 11.10.4 We present simulated counting distributions for the gamma renewal process in Fig. B.10c) for various values of the order parameter m. Again, the mean of the initial Poisson counting distribution ($\mathsf{m} = 1$) is $\mu_1 T = 15$. Increasing the order parameter yields a decrease in both the count mean and variance. An order parameter that is less than unity results in an increase of both the mean and variance. The count mean varies with the order parameter in accordance with $\mathrm{E}[\mu_R]\, T = \mu_1 T/\mathsf{m}$ while the variance changes more rapidly by virtue of the square in the denominator of $\mathrm{Var}[n] \approx \mu_1 T/\mathsf{m}^2$.

Prob. 11.10.5 Simulated decimated-Poisson counting distributions with a final mean $\mathrm{E}[\mu_R]\, T = 15$ appear in Fig. B.10d). The relative width clearly narrows as m becomes larger, corresponding to the increasing regularity of the event occurrences. Values of $\mathsf{m} < 1$ yield distributions broader than the Poisson by virtue of the increased clustering in the process.

Prob. 11.11 Although fractal fluctuations are present in the original point process, the small value of the coefficient of variation ($C_{\tau 1} \doteq 0.176$) dictates that even large variations in the rate result in rather modest changes in the numbers of counts. Since exponentialization imparts a coefficient of variation of unity to the process, it effectively amplifies the fractal character of the resulting process by the ratio of the interval variances, namely $(C_{\tau R}/C_{\tau 1})^2 = (1/C_{\tau 1})^2 \doteq 32.2$.

Prob. 11.12.1 Little information can be drawn from Fig. 11.16 since: (1) the shuffled surrogate, by construction, yields a curve identical to that for the original data; and (2) the exponentialized surrogate, by construction, yields an exponential interevent-interval histogram. Knowledge of the estimated interevent-interval histogram alone is thus of little help in identifying the underlying point process.

Prob. 11.12.2 All three curves in Fig. 11.17 differ. The power-law growth of the normalized Haar-wavelet variance for the original data, with increasing counting time, signals the likely presence of fractal behavior of some form in the point process. The exponentialized version of the data has similar fractal content although it *appears* to have an increased fractal onset time and a wavelet variance that is slightly reduced in magnitude. Taken together, these observations might suggest that we can ascribe at least a portion of the fractal behavior to the ordering of the intervals.

The normalized Haar-wavelet variance for the shuffled data increases a bit and then saturates at a value of $\widehat{A}(T) \approx 2$ [the results are similar to those for the cat striate cortex cell displayed in Fig. 11.14 and discussed by Teich et al. (1996, Fig. 2); this cell also has a quite low firing rate]. Behavior of this kind can arise from a nonfractal renewal process model such as the gamma (see Prob. 4.7 in the range $0 \leq \mathsf{m} \leq 1$) or by a nonfractal cluster point process with slight clustering (see Sec. 4.5). So in view

of the behavior of the shuffled data, it appears that very little, if any, of the fractal behavior in the original point process does derive from the form of the underlying interevent-interval density.

The apparent reduction of the fractal content of the exponentialized data is therefore simply a manifestation of removing the (essentially nonfractal) features of the interevent-interval density inherent in the original data. Since shuffling completely destroys the fractal behavior whereas exponentialization does not change the fractal qualities for this data set, we conclude that the ordering of the intervals is solely responsible for the fractal behavior.

These observations reinforce earlier caveats about attempting to infer the nature of a fractal-based point process from a single measure. Indeed, neural spike trains recorded from many loci, in many preparations, exhibit power-law interevent intervals similar to those seen in the solid curve of Fig. 11.16 (see, for example, Gerstein & Mandelbrot, 1964; Wise, 1981). Such data are often coopted to conclude that fractal renewal processes provide useful models for these action-potential sequences, but the interneuron example at hand makes it clear that drawing such conclusions requires caution.

Prob. 11.12.3 Adding the two curves results in something quite close to the curve for the original data. Indeed, for short counting times the correspondence is almost exact. This indicates that the surrogate data sets perform as designed; namely, they separate out two aspects of point-process behavior: fluctuations associated with the interval distribution and fluctuations associated with the interval ordering.

Prob. 11.12.4 It is not straightforward to make a definitive choice based on the limited number of measures studied. Considering the underlying neurophysiology of the preparation provides guidance in setting forth the options. A neurophysiologically plausible point process that generates sample functions that accord with the data is a nonfractal cluster process driven by fractal-rate fluctuations (Teich et al., 1997). A natural choice for the fractal-rate fluctuations is fractal binomial noise (Thurner et al., 1997), which, as discussed in Sec. 8.4, converges to the fractal Gaussian process. An alternative choice is a gamma-based fractal doubly stochastic Poisson process, such as the fractal-binomial-noise-driven gamma process mentioned in Sec. 8.4; however, this model is less appealing from a neurophysiological perspective (Teich et al., 1997). The behavior of the shuffled version of the data in Fig. 11.17 supports either interpretation. *A priori* information clearly plays an important role in point-process identification.

Prob. 11.12.5 The generalized-dimension scaling functions presented in Fig. 11.18 reveal that the INTERNEURON action-potential sequence is not a fractal point process. Given its fractal characteristics, it must belong to the family of fractal-rate point processes (see Sec. 3.5.4 and Prob. 5.5). This accords with the supposition set forth in Prob. 11.12.4.

B.12 ANALYSIS AND ESTIMATION

Prob. 12.1 We can understand the forms of the interevent-interval densities that characterize these processes by viewing them as modulated versions of the basic exponential form provided in Eq. (4.3), which, of course, applies exactly for a Poisson process driven by a fixed, deterministic rate (yielding the homogeneous Poisson process in that case). Modulating the rate in effect modulates the mean value of the exponential density. If the rate modulation is slow in comparison with the mean rate of events, and is sufficiently weak so that its coefficient of variation obeys $C_\mu \ll 1$, then the interval density remains essentially exponential, as provided in Eq. (4.33). However, for larger values of C_μ, perceptible broadening of the interval density can occur via Eq. (4.32). Since, by assumption, rate processes (2) and (3) do not differ substantially from rate process (1), the overall forms of the interevent-interval densities for all three processes should not differ greatly from each other.

In fact, distinguishing among these three processes proves nearly impossible without recourse to an extraordinarily long record. In Fig. 10.6 for the fractal-shot-noise-driven Poisson process, for example, the interevent-interval density for $\beta = \frac{1}{2}$, corresponding to $\alpha = 1$, deviates from the equivalent result for the fractal-Gaussian-process-driven Poisson process (not shown) only for about one interval in 10^8 [we do not consider the other two curves displayed in Fig. 10.6 since they do not yield spectra that follow the form of Eq. (5.44a)]. An exception to this general similarity occurs for shot-noise rates with large K and small A. The shot-noise rate then takes on relatively large values immediately following the onset of each impulse response function. This local augmentation of the rate, in turn, can lead to a significant increase in the proportion of small intervals, while leaving the remainder of the interval density essentially intact.[4] The results in Fig. 10.6 correspond to relatively small values of K, so that no such increase for small interevent intervals is apparent.

The nature of the rate process is far more accessible if the kernel has an integrate-and-reset form. In this case, a rate comprising fractal binomial noise generates a piecewise-periodic point process between transition times of the component alternating fractal renewal processes, if significant numbers of events occur between these transitions. A histogram of the interevent intervals would readily reveal this feature, thereby distinguishing a fractal-binomial-noise-driven integrate-and-reset process from its shot-noise and Gaussian-process brethren. Although histograms of the interevent intervals for these two latter processes may resemble each other, the point process deriving from fractal shot noise will exhibit steadily increasing intervals except at the onset times of the impulse response functions. The result for the fractal Gaussian process, in contrast, will exhibit as many increases as decreases and therefore lack this asymmetry.[5]

[4] Examples of this appear in Lowen et al. (2001, Figs. 3B and 4B on pp. 385 and 387, respectively) for fractal-rate visual-system action potentials. For nonfractal cathodoluminescence photon emissions, examples appear in Saleh & Teich (1982, Figs. 10 and 14 on pp. 236 and 239, respectively).

[5] Examples of the latter case, for the human-heartbeat point process, appear in Turcott & Teich (1993, Fig. 3 on p. 26) and in Turcott & Teich (1996, Fig. 3 on p. 278).

Prob. 12.2 Given additional *a priori* information about a process, we can fit increasingly more explicit and accurate functional forms to the various estimators we employ, such as the periodogram or the estimated normalized Haar-wavelet variance. If, for example, we knew that we had a fractal renewal process at hand, with an interevent-interval density given by Eq. (7.1) and $1 \leq \gamma \leq 2$, we could fit a suitable functional form to the periodogram or even use maximum-likelihood methods. We would know to expect oscillations in the periodogram resulting from the abrupt cutoff in the probability density, among other features (see Fig. 7.2). But this increase in accuracy comes at the expense of robustness. Such specificity would prove disastrous were we to encounter instead a point process that differs greatly from the prescribed form. A fractal-shot-noise-driven Poisson process, for example, has a periodogram with significantly different detailed structure (see Fig. 10.8), and the fractal renewal assumptions would lead to spurious estimates of α. Indeed, we already encountered just such a conundrum in examining the action-potential statistics generated by an insect visual-system interneuron (see Probs. 7.8 and 11.12).

Prob. 12.3 Computing the correlation coefficient between the absolute values in columns three and four of Table 12.1 yields $\rho = -0.620$, which is less than zero and therefore does indeed indicate a bias/variance tradeoff. However, carrying out this calculation using the entries in columns six and seven yields $\rho = +0.954$, in apparent contradiction to the bias/variance tradeoff hypothesis. Why might this arise?

Examining the entries in the latter two columns reveals that a positive bias appears only for the shortest time scales; on the other hand, the largest negative bias occurs at the largest time scales. The decrease in the magnitude of the bias as the time range increases results from a partial cancelation of the positive and negative bias values. The decreased standard deviation results from the larger numbers of normalized Haar-wavelet variance values over which we calculate the fractal-exponent estimate. Since these two sources of error vary together, we expect a positive correlation coefficient. In this case, we have substantially eliminated the bias by subtracting unity from the normalized Haar-wavelet variance so that we can fully utilize the entire range of time scales. The bias/variance tradeoff therefore does not apply.

Let us examine the variation in the bias a bit more carefully. Since the magnitude of the bias in column six lies well below the standard deviation in column seven, we might be tempted to attribute the entries in column six to random fluctuations about a true bias of zero; indeed, this would generate a positive correlation coefficient. However, this is not a likely explanation for the large positive value of ρ. The standard error (the standard deviation of the mean estimate) equals the standard deviation divided by the square root of the number of simulations; the bias exceeds this value in all cases, and in fact it exceeds it by a factor of 2.3 in most of the cases. This explanation might still have merit were the distribution of the estimated values of α to deviate significantly from Gaussian form, but, in fact, estimates of the skewness and kurtosis (not shown) confirm a Gaussian distribution. Hence, it is not likely that random Gaussian fluctuations about a true bias of zero provides an explanation for the values of the bias displayed in column six. Other, subtle effects offer a more cogent explanation, as discussed in Sec. 12.2.3.

Prob. 12.4 Given a finite data set, we find an estimate of the coincidence rate by assembling a list of all possible pairs of events (regardless of the presence or absence of intervening events), and note the delay times between each pair. We can say that a coincidence has occurred at each of these delay times, but we have no information about other delay times that might also represent coincidences; only those delay times that happened to occur in our data appear in the final result. Because of the sparseness of this statistics, the delay times almost surely do not include any particular time we choose *a priori*, and so we estimate $G(t) = 0$ for any delay time specified before collecting the data. To make use of this statistic we must average over time windows. Although other averaging methods exist, a rectangular filter of unit height and constant duration T seems most convenient. Applying this filter to a point process yields the sequence of counts $Z(k, T)$, and the filtered coincidence rate then becomes the count-based autocorrelation $R_Z(k, T)$. Section 12.3.1 addresses this issue.

This problem does not afflict the point-process spectrum. We can readily carry out the Fourier transform of the point process, take the absolute magnitude, square it, and divide by the duration of the data set to estimate it, as indicated in Sec. 3.5.2:

$$\begin{aligned}
\widetilde{N}(f) &\equiv \int_0^L e^{-i2\pi ft}\, dN(t) \\
&= \int_0^L e^{-i2\pi ft} \sum_k \delta(t - t_k)\, dt \\
&= \sum_k e^{-i2\pi ft_k} \\
\left|\widetilde{N}(f)\right|^2 &= \left|\sum_k e^{-i2\pi ft_k}\right|^2 \\
\widehat{S}_N(f) &= \frac{1}{L}\left|\sum_k e^{-i2\pi ft_k}\right|^2 . \qquad \text{(B.254)}
\end{aligned}$$

Equation (B.254) does indeed provide an accurate estimate of the point-process spectrum, without the bias inherent in using the rate-based periodogram [see Eq. (3.67)]. However, as noted in Sec. 3.5.2, the estimate set forth in Eq. (B.254) suffers from a major drawback: the times $\{t_k\}$ span a continuous range of values, which precludes use of the fast Fourier transform algorithm. For a large data set this method can take several orders of magnitude longer to compute than the rate-based periodogram, with little advantage in accuracy. We therefore generally compute the rate spectrum (see Sec. 12.3.9).

Prob. 12.5.1 From Eq. (12.6) we have

$$\begin{aligned}
F(T) &\approx (T/T_F)^\alpha \left[1 - (T/L)^{1-\alpha}\right] \\
&= T_F^{-\alpha}\, T^\alpha - T_F^{-\alpha}\, L^{\alpha-1}\, T \\
\frac{dF(T)}{dT} &= \alpha T_F^{-\alpha}\, T^{\alpha-1} - T_F^{-\alpha}\, L^{\alpha-1} \quad = \quad 0
\end{aligned}$$

$$\begin{aligned} 0 &= \alpha T^{\alpha-1} - L^{\alpha-1} \\ T &= \alpha^{1/(1-\alpha)} L, \end{aligned} \tag{B.255}$$

which is independent of the fractal onset time T_F.

Prob. 12.5.2 For convenience, we employ the same simulation as that used throughout Chapter 12 (see Sec. 12.2.3), effectively extending Fig. 12.2 to larger counting times. Since estimating a variance requires at least two values, we must have $M \equiv \text{int}(L/T) \geq 2$, which, in turn, implies that $T \leq L/2$. To highlight the differences between the predictions provided by Eqs. (5.44b) and (12.6), we present the results in the form of a doubly linear plot. As shown in Fig. B.11, the simulations lie far from Eq. (5.44b). Although they roughly follow the form of Eq. (12.6), they consistently lie above this prediction, suggesting that Eq. (12.6) slightly overestimates the bias.

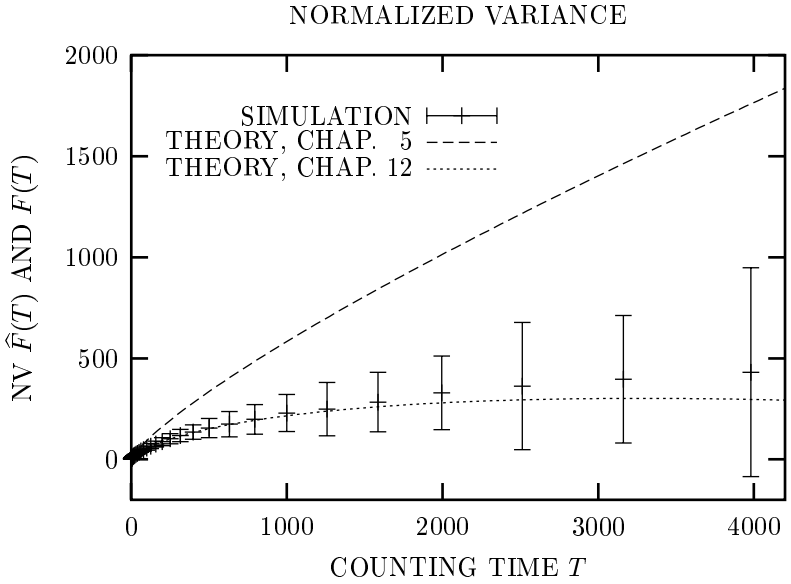

Fig. B.11 Two theoretical results for the normalized variance $F(T)$ vs. counting time T, along with an estimate of this quantity, $\widehat{F}(T)$, based on the same simulations as used to generate Figs. 12.1–12.7 and 12.9. We present the mean $\pm$ standard deviation of the simulated results (short horizontal lines $\pm$ error brackets), as well as the predicted theoretical curves from Chapter 5 [Eq. (5.44b), dashed curve] and from Chapter 12 [Eq. (12.6), dotted curve]. The simulations closely follow the latter result, but they consistently lie just above it.

Prob. 12.6 Our principal concern has heretofore been the accurate estimation of the fractal exponent α from the periodogram (spectrum estimate), rather than the estimation of the spectrum itself. Averaging adjacent computed values of the periodogram does indeed lead to spectral estimates with reduced variance. However, this comes at

the cost of fewer spectral values so that the net variance does not change. But, since the averaged values derive from different frequencies, which have different expected values, the averaging process introduces bias. Although this bias is small at high frequencies, where adjacent values differ by small relative amounts, the averaging procedure strongly affects the results at low frequencies where the spectrum changes quickly with frequency. Since the averaging process introduces bias without reducing the variance, we decline to make use of it.

A similar argument applies for block averaging of the periodogram. Fourier transforming a block yields fewer values than does transforming the entire data record. Although the averaging then occurs across transforms at identical frequencies, which eliminates the bias problem, the division of the data into blocks precludes estimating components at frequencies that lie below the inverse of the block duration. Averaging again results in fewer values with proportionately reduced variance, but it destroys important information at the longest time scales. With the net variance unchanged, and a portion of the spectrum rendered unavailable, this method does not prove helpful in fractal-exponent estimation. Indeed, as a general rule, parametric-estimation practice eschews smoothing of any kind before parameter estimation.

Prob. 12.7 We focus on the spectrum, as estimated by the periodogram, although the following argument applies to any measure with an asymptote. A real data set has finite length so that the periodogram constructed from it exhibits random fluctuations. These fluctuations, an inherent part of constructing the estimator, depend on all features of the spectrum at any given frequency, not only on the fractal component. The fluctuations can thus remain significant even when the fractal component becomes small. In particular, near the high-frequency/short-time limit, the contribution from fluctuations can readily exceed that from the fractal component. Subtracting the asymptote from the estimated value might then give rise to a negative value for the adjusted periodogram at that frequency; computation of the logarithm then cannot proceed without a modification such as that used in Sec. 12.3.9. Even so, at high frequencies little usable information pertaining to the fractal content of the spectrum resides in its estimate.

Another potential problem with subtracting the high-frequency/short-time limit arises in connection with the intrinsic nature of certain types of point processes. Even without random effects in the periodogram, point processes often have intermediate-frequency effects (such as dead time) that cause the spectrum, over some range of frequencies, to lie below the high-frequency limit (see Fig. 5.1, particularly the curve labeled HEARTBEAT). Subtracting the high-frequency asymptote then leads to negative values in the periodogram, and thence to the absence of usable information over that range. The averaging methods employed in Sec. 12.3.9 do not render these spectral values useful, since they lie well below the high-frequency asymptote for an extended range of frequencies. The simulations used to generate Tables 12.1–12.10 had no dead time or other intermediate-frequency effects, by construction, so that this issue did not arise. We reiterate our caution in employing *a priori* information such as this when estimating an unknown process.

This issue also arises in connection with the normalized Haar-wavelet variance, as shown in Fig. 5.2 (see also Fig. 7.5 and Fig. B.13 in Prob. 12.8).

Prob. 12.8 Figures B.12 and B.13 present results for the periodogram (rate spectrum estimate) and normalized Haar-wavelet variance estimate, respectively, for the simulated fractal renewal process (FRP) and homogeneous Poisson process (HPP). For the fractal renewal point process, both of these count-based measures clearly reveal power-law variation over a large range of frequency and time, indicating fractal behavior. For the homogeneous Poisson process, both show no significant variation with frequency and time, indicating a nonfractal process. For both processes, therefore, the two measures reliably describe the presence or absence of fractal characteristics in the point process under study.

The dip in the normalized Haar-wavelet variance that occurs for the fractal renewal process in Fig. B.13 arises from the abrupt cutoff of small intervals in the interevent-interval density. This cutoff is equivalent to dead time in the underlying point process (Fig. 5.2 reveals how widespread behavior of this kind is for real data). The presence of this dip vividly illustrates one of the difficulties associated with subtracting asymptotic

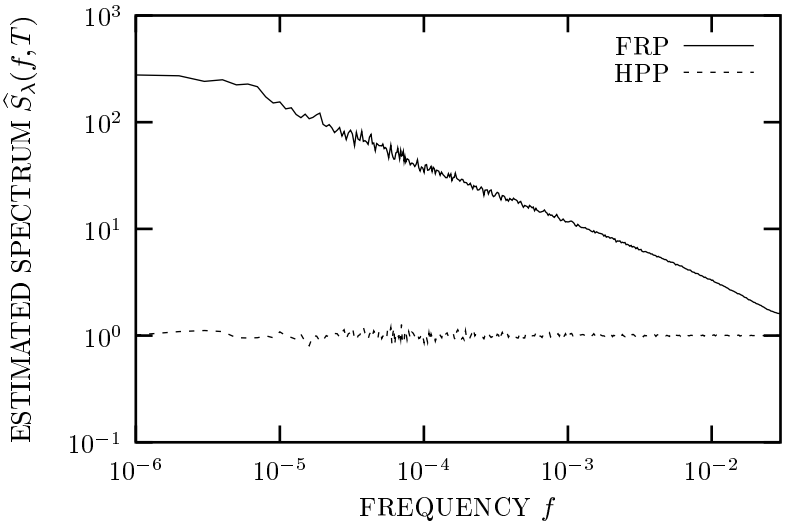

Fig. B.12 Estimated spectrum (periodogram) $\widehat{S}_\lambda(f,T)$ vs. frequency f for a simulated fractal renewal process (FRP, solid curve) and a homogeneous Poisson process (HPP, dashed curve) with the same mean rate, $\mathrm{E}[\mu] = \mathrm{E}[\tau] = 1$. The counting time $T = L/2^{16} \doteq 15.2588$. Parameters used in simulating the fractal renewal process are as follows: $\gamma = \frac{3}{2}$ ($\alpha = \frac{1}{2}$), $B/A = 10^6$, $A = 1.001001/3 = 0.333667$, $B = 0.333667 \times 10^6$, and $L = 10^6$. The spectrum reliably reports the presence of power-law behavior in the fractal process and its absence in the nonfractal process. Calculated point-process spectra for the fractal renewal process appear in Fig. 7.2.

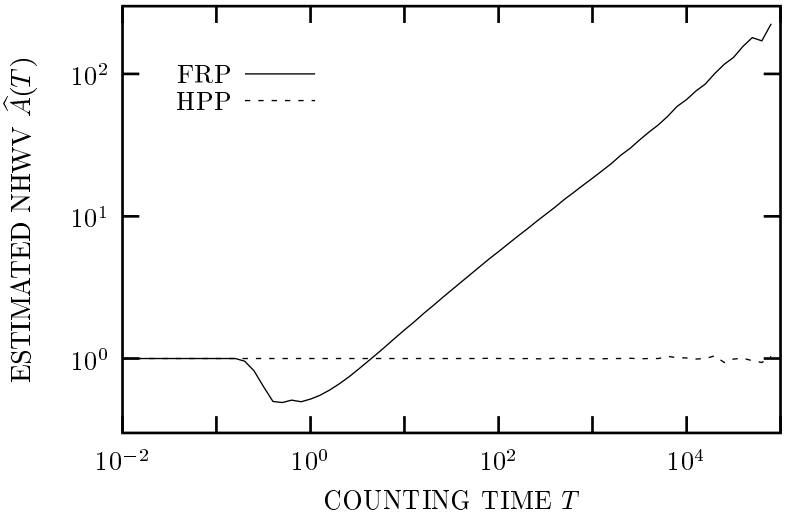

Fig. B.13 Estimated normalized Haar-wavelet variance, $\widehat{A}(T)$ vs. counting time T, for a fractal renewal point process (FRP, solid curve) and a homogeneous Poisson process (HPP, dashed curve) with the same mean rate of unity, $\mathrm{E}[\mu] = \mathrm{E}[\tau] = 1$. The caption of Fig. B.12 provides parameters for the fractal renewal process. Along with the results shown in Fig. B.12, this measure reliably reports power-law behavior in the fractal process and its absence in the nonfractal process. The dip in the curve for the fractal renewal process derives from the abrupt cutoff in the interevent-interval density for small intervals. A simulated version of $A(T)$ for $\gamma = \frac{1}{2}$, which also yields $\alpha = \frac{1}{2}$, appears in Fig. 7.5.

values in an attempt to improve fractal-exponent estimation, as discussed in Prob. 12.7. In the case at hand, the asymptote is unity; the decrease of $\widehat{A}(T)$ below unity therefore renders the adjusted normalized Haar-wavelet variance negative, an impossibility.

Figure B.14 shows the corresponding results for the estimated normalized rescaled range statistic, $\widehat{U}_2(k) = \widehat{U}^2(k)/k$. This measure should lie near unity for a nonfractal process, which indeed it does for the homogeneous Poisson process. However, it exhibits similar behavior for the fractal renewal process. Indeed, the two curves differ by less than a factor of 1.3 over the entire range examined, which spans five decades. This result confirms that this interval-based measure fails to reveal fractal behavior in the fractal renewal process.

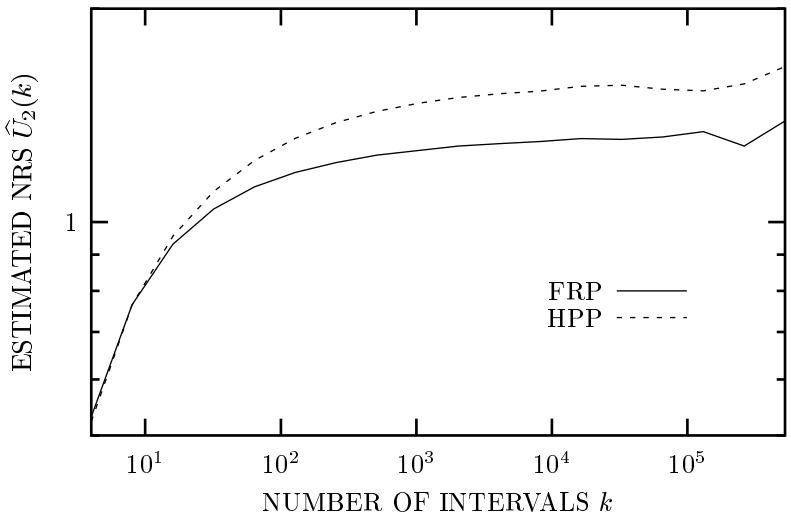

Fig. B.14 Normalized rescaled range estimate $\widehat{U}_2(k) = \widehat{U}^2(k)/k$ vs. number of intervals k, for a fractal renewal point process (FRP, solid curve) and a homogeneous Poisson process (HPP, dashed curve) with the same mean rate of unity, $\mathrm{E}[\mu] = \mathrm{E}[\tau] = 1$. The caption of Fig. B.12 provides parameters for the fractal renewal process. In contrast to the results demonstrated in Figs. B.12 and B.13, this measure fails to detect scaling behavior in the fractal process.

B.13 COMPUTER NETWORK TRAFFIC

Prob. 13.1 For both Eqs. (13.1) and (13.2) we simply set $Q_m \to \infty$. This leads to

$$\frac{dp\,(n,t)}{dt} = \begin{cases} -\mu_a\,p\,(n,t) & +\mu_s\,p\,(n+1,t) \qquad n=0 \\ -(\mu_a+\mu_s)\,p\,(n,t)+\mu_a\,p\,(n-1,t)+\mu_s\,p\,(n+1,t) & n>0 \end{cases} \tag{B.256}$$

and

$$p_\infty(n,t) \to (1-\rho_\mu)\,\rho_\mu^n, \tag{B.257}$$

as in Eq. (13.4).

Prob. 13.2 We wish to accommodate M servers, all handling requests from the same buffer. For large values of the queue length n, where all M servers are effective in decreasing it, we replace the service rate μ_s with $M\mu_s$. For smaller values of the buffer occupancy n, where not all servers can work at the same time, the service rate increases by a factor of only n, rather than M. The effective service rate therefore becomes $\min(n,M)\mu_s$, where the function $\min(\cdot\,,\cdot)$ returns the smaller of its two arguments. We must thus institute the following modifications in Eq. (13.1):

$$\begin{aligned} +\mu_s\,p\,(n+1,t) \quad &\to \quad +\min(n+1,M)\,\mu_s\,p\,(n+1,t) \\ -\mu_s\,p\,(n,t) \quad &\to \quad -\min(n,M)\,\mu_s\,p\,(n,t). \end{aligned} \tag{B.258}$$

Prob. 13.3 We obtain the queue-length distribution $p_\infty(n)$ directly from Eq. (13.4). From this we immediately write the four possibilities:

$$\begin{aligned} p_a \;&\equiv\; p_\infty(Q_m) \;&=\; (1-\rho_\mu)\,\rho_\mu^{Qm} \\ p_b \;&\equiv\; p_\infty(Q_m+1) \;&=\; (1-\rho_\mu)\,\rho_\mu^{Qm+1} \\ p_c \;&\equiv\; \sum_{n=Qm}^{\infty} p_\infty(n) \;&=\; \sum_{n=Qm}^{\infty} (1-\rho_\mu)\,\rho_\mu^n \;=\; \rho_\mu^{Qm} \\ p_d \;&\equiv\; \sum_{n=Qm+1}^{\infty} p_\infty(n) \;&=\; \rho_\mu^{Qm+1}. \end{aligned} \tag{B.259}$$

To determine which of these lies closest to the true result $p_Q(Q_m)$, we divide each by $p_Q(Q_m)$, as provided in Eq. (13.8). We then compare results, considering the limit $Q_m \to \infty$:

$$\begin{aligned} p_a/p_Q(Q_m) \;&=\; \left(1-\rho_\mu^{Qm+1}\right) \;\to\; 1 \\ p_b/p_Q(Q_m) \;&=\; \rho_\mu\left(1-\rho_\mu^{Qm+1}\right) \;\to\; \rho_\mu \\ p_c/p_Q(Q_m) \;&=\; (1-\rho_\mu)^{-1}\left(1-\rho_\mu^{Qm+1}\right) \;\to\; (1-\rho_\mu)^{-1} \\ p_d/p_Q(Q_m) \;&=\; \rho_\mu(1-\rho_\mu)^{-1}\left(1-\rho_\mu^{Qm+1}\right) \;\to\; \rho_\mu(1-\rho_\mu)^{-1}. \end{aligned} \tag{B.260}$$

We conclude that $p_a \equiv p_\infty(Q_m)$ provides the closest approximation to $p_Q(Q_m)$.

Prob. 13.4 A mean interevent interval of 10 msec and a mean service time of 9 msec together yield a service ratio $\rho_\mu = 0.9$. Since both the arrival and service processes follow a homogeneous-Poisson form, and a single server handles the requests, we can make use of the results obtained for the M/M/1/Q_m queue. Inverting Eq. (13.9) yields

$$Q_m = -\log\left(\rho_\mu + \frac{1-\rho_\mu}{P_B}\right) \Big/ \log(\rho_\mu). \tag{B.261}$$

Substituting the values $P_B = 10^{-3}$, 10^{-6}, and 10^{-9} into Eq. (B.261), and rounding up to the nearest integer, yields buffer sizes of 44, 110, and 175, respectively.

Prob. 13.5 We simulate this M/M/1 queue, effectively using two homogeneous Poisson processes. Since both the arrival and service processes lack memory, we can note the queue length after each event (arrival or departure from the queue), and base our results on that statistic. Alternatively, we can sample the queue at all times equal to integer multiples of a sampling time. Decreasing this sampling time provides better resolution. Indeed, we can effectively achieve an infinitesimal sampling time by recording the durations between events, which yields the proportion of the total time spent at each queue length. We use this approach in this simulation and in the ones following.

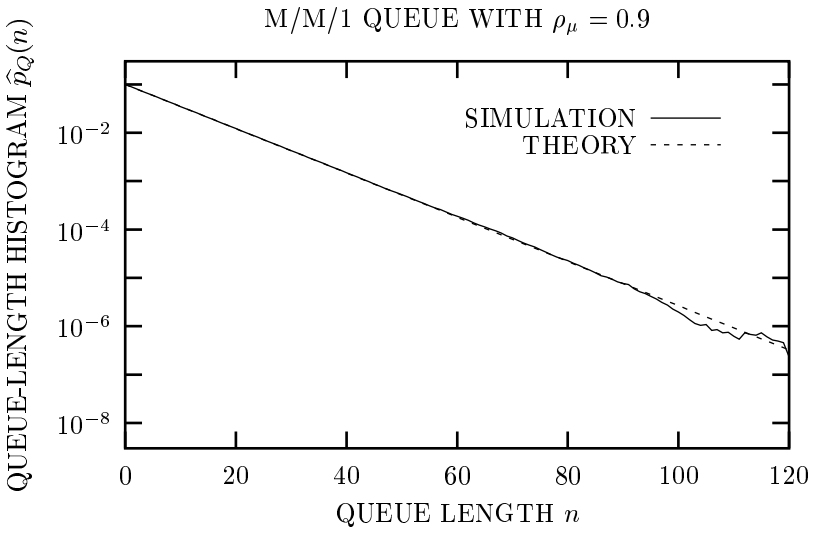

Fig. B.15 Simulated queue-length histogram for the M/M/1 queue with $\rho_\mu = 0.9$ (solid curve), and the geometric-distribution theoretical fit provided by Eq. (13.4) (dashed curve).

Figure B.15 presents the simulated queue-length histogram (solid curve), along with the theoretical result (dashed curve)

$$p_\infty(n) = (1 - \rho_\mu)\,\rho_\mu^n, \tag{B.262}$$

which is the geometric distribution reported in Eq. (13.4). The simulation agrees well with the theory.

In Prob. 13.4 we used analytical formulas for the M/M/1/Q_m queue to determine that buffer sizes of 44 and 110 correspond to overflow probabilities of 10^{-3} and 10^{-6}, respectively. The queue-length distribution for the M/M/1/∞ queue plotted in Fig. B.15 reveals that $p_\infty(44) \approx 10^{-3}$ and $p_\infty(110) \approx 10^{-6}$, thereby confirming the validity of Eq. (13.12) for sufficiently large values of Q_m: $P_B \approx p_\infty(Q_m)$.

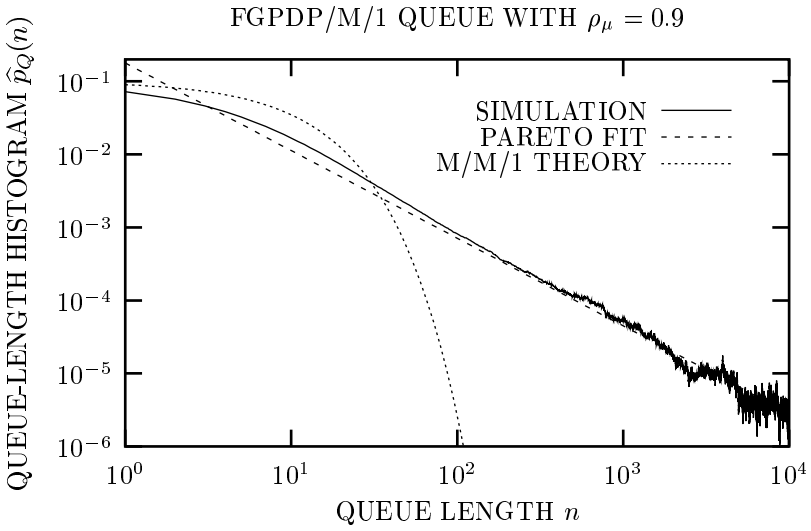

Fig. B.16 Simulated queue-length histogram $p_Q(n)$ for the FGPDP/M/1 queue (solid curve). Arrivals at the queue are described by a fractal-Gaussian-process-driven Poisson process (FGPDP) simulated using the following parameters: $\mathrm{E}[\mu] = 100$, duration $L = 10^6$, fractal exponent $\alpha = 0.8$, onset frequency $f_S = 0.2$, and fractal-Gaussian-process array size $M = 2^{24}$. With an expected service time of 0.009, this yields a service ratio $\rho_\mu = \mu_a/\mu_s = 100 \cdot 0.009 = 0.9$. We present an empirical power-law fit provided in Eq. (B.263) (dashed curve), and the M/M/1 theoretical geometric distribution from Eq. (13.4) (dotted curve). The simulated queue-length histogram closely follows the power-law decreasing form with the same fractal exponent, rather than the exponentially decreasing form of the M/M/1 distribution.

Prob. 13.6.1 Since we increase the length of the simulation by a factor of 100 over that used in Chapter 12, we increase the fractal Gaussian process array size M by a factor of $2^7 = 128$, the closest multiple of 2 to 100. Again, to ensure stationarity we

prepend an additional 1% of the total simulation, the results of which we then discard before compiling the queue-length histogram.

Figure B.16 displays the estimated queue-length histogram obtained by using this fractal-Gaussian-process-driven Poisson-process simulation for the arrival process, coupled with exponential service times and a single server: the FGPDP/M/1 queue (solid curve). We also present a power-law fit (dashed curve)

$$p_Q(n) = c\, n^{\alpha-2}, \tag{B.263}$$

with c chosen to yield a counting distribution that sums to unity (dashed curve), and α chosen to coincide with the design value $\alpha = 0.8$. The form of the exponent derives from asymptotic bounds on the queue (Likhanov, 2000). The distribution presented in Eq. (B.263) is known as the zeta distribution (see Sec. 2.7.1).

We also present the theoretical M/M/1 result set forth in Eq. (13.4) (dotted curve). The simulated queue-length histogram behaves as a decaying power-law function rather than as a decaying exponential function. The arrival process evidently imparts its fractal character to the queueing process, yielding the power-law behavior of the FGPDP/M/1 queue-length distribution (straight line on a doubly logarithmic plot).

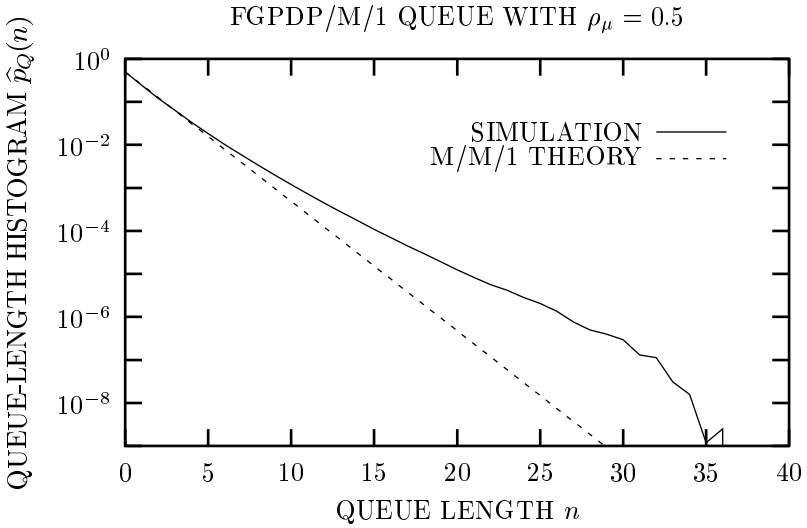

Fig. B.17 Simulated queue-length histogram $p_Q(n)$ for the FGPDP/M/1 queue (solid curve). Arrivals at the queue are described by a fractal-Gaussian-process-driven Poisson process (FGPDP) simulated using the following parameters: $\mathrm{E}[\mu] = 100$, duration $L = 10^6$, fractal exponent $\alpha = 0.8$, onset frequency $f_S = 0.2$, and fractal-Gaussian-process array size $M = 2^{24}$. Decreasing the expected service time to 0.005 reduces the service ratio to $\rho_\mu = \mu_a/\mu_s = 100 \cdot 0.005 = 0.5$. The M/M/1 theoretical geometric distribution from Eq. (13.4) appears as well (dashed curve). The simulated queue-length histogram follows the exponentially decreasing form of the M/M/1 distribution reasonably well.

Prob. 13.6.2 Reducing the mean service time from 0.009 to 0.005 serves to reduce the service ratio ρ_μ and to greatly diminish the queue length. With the average service rate nearly doubled, even large clusters of arrivals pass through the server without significantly burdening the queue. Figure B.17 presents the simulated FGPDP/M/1 queue-length histogram (solid curve), along with the theoretical M/M/1 queue-length distribution set forth in Eq. (13.4) (dashed curve). Though not perfect, the M/M/1 result provides a far superior fit than does a power-law form, which would exhibit significant curvature on this plot (not shown).

Prob. 13.7 Since the fractal-based point process used in Prob. 13.6 has a Poisson kernel and the rate process has a standard deviation smaller than the mean ($C_\mu < 1$), the probability density associated with the resulting interevent intervals does not depart greatly from an exponential form [see Eq. (4.33)]. Hence, shuffling the intervals results in a simulated renewal point process with an estimated interevent-interval density close to an exponential form. This corresponds to a homogeneous Poisson point process. We therefore expect that the SHUFFLED-FGPDP/M/1 traffic process will lead to results similar to those obtained for the M/M/1 queue discussed in Prob. 13.5.

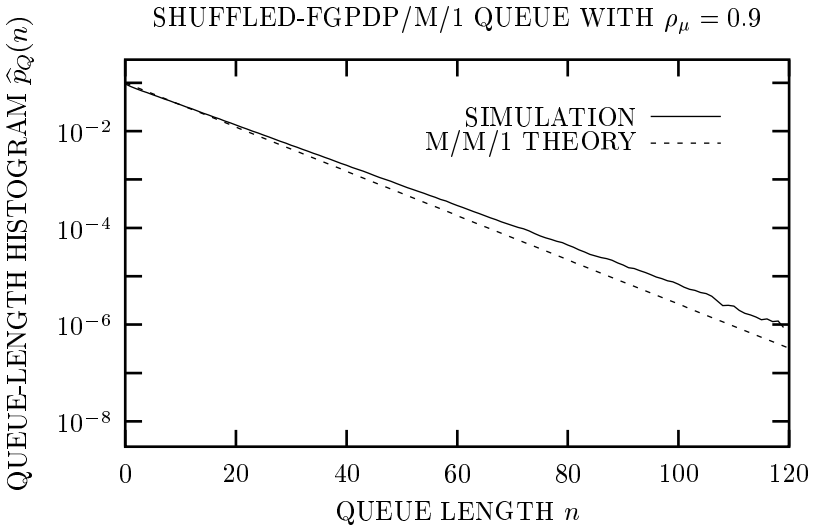

Fig. B.18 Simulated queue-length histogram $p_Q(n)$ for the FGPDP/M/1 queue, after shuffling (solid curve). Arrivals at the queue are described by a shuffled version of a fractal-Gaussian-process-driven Poisson process (FGPDP) simulated using the following parameters: $\mathrm{E}[\mu] = 100$, duration $L = 10^6$, fractal exponent $\alpha = 0.8$, onset frequency $f_S = 0.2$, and fractal-Gaussian-process array size $M = 2^{24}$. The service ratio was $\rho_\mu = 0.9$. The M/M/1 theoretical geometric distribution (using the theoretical arrival rate) of Eq. (13.4) also appears (dashed curve). The simulated queue-length histogram closely follows the exponentially decreasing form of the M/M/1 distribution, rather than the power-law decreasing form followed by the unshuffled results (see Fig. B.16).

Figure B.18 displays the queue-length histogram resulting from the simulation (solid curve), along with a plot of the theoretical geometric M/M/1 result (dashed curve), as provided in Eq. (13.4). As before, we discard an added initial 1% before analyzing the queue-length statistics. The M/M/1 theoretical result fits the simulation reasonably well. The modulating effect of the fractal Gaussian process influences the ultimate mean value of the point process, so that we gain improved agreement by using the measured arrival rate (100.587) in Eq. (13.4), rather than the expected value $\mu_a = 100$ (not shown). Still better agreement would obtain from incorporating the deviation of the interevent-interval density from an exponential form.

Prob. 13.8 Figure B.19 displays the estimated queue-length histogram obtained by using a rectangular fractal-shot-noise-driven Poisson simulation for the arrival process, coupled with exponential service times and a single server (solid curve): this appears as the RFSNDP/M/1 queue. We also show the power-law form of Eq. (B.263) (dashed curve) using the design value $\alpha = 0.8$, and the theoretical M/M/1 queue re-

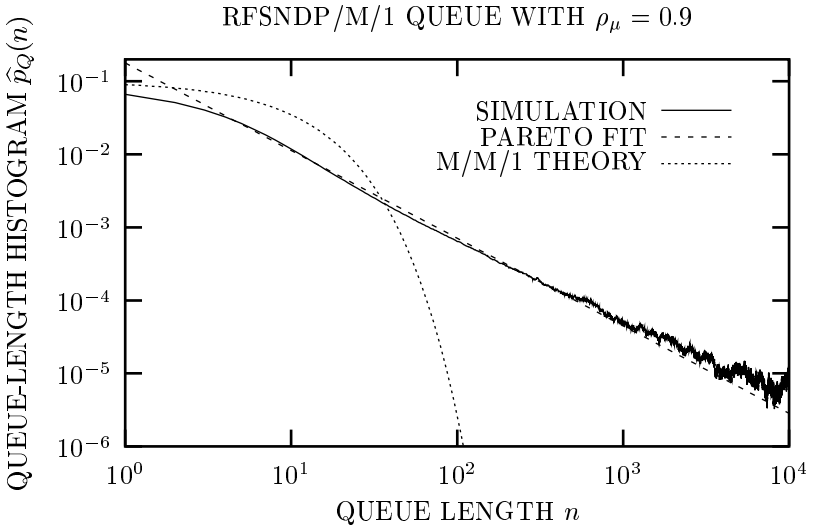

Fig. B.19 Simulated queue-length histogram $p_Q(n)$ for the RFSNDP/M/1 queue (solid curve). A rectangular fractal-shot-noise-driven Poisson process (RFSNDP) describes arrivals at the queue; the impulse-response-function duration B obeys a decaying power-law distribution $\sim B^{-1.2}$. The service ratio $\rho_\mu = \mu_a/\mu_s = 100 \cdot 0.009 = 0.9$. We also shown the simple power-law form provided in Eq. (B.263) (dashed curve), and the M/M/1 theoretical geometric distribution of Eq. (13.4) (dotted curve). The simulated queue-length histogram closely follows that of the FGPDP/M/1 queue displayed in Fig. B.16. A simple power-law decreasing fit with exponent $\alpha - 2 = -1.2$ thus describes both the FSNDP/M/1 and FGPDP/M/1 queues well for a broad range of queue lengths, while the exponentially decreasing M/M/1 queue-length distribution does not.

sult from Eq. (13.4) (dotted curve). The simulation follows a simple power law with exponent $\alpha - 2 = -1.2$ over a large range of queue lengths.

As expected, the outcome resembles that obtained for the FGPDP/M/1 queue (see Fig. B.16), where the arrival process at the queue is a fractal-Gaussian-process-driven Poisson process.

Prob. 13.9 Figure B.20 shows the estimated queue-length histogram obtained by using a modulated fractal-Gaussian-process-driven Poisson simulation for the arrival process, coupled with exponential service times and a single server (solid curve); we denote this the MODULATED-FGPDP/M/1 queue. The modulation is sinusoidal with unity modulation depth. We also show the result for the original (unmodulated) fractal-Gaussian-process-driven Poisson simulation (dashed curve).

In comparison with the original, the modulated version lies below it at small queue lengths, and above it at large queue lengths. The depression and bump in the modulated curve resemble the depression and bump in the sinusoidally modulated

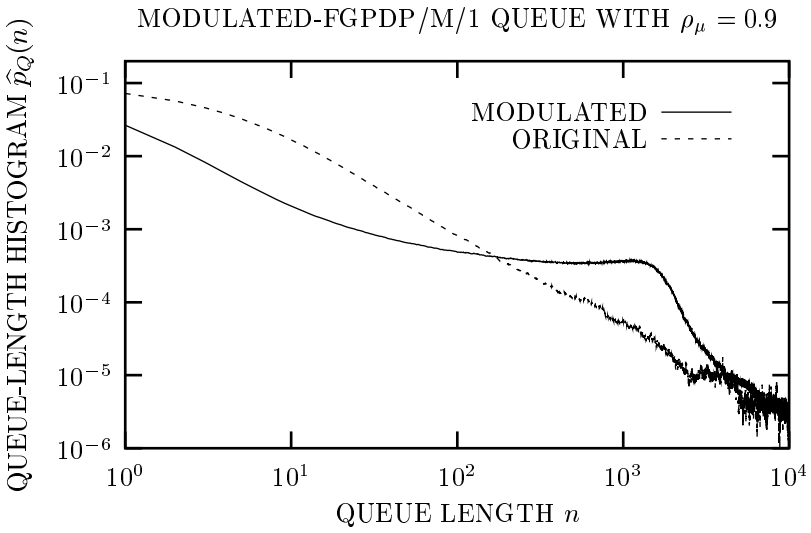

Fig. B.20 Simulated queue-length histogram $p_Q(n)$ for the MODULATED-FGPDP/M/1 queue (solid curve). We begin with an unmodulated simulation of the fractal-Gaussian-process-driven Poisson process (FGPDP). This process appears in connection with Prob. 13.6 and relies on the following parameters: $\mathrm{E}[\mu] = 100$, duration $L = 10^6$, fractal exponent $\alpha = 0.8$, onset frequency $f_S = 0.2$, and fractal-Gaussian-process array size $M = 2^{24}$. The service ratio for both Prob. 13.6 and the problem at hand is $\rho_\mu = \mu_a/\mu_s = 100 \cdot 0.009 = 0.9$. To generate the modulated curve, we warped the time axis in a suitable manner (see text) to achieve sinusoidal modulation with $\mu_0/\omega_0 \gg 1$, $a = 1$, and $2\pi/\omega_0 = 1$ min [see Eq. (13.16)] and used this as the arrival process. We present a queue-length histogram for the FGPDP/M/1 queue as the dashed curve. Roughly speaking, the solid curve follows the power-law decaying trend of the dashed curve within an order of magnitude.

Poisson-process counting distribution; this result appears in both theory (Diament & Teich, 1970b, Fig. 7) and experiment (Teich & Vannucci, 1978, Fig. 1). These features carry through from the driving rate process, which heavily favors the peaks and troughs of the sinusoid at the expense of the mean. As in the absence of modulation, the arrival process imparts its fractal nature to the queue length.

The queue-length histogram roughly follows the power-law decaying trend of the unmodulated simulation and, in fact, the two curves lie within an order of magnitude of each other at all values of the queue length. The power-law form therefore provides a far closer approximation to modulated simulation than does the M/M/1 queue, although the modulation destroys the precise power-law behavior seen in the original.

Prob. 13.10.1 To summarize, we have

$$\begin{array}{rcl} L & \geq & 10\,T_{A4} \\ T_{A4} & \geq & 10^3\,T_{A3} \\ T_{A3} & \geq & T_{A2} \\ T_{A2} & \geq & 10^3\,T_{A1} \\ T_{A1} & = & 10\,\mathrm{E}[\tau], \end{array} \tag{B.264}$$

which, taken together, provide $L \geq 10^8\,\mathrm{E}[\tau]$. Since the expected number of events $\mathrm{E}[N(L)] = L/\mathrm{E}[\tau]$, we have $\mathrm{E}[N(L)]/\mathrm{E}[\tau] \geq 10^8$, so that the average simulation must contain at least 10^8 events.

Prob. 13.10.2 First, suppose we assume equalities in Eq. (B.264). Then $T_{A3} = T_{A2}$. When T equals this transition time, the contribution of the α_1 term becomes $(T_{A2}/T_{A1})^{\alpha_1}$. For the α_2 term to dominate for $T > T_{A3} = T_{A2}$, it must achieve the same value at that same time; thus it becomes $(T_{A2}/T_{A1})^{\alpha_1} \times (T/T_{A2})^{\alpha_2}$. Recall again that we have set $T_{A3} = T_{A2}$. The resulting normalized Haar-wavelet variance then becomes

$$A(T) = 1 + (T/T_{A1})^{\alpha_1} + (T_{A2}/T_{A1})^{\alpha_1}(T/T_{A2})^{\alpha_2}. \tag{B.265}$$

Least-squares fitting programs applied directly to doubly logarithmic curves yield results that proportionally follow large values of the ordinate far more closely than small ones. However, instead of employing Eq. (B.265) we can instead perform a least-squares fit to the modified equation

$$f(x) = \log\Big\{1 + \big[\exp(x)/T_{A1}\big]^{\alpha_1} + (T_{A2}/T_{A1})^{\alpha_1}\big[\exp(x)/T_{A2}\big]^{\alpha_2}\Big\}. \tag{B.266}$$

To maintain equal weighting over all decades, we choose geometric spacing for T, which is equivalent to linear spacing for x.

Using this method, we obtain monofractal parameters $\alpha \doteq 0.615716$ and $T_A \doteq 24.7731$. Figure B.21 displays the bifractal curve and the monofractal fit, which follows it fairly well.

Were real teletraffic to follow the bifractal curve in Fig. B.21, a cursory analysis might lead us to conclude that the data follows a monofractal form. Indeed, Occam's

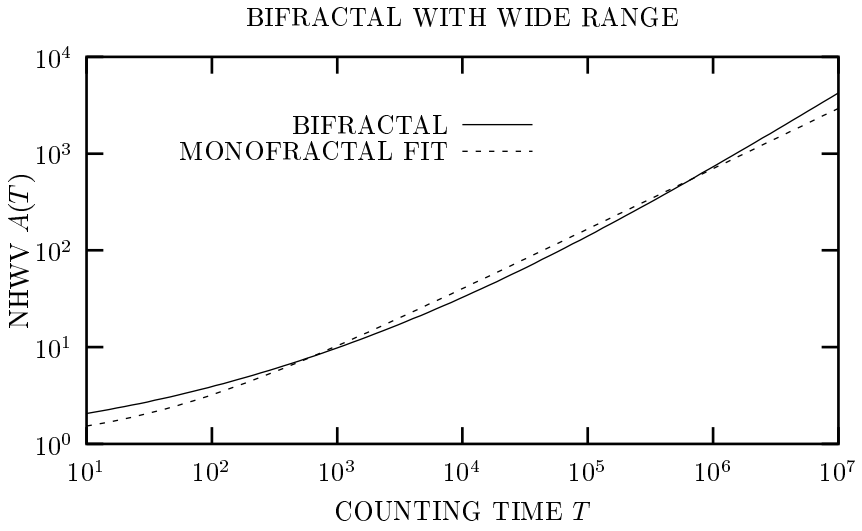

Fig. B.21 Bifractal form of the normalized Haar-wavelet variance provided in Eq. (B.265) (solid curve), and the monofractal logarithmic least-squares fit obtained via Eq. (B.266) (dashed curve), for the wide scaling range $T_{A2}/T_{A1} = T_{A4}/T_{A3} = 10^3$.

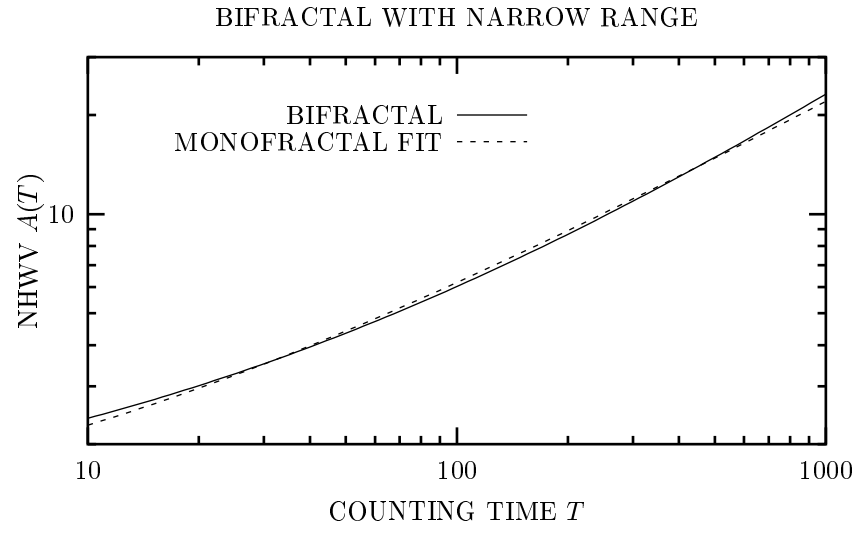

Fig. B.22 Bifractal form of the normalized Haar-wavelet variance provided in Eq. (B.265) (solid curve), and the monofractal logarithmic least-squares fit obtained via Eq. (B.266) (dashed curve), for the narrow scaling range $T_{A2}/T_{A1} = T_{A4}/T_{A3} = 10$.

razor would encourage us to draw this conclusion. However, Fig. B.21 illustrates that a significant difference exists between the two results, in the sense of Eq. (12.25), which favors the bifractal interpretation. Still, real data almost never follow precise forms, be they bifractal, monofractal, or otherwise; this makes a monofractal interpretation at least plausible, despite the relatively wide scaling ranges T_{A4}/T_{A3} and T_{A2}/T_{A1}.

For the narrow scaling range $T_{A2}/T_{A1} = T_{A4}/T_{A3} = 10$, the interpretation becomes quite murky. Here we obtain $\alpha \doteq 0.606821$ and $T_A \doteq 6.61332$; interestingly, the monofractal cutoff time T_A lies below both T_{A1} and T_{A3}. Figure B.22 displays the results. Deducing the presence of two scaling regions from data with these characteristics would prove nearly impossible.